University of Southern Queensland

Faculty of Engineering & Surveying

Optimisation of Low-Cost Astronomical Site Testing Techniques

A dissertation submitted by

Ramin Rafiei

in fulfilment of the requirements of

ENG4111 and ENG4112 Research Project

towards the degree of

Bachelor of Computer Systems Engineering / Bachelor of Science (Physics)

Submitted: November, 2006

Abstract

"Seeing" is the term used in astronomy to quantify the steadiness of the atmosphere. Seeing affects the performance of large optical telescopes by determining the obtainable spatial resolution of the image. It is therefore of great significance in selecting optimum sites for astronomical observatories. A low cost technique for the measurement of seeing has been developed and optimised to help USQ astronomers select optimum sites for the installation of telescopes of aperture 0.5 to 1.0m. This is needed for a NASA funded collaboration with the University of Louisville, Northern Kentucky University, and the Cosmos Centre in Western Queensland.

The physics of optical astronomy, and the past and present methods for the measurement of seeing are reviewed. This identified the measurement of the full width half maximum (FWHM) of the stellar profile, obtained through stellar imaging or stellar trail imaging, as the appropriate seeing measurement technique in terms of available equipment and the low cost criterion. An ST-4 camera in combination with a 10-inch Meade LX200 f/10 telescope was chosen as the test bed for this project. The application of Nyquist's theorem to stellar profile sampling suggested that the ST-4 can resolve seeing down to only 3.1 arcseconds, far from the requirement of 1 arcsecond. However, a study of the interrelation of resolution and signal to noise ratio indicated that the Nyquist criterion does not set the absolute limitation on the accurate measurement of seeing.

An extensive study was therefore carried out to understand what controls the accuracy of the measurement of seeing. Error estimation theory based on the Levenberg-Marquardt Non-Linear Least Squares (LMNLLSQ) fitting technique identified: (i) that the standard error in the measurement of seeing is inversely proportional to the signal to noise ratio; (ii) the ex-

istence of an optimum fitting window; (iii) that decreasing resolution increases the standard error at the optimum fitting window. Based on these results, a fitting environment was created using LMNLLSQ, which allowed for optimised determination of seeing. To test this theory, fitting to simulated stellar profiles was performed for many parameter sets. This showed that using the ST-4, seeing can be measured down to 1.4 arcseconds. By extending the optimisation procedure to stellar trails and fitting to simulated trails, seeing could be measured down to 1 arcsecond and with an accuracy of 0.11 arcseconds.

The project objectives have therefore been achieved as the seeing can now be measured with an accuracy of better that 0.5 arcseconds and down to 1 arcsecond. The developed techniques are widely applicable to the design of seeing measurement systems and the analysis of their data. After experimental validation, this low cost technique will be ready for implementation in Western Queensland and world wide.

University of Southern Queensland

Faculty of Engineering and Surveying

ENG4111/2 *Research Project*

Limitations of Use

The Council of the University of Southern Queensland, its Faculty of Engineering and Surveying, and the staff of the University of Southern Queensland, do not accept any responsibility for the truth, accuracy or completeness of material contained within or associated with this dissertation.

Persons using all or any part of this material do so at their own risk, and not at the risk of the Council of the University of Southern Queensland, its Faculty of Engineering and Surveying or the staff of the University of Southern Queensland.

This dissertation reports an educational exercise and has no purpose or validity beyond this exercise. The sole purpose of the course pair entitled "Research Project" is to contribute to the overall education within the student's chosen degree program. This document, the associated hardware, software, drawings, and other material set out in the associated appendices should not be used for any other purpose: if they are so used, it is entirely at the risk of the user.

Prof R Smith

Dean

Faculty of Engineering and Surveying

Certification of Dissertation

I certify that the ideas, designs and experimental work, results, analyses and conclusions set out in this dissertation are entirely my own effort, except where otherwise indicated and acknowledged.

I further certify that the work is original and has not been previously submitted for assessment in any other course or institution, except where specifically stated.

RAMIN RAFIEI

0011226728

_____

Signature

_____

Date

Acknowledgments

I would like to express my sincere gratitude to Associate Professor Nigel Hancock, Dr Rhodes Hart and Dr Brad Carter for their advice, guidance, constructive criticism and support throughout the year. Last, but not least, my dear parents whose unfailing faith in me has been a constant comfort and source of inspiration.

<div align="right">

RAMIN RAFIEI

</div>

University of Southern Queensland
November 2006

Contents

List of Figures

List of Tables

Chapter 1

Introduction

This project aims to optimise astronomical seeing measurements using low cost instrumentation. "Seeing" is the term used in astronomy to quantify the steadiness of the atmosphere. The performance of an optical telescope largely depends on the obtainable image quality. The quality of an astronomical image is dependent on the seeing at that particular site, as seeing determines the obtainable spatial resolution of the image. The development of an optical observatory needs to be guided by an understanding of typical seeing conditions, as investment in large and expensive equipment is unquestionably best done at sites where good seeing conditions are typical. Therefore selecting sites with "good" seeing has become of paramount importance.

USQ astronomers are currently engaged in several robotic telescope projects. These projects include a NASA funded collaboration with the University of Louisville, Northern Kentucky University, and the Cosmos Centre in Western Queensland and aim to develop remotely and robotically operated astronomical facilities for educational outreach, tourism, teaching, and research.

To best utilise these expensive telescopes, sites with lowest seeing must be identified which requires simultaneous measurements of seeing at multiple sites over a period of typically one year. To facilitate this, low cost techniques for the measurement of seeing have been developed and optimised, hence making simultaneous measurements an affordable process.

This project aims to optimise the low cost measurement of astronomical seeing within the required range of 1-10 arcseconds and to an accuracy of 0.5 arcseconds. While the optimised low cost techniques are applicable to any imaging system, the ST-4 Star Tracker Imaging Camera manufactured by Santa Barbara Instrument Group, Inc, owned by the University of Southern Queensland, was used as a test bed.

Initial project work explored the science of seeing and site testing. It further investigated the past and present techniques and technologies for seeing measurement which revealed that the literature was sparse. This review showed that the current seeing measurement systems are not wholly suited for low cost measurement of seeing in the Southern Hemisphere. Hence the project focuses on the optimisation of low cost seeing measurement based on the full width half maximum of stellar profiles and stellar trails.

Theoretical analysis and simulations performed in this project have refined low cost astronomical seeing measurements. Simulations have shown that conventional thinking on the limits of seeing measurement (application of Nyquist theorem to stellar profile sampling), can be exceeded. While conventional analysis on the ST-4 CCD camera, identified it as unsuitable for the measurement of seeing down to 1 arcsecond, optimised low cost techniques prove otherwise.

1.1   Project Objectives

1. Research information on optical astronomy, in particular its limitations. Identify the components of site-evaluation and the characteristics of a 'good' astronomical site.

2. Analyse past and present techniques and technologies used for the measurement of seeing and identify the best method to measure the seeing for a low-cost implementation.

3. Evaluate the suitability of the available equipment for a low-cost seeing measurement system which will measure the seeing within 1-10 arcseconds and to an accuracy of 0.5 arcseconds.

4. Investigate possible data-analysis techniques to overcome conventional limitations of low-cost seeing measurement techniques:

    (a) Examine the sources of error in seeing measurement.

(b) Find the conditions for optimum seeing determination.

5. Explore related techniques that may yield further improvement in low cost seeing measurement.

1.2   Overview of the Dissertation

Chapter 2 provides an overview of astronomy in the optical region of the spectrum using ground based telescopes, with particular focus on the limitations imposed on optical astronomy by the Earth's atmosphere. It further explores in detail the components of astronomical site testing and develops a detailed description of the term 'seeing' and its measurement.

Chapter 3 evaluates the past and present techniques and technologies used for the measurement of astronomical seeing. This chapter serves two purposes: (i) it firstly identifies the most appropriate technique for the low cost measurement of seeing by showing that the current seeing measurement systems are not wholly suited for the low cost measurement of seeing in the Southern Hemisphere; (ii) it amalgamates all past and present seeing practices within the three categories of visual, photographic and digital – because of the absence of an accessible, universal review on the practice of seeing. The measurement of the full width half maximum (FWHM) of the stellar profile obtained through stellar imaging or stellar trail imaging was found to be the appropriate technique in terms of available equipment and the low cost criterion.

Chapter 4 investigates the three identified critical design factors, namely field of view and stellar density function, signal to noise ratio and resolution, in order to examine the suitability of both digital (CCD) and photographic implementations of low cost seeing measurement. While the results have demonstrated that both methods fail to measure the seeing to the defined specification, owing to poor Nyquist resolution, the identified interrelation of signal to noise ratio and resolution has provided a way forward.

Chapter 5 determines how much below the Nyquist sampling resolution we can sample the stellar profile, and the S/N that we require in order to make an acceptable fit to the signal (i.e. within 0.5 arcseconds as defined by the project specifications). In obtaining a solution both fitting error analysis and simulations were used. The dependency of

fitted errors of the FWHM on the signal-to-noise, resolution and fitting window width was identified using the Levenberg-Marquardt non-linear least squares fitting technique. Simulations were used to show that the application of the Nyquist theorem to stellar profile sampling can be exceeded.

Chapter 6 proves that further significant gains in the lowest resolvable seeing can be obtained by fitting to star trails, using stellar trail modelling and simulations.

Chapter 2

Review of the Physics of Ground Based Optical Astronomy and its Limitations

2.1   Chapter Overview and Rationale

Astronomical information from beyond the solar system travels to us in the form of electromagnetic waves. Of this vast range of wavelengths, our eyes are sensitive only to the visible wavelength range (400-700nm). Optical astronomy refers to astronomy in the visible range of light, where optical components such as lenses and mirrors are used to control the paths of light rays. The intergalactic and interstellar media, the Earth's atmosphere and the telescope and detection system used, filter, and therefore alter, much of the light that reaches the Earth's surface. When performing optical astronomy it is of paramount importance that the astronomer is aware of how the atmosphere and the instrumentation used influence the image quality, so that their effects can be minimised and corrections can be made.

This chapter is intended to provide an overview of the fundamentals of astronomy in the optical region of the spectrum using ground based telescopes, with particular focus on the imposed limitations by the Earth's atmosphere. These limitations have defined the components of site evaluation, a process which is critical for the identification of sites where large optical telescopes are best utilised.

2.2   Primary Tools for Optical Astronomers

2.2.1   Lenses and Mirrors

A lens is a device for either concentrating or diverging light, usually formed from a piece of glass. In optical astronomy we are concerned with a lens system that converges light rays to a focus, thus producing an image. Such a lens is called a convex lens. A convex lens will make an image of a distant object that is smaller than the object and upside down. The ray-diagram for such an arrangement is provided in Figure 2.1.
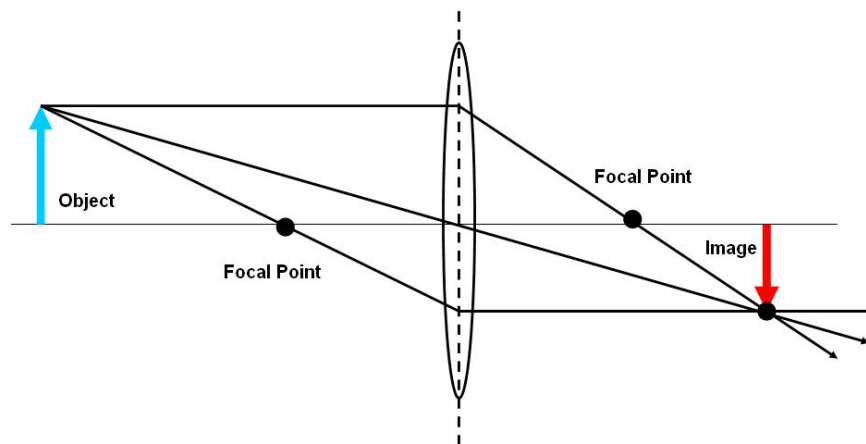
Figure 2.1: Interaction of a Light Ray with a Convex Lens.

A mirror can be simply defined as a surface with specular reflection that allows an image to be formed. Shown in Figure 2.2 is a perfect parabolic mirror where all light rays come to a focus. The ray-diagram for a parabolic mirror is provided in Figure 2.3.
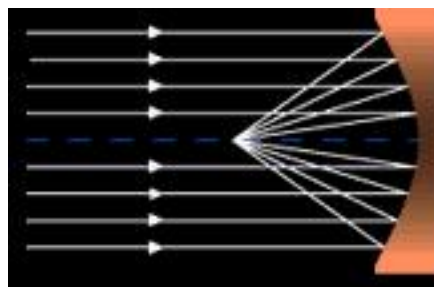
Figure 2.2: Interaction of Light Rays with a Parabolic Mirror (adapted from Hecht (2002)).

The three main characteristics of a lens/mirror system are its focal length, object distance and
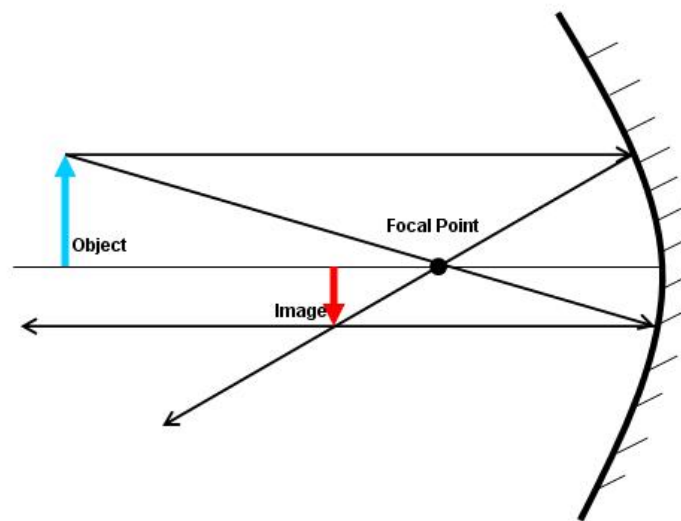
Figure 2.3: An Image Formation Diagram for Light Rays Incident on a Parabolic Mirror from a Distant Object.

image distance which are related by the Lens Equation defined by Equation 2.1:

$$\frac{1}{f} = \frac{1}{d_o} + \frac{1}{d_i} \tag{2.1}$$

where d_o is the object distance, d_i is the image distance and f is the focal length. For an object at infinity, such as a star, the distance from the convex lens to the image is the same for all objects and equal to the focal length. Such a system forms the simplest of all telescopes in which an image forms on the focal plane.

2.2.2 Telescopes

There are three basic types of telescopes - refracting, reflecting and catadioptric. Refractors use a lens as the primary light gathering element (primary lens) while reflectors use a mirror to gather light (primary mirror). Both transmissive and reflective elements are used for light gathering in a catadioptric telescope. The use of a lens as the primary light gathering element has many disadvantages. Since the light must pass through the lens it must be supported only along the edge of the glass. Large lenses can sag slightly in the middle, thus distorting the image; therefore refracting telescopes have a limit on their size ("size" refers to the diameter

of the primary lens). Refracting telescopes also suffer from chromatic aberration, where light from different wavelengths does not focus at one point, resulting in the formation of coloured halos around the bright image. The largest refracting telescopes include the Lick 36 inch and Yerkes 40 inch telescopes (Roussel 1997).

The Schmidt-Cassegrain telescope is a catadioptric telescope. As shown in Figure 2.4 the Schmidt-Cassegrain system consists of a spherical mirror, convex mirror and Schmidt corrector plate. The spherical primary mirror focuses the incoming light onto a secondary mirror which sends the light back through a hole in the primary mirror to the eyepiece, located at the rear of the telescope. A corrector plate is used at the front of the telescope to correct the spherical aberration due to the use of a spherical rather than parabolic primary mirror.
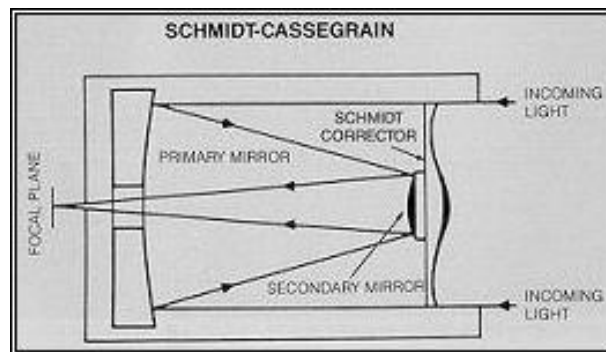
Figure 2.4: The Schmidt-Cassegrain Optical System (adapted from Hinds (2004)).

2.3 Fundamental Parameters of Optical Astronomy

2.3.1 F-ratio and Plate Scale

F-ratio

The f-ratio of a telescope is defined as the ratio of the focal length to the diameter of the primary lens/mirror given by Equation 2.2:

$$\text{f}-\text{ratio} = \frac{f}{D} \tag{2.2}$$

where f is the focal length and D is the diameter of the primary lens or mirror. The focal length sets the size of the image, and the diameter of primary lens/mirror controls the amount of light in the image. As a result the f-ratio gives the image brightness, where a smaller f-ratio corresponds to a brighter image (Zeilik 1981).

Plate Scale

For a star, effectively at an infinite distance, as shown in Figure 2.5, its image is given by the small angle approximation:

$$\mathrm{I} = f\tan\delta \simeq f\delta \tag{2.3}$$

where f is the focal length and δ is the angle between the star and the optical axis.
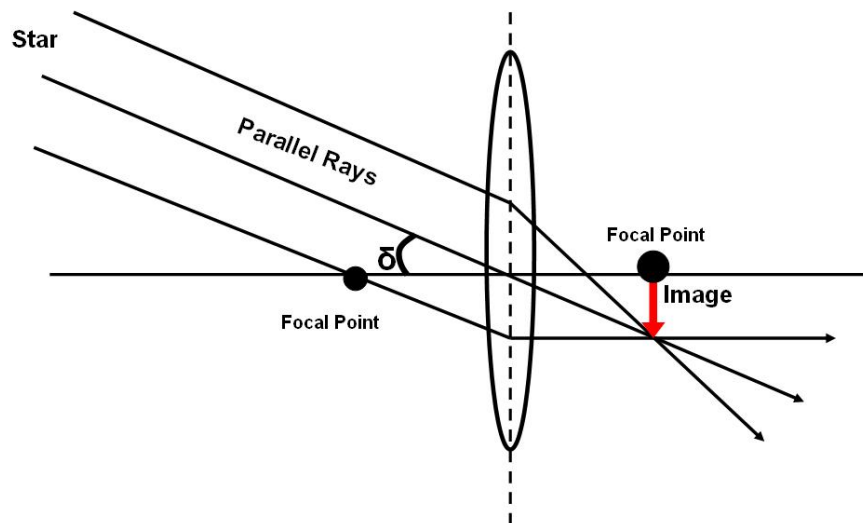
Figure 2.5: The Small Angle Approximation allows for the Angular Measurement of the Star.

The plate scale is a scale factor for converting a linear measure on the image plane to an angular measure in the sky. Based on Equation 2.3 the plate scale is defined as:

$$s = \frac{\pi}{180} \times f \tag{2.4}$$

where f is the focal length and s is the plate scale in units of f per degree (Zeilik 1981). Traditionally, the mapping between the angle on the sky and distance in the focal plane is expressed by Equation 2.5:

$$s[\mathrm{arcsec/mm}] = \frac{206265}{f[\mathrm{mm}]} \tag{2.5}$$

where 206265 is the number of arcseconds in one radian [1].

2.3.2 Light Gathering Power, Resolving Power and Magnification

Light Gathering Power

Light gathering power (LGP) is the most important function of a telescope. A star sources steady stream of photons that strike the ground with a certain number of photons per unit area per second. If we observe the star directly we only see photons that directly pass through the pupil of our eye. A telescope on the other hand allows for the collection of photons over an area much larger than our eye and concentrates them onto our eye, thus delivering more photons per second. A telescope's light gathering power is directly proportional to the square of its diameter and is obtained by Equation 2.6:

$$\mathrm{LGP} = \left(\frac{D_o}{D_e}\right)^2 \tag{2.6}$$

where D_o is the diameter of the objective lens/mirror and D_e is the diameter of the eyepiece lens (Kutner 2003).

---

[1] The degree ($^\circ$) is the most common unit used for angular measurements. There are 360° in a circle. The number 360 is completely arbitrary and its origins can be traced back to the Babylonians, who used a base 60 number system. A degree can be divided into 60 minutes of arc, or arcminute (′), each arcminute can then be further subdivided into 60 seconds of arc,or arcseconds (″). Another way of measuring angles is by using the radian. One radian is the angle defined by an arc length equal to the radius of the circle. There are 2π radians in one complete circle so that there are $180/\pi$ degrees or 206265 ($180/\pi \times 3600$) arcseconds in one radian.

Resolving Power

The second most important function of a telescope is to provide increased angular resolution. The resolution is the ability of the telescope to separate objects in the sky that are close together. This ability is called resolving power (RP) and is defined by Equation 2.7 as the inverse of the minimum angle there must be between two points in order for them to be easily separated (Zeilik 1981).

$$\text{RP} = \frac{1}{\theta_{\min}} \tag{2.7}$$

The minimum angle and resolving power are both a function of the diameter of the objective and the wavelength of light being observed. The minimum angle is given by Equation 2.8:

$$\theta_{\min} = \frac{206265\lambda}{D} \tag{2.8}$$

where λ,the wavelength of light being observed, and D ,the diameter of the objective, are both to be expressed in the same units of length. The value of 206265 provides us with a conversion from radians to arcseconds (Zeilik 1981).

A source with no angular extent is defined as a point source. Although real stars have a slight angular extent, they can be assumed as point sources when viewed through an optical telescope. Ignoring the effects of the Earth's atmosphere, one would expect that a star viewed through an optical telescope would produce a point image. The Hubble Space Telescope sitting outside the Earth's atmosphere does not focus a point source onto a point image due to a natural phenomenon called diffraction.

The resolution of a telescope is limited by the diffraction pattern of the aperture. For a point source from infinity some of the light will be spread away from the centre of the image when it passes through the aperture. The diffraction pattern of a circular aperture is called an Airy pattern which is a pattern of maxima and minima. As illustrated in Figure 2.6, from diffraction theory it can be shown that for an Airy pattern the central maximum contains 84% of the power.

The **Dawes' limit**, also called the **Rayleigh's limit**, provide us with the theoretically diffraction
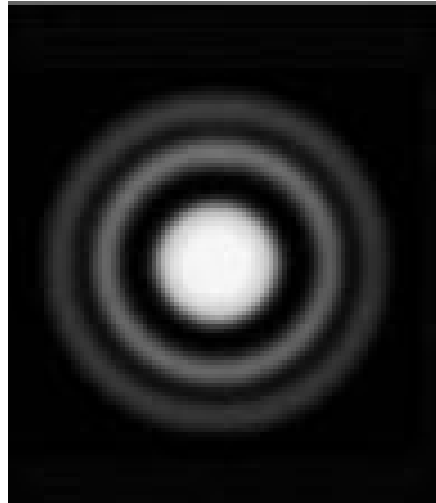
Figure 2.6: The Diffraction Pattern of a Circular Aperture is an Airy Pattern (reproduced from Newsam (2006)).

limited resolution of a telescope. When the centre of the Airy disc of one image is superimposed upon the first minimum of the other image we have reached the Dawes'/Rayleigh's limit for the resolution of a lens/mirror. If $\Delta\theta$ represents the angular width of the central maximum, it is related to the wavelength of the wave and the diameter of the aperture D, by Equation 2.9:

$$\Delta\theta = 1.22 \times \frac{\lambda}{D}[\text{radians}] \tag{2.9}$$

where λ and D must be expressed in the same units of length (Kutner 2003). This equation shows that the amount of diffraction is inversely proportional to the diameter of the primary aperture. Therefore, for a large telescope, the diffraction becomes minimal and certainly not the resolution limiting factor, as atmospheric effects will dominate.

In Figure 2.7 there are two point sources; to the left, the two point sources have a separation larger than the Dawes' limit and can therefore be resolved while on the right, the two point sources are irresolvable as their separation is less than the Dawes' limit.

Magnification

The third function of an optical telescope is magnification. The magnifying power (MP) of a telescope is defined as the apparent increase in angular size of an object when viewed through a
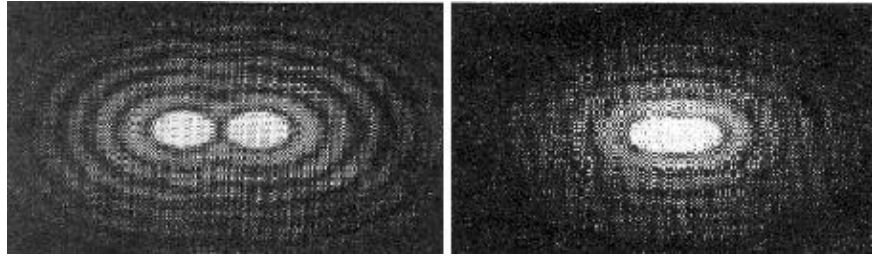
Figure 2.7: Demonstration of Dawes' / Rayleigh's limit (reproduced from Newsam (2006)).

telescope, compared with the direct view of the same object. From the geometry of Figure 2.1 it can be shown that the magnification is equal to the ratio of the focal length of the objective to the focal length of the eyepiece, given by Equation 2.10:

$$\text{MP} = \frac{f_o}{f_e} \tag{2.10}$$

where f_o is the focal length of the objective and f_e is the focal length of the eyepiece expressed in the same units of length.

In practice there is an upper and lower limit on the useful magnification of a telescope. The upper limit is approximately twice the aperture size and is set by the effects of diffraction on the image. The lower limit is set by the size of the **exit pupil** which is the name given to the size of the circular image or beam of light formed by the eyepiece of the telescope. An exit pupil larger than that of the human eye will waste the light and the image will not appear any brighter as the magnification is reduced (Zeilik 1981).

2.4   Limitations of Ground Based Optical Astronomy

The resolving power of a large ground based telescope is not limited by its optics but by the Earth's atmosphere. While the atmosphere provides us with the oxygen and shields us from harmful radiation such as ultraviolet radiation and x-rays, to an optical astronomer the atmosphere is the principal problem.

Historically, observatories were placed in locations which were convenient for access, such as

near university campuses. Universities had astronomers, and their use of the facilities was limited to the number of clear nights. Today proximity to the parent institution has become of low importance. With large investments made by governments, universities and private funds in the building of large telescopes with state of the art technology, it is normal to expect a higher level of utilisation. This requires the building of an observatory only after extensive investigation has been performed on the quality of the site. In order to define a high quality astronomical observing site it is important to study factors which influence the quality of ground based observations and set limitations on ground based optical astronomy. These factors also define the components of astronomical site evaluation, as the identification of the best location for an optical observatory requires the consideration of all these imposed limitations.

2.4.1   Weather and Climate

Weather and climate both affect the quality of an astronomical site. Weather is defined as the local conditions in the troposphere which have a short term effect, while climate is the long term accumulated weather patterns for a given region. An astronomical site with 'good weather' is one in which the frequency of bad weather events such as thunderstorms and cyclonic storms is as low as possible, the air above the observatory is dry and cloud cover is minimum. In order to gain confidence in the quality of the site, such weather information must be studied over periods of many years as it is this climate information that will provide us with a forecast on how weather conditions could possibly change in the near and far future.

2.4.2   Astronomical 'Seeing'

Definition of Seeing

There are a multitude of definitions that can be found for the term 'seeing'. Wikipedia provides a simple definition:

> Astronomical seeing refers to the blurring and twinkling of astronomical objects,
> such as stars, caused by the Earth's atmosphere. The astronomical seeing condi-

tions on a given night at a given location describe how much the Earth's atmosphere perturbs the images of stars as seen through a telescope (Wikipedia 2006).

Cause of Seeing

Turbulence produces the seeing effect. The mixing of parcels of air of different temperatures, and therefore densities, produces variations in the refractive index of the atmosphere. This is because the air's refractive index is a function of its density and therefore temperature. The temporal and spatial variations in the refractive index generate distortions in the wavefront of light reaching the telescope's mirror, thus producing the motion, blurring and scintillation (commonly called "twinkling") of the focused image. The **Fried parameter** (r_0) is the typical diameter of the refractive-index fluctuations and may be used to characterise the seeing effect.

In simple terms, one could consider two parallel rays of light from the same star. These two parallel rays when travelling thought the Earth's atmosphere may encounter different temperature regions and be refracted to different extents. When these two rays reach the telescope's surface they will no longer be in parallel and therefore by Equation 2.3 their images will separate. When we consider all possible rays entering the telescope, the result will be an image that has been broadened and appears to scintillate. This effect is called 'bad seeing'. Seeing is considered to be at its best when the width of the focused star image and its scintillation are at a minimum and diffraction rings are clearly seen. Figure 2.8 is a representation of both good seeing and bad seeing.
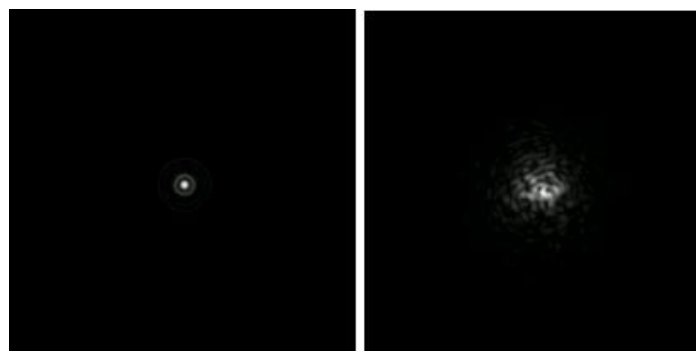
Figure 2.8: An Artificial Illustration, representing Good Seeing (left image) and Bad Seeing (right image) (reproduced from Peach (2006)).

While turbulence can occur in different layers of the atmosphere, the turbulence near the ground

layer is the greatest contributing factor to the seeing effect. This issue is of great concern to amateur astronomers as most of their observatories are located within this layer. The amount of ground layer turbulence is a function of the topography, surface roughness and surface material. The Sun heats the Earth and its objects during the day; this heat is radiated away during night time. Different materials vary in density and therefore radiate the heat differently, which results in local convection currents.

An observatory and its surroundings must be of material with a low heat capacity. This is to reduce the amount of heat stored during the day which will then produce local turbulence at night time. It is therefore best to construct an observatory of thin sheet metal, paint it white and provide adequate ventilation, while for its surroundings, uniform topography (e.g. grass and bushes or large bodies of water) is ideal.

Telescope 'tube currents' can also greatly increase the ground seeing effect. Tube currents are produced when the temperature of the objective lens/mirror of a telescope is not at the surrounding air temperature level. As a result the telescope will become surrounded by a wavy, irregular, slowly shifting envelope which is slightly warmer or cooler than the ambient night. The design of modern domes takes into consideration the importance of maintaining temperature equilibrium with surroundings to prevent the formation of tube currents.

Seeing Measurement

The distortions in the star image, caused by the turbulence in the atmosphere, change at a high rate (often at a frequency larger than 100 Hertz). In even the shortest exposure times these distortions average out as a **Point Spread Function** (PSF), called a "seeing disc". The **Full Width Half Maximum** (FWHM) of the diameter of the seeing disk is a common measure of seeing conditions at an observing site measured in units of arcseconds. Figure 2.9 represents a stellar profile, approximated by a Gaussian distribution whose image has been averaged over some seconds. The FWHM of its seeing disk is a measure of the averaged seeing value. This is not to be confused with the Airy disk, which as will be shown in Chapter 4, defines the resolution limitation imposed by the telescope.

Because seeing fluctuates with atmospheric conditions, it is defined as a variable quantity
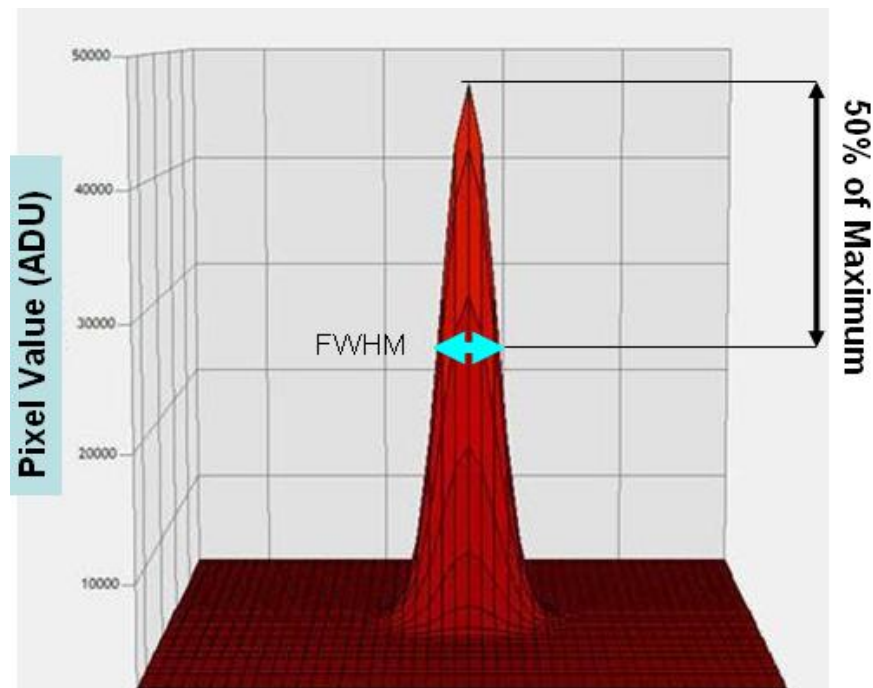
Figure 2.9: The Stellar Profile of a Star approximated by a Gaussian Distribution (adapted from Bennion (2006)).

whose value can change over a night, and over the year. Because of its variable nature only long term seeing measurements are representative of the true seeing value at a particular site.

2.4.3 Transparency and Extinction

Transparency

Atmospheric transparency refers to the extent at which the Earth's atmosphere transmits light from celestial objects. The transparency is a function of the amount of absorbing material in the atmosphere, the most common of which is dust. The quantity of dust in the air is a function of the altitude of the observing site, its proximity to a dust source and prevailing wind currents. Other suspended particles which affect the transparency are condensation nuclei (small particles upon which cloud droplets form), fog, mist and solid particles in suspension (generally the by-product of combustion). In general, transparency improves with altitude and is at its best above the inversion layer, as the cold layer close to the ground traps much of the absorbing material.

Extinction

Atmospheric extinction refers to the absorption of radiation by the air, and is a function of both the wavelength of light and airmass. One airmass is defined as the amount of air directly above an observer looking at the zenith (the local vertical). As we move from the zenith towards the equator the airmass increases by the secant of the zenith angle. As a result, photons of light travel a greater path length through the atmosphere which increases the absorption and scattering of the photons as they collide with atoms, molecules and suspended particles. Consequently the observer detects fewer light rays from the star, an effect which is called 'dimming'. Rayleigh scattering, ozone extinction and aerosols contribute the greatest to atmospheric extinction.

2.4.4 Night-Sky Radiation

Night sky radiation provides a background against which faint objects can be detected only with difficulty. Because of the inherent photon nature of light, the night sky light produces noise, making it more difficult to detect the signal from the stars. The brighter the sky, the lower the signal to noise ratio and the harder it is to detect a star signal. The presence of this noise is due mainly to photo-chemical processes in the Earth's ionosphere while other contributing factors include the sunlight scattered by interplanetary matter in the solar system, scattered starlight, diffuse radiation from the galaxy, and light from other galaxies.

2.5 An Ideal Site

Having discussed the limitations of ground based optical astronomy we can now arrive at a definition for an ideal astronomical observing site. A site can be classified as a high quality site if:

- the occurrence of bad weather is minimal;

- cloud cover is very infrequent;

- night sky radiation is at a minimum;

- site is at high altitude;

- the air above the observatory is dry;

- atmospheric turbulence is low;

- atmospheric transparency is high.

These items are local conditions and therefore vary greatly from one site to another. From a study of the location of the world's modern large telescopes, one can observe that almost all these telescopes are positioned on mountain tops which are mainly located above the inversion layer with a stable laminar air flow from the oceans. Temperature inversion is a major factor in choosing a site for professional astronomy. An inversion occurs when cooler air is located near the ground and the warmer air settles above. This orientation suppresses the formation of local convection resulting in dry, stable and generally cloud free air above the inversion layer.

Mauna Kea

Mauna Kea is the best observing site in the Northern Hemisphere. It is located in the middle of the Pacific Ocean on the island of Hawaii and is a dormant volcano towering over 40% of the Earth's atmosphere (Kea 2006). As shown in Figure 2.10, the peak, with an elevation of 4.2km, is located well above the tropical inversion cloud layer which is about 600 metres thick. This ensures that the atmosphere above the mountain remains dry and free from atmospheric pollutants and clouds. Mauna Kea has one of the highest proportions of cloud free nights, which allows for its full utilisation throughout the year. Its exceptional atmospheric stability and distance from city lights allow for detailed studies that are not possible elsewhere. The three main optical telescopes at the peak of Mauna Kea are the Keck, Gemini and Subaru telescopes. The Keck is two telescopes each 10 metres in aperture. The Gemini telescopes consist of two separate 8.1 metre telescopes. Only one Gemini telescope is located at this site while the other is on Cerro Pachon in Chile. The Subaru telescope is an 8.3 metre telescope (Kea 2006).

Figure 2.10: The Mauna Kea Summit is located well above the Cloud Inversion Layer (reproduced from Kea (2006)).

Chile

Major observatories have been developed in the Chilean Andes. The northern half of the Andes runs next to the Atacama Desert, which is one of the world's driest with no recorded rainfall in over a century. High altitude, clear weather, dry air and no light pollution have made these sites the best in the Southern Hemisphere for ground based optical astronomy. The three major observatories developed in the Andes are the European Southern Observatory (ESO), the Cerro Tololo Interamerican Observatory and the Las Campanas Observatory. The ESO has also gained another site, Cerro Paranal, farther into the desert for the Very Large Telescope (VLT), a group of 4 separate 8.2 metre telescopes (Kutner 2003).

Antarctica

Preliminary studies of Antarctica's high plateau regions completed by Ashley et al. (2004) from the School of Physics, University of New South Wales, identify this region as one of the best sites for astronomical observations. Ashley et al. (2004) site testing focused on Dome C, which is a local high point at an altitude of 3260m. Complete lack of aerosols and dust

particles, good proportion of clear skies, low average wind speeds, stable wind directions, absence of lightning, and superb seeing conditions are some of the advantages of the Antarctic plateau for astronomical observations. On the other hand, the net amount of dark time is less than at mid-latitude sites and there is less overall sky coverage, while extremely low temperatures pose difficulties and limitations on instrumentation design (Ashley et al. 2004).

2.6   Chapter Summary

Lenses and mirrors are the basic tools of optical astronomers. Both reflective and refractive telescopes are used by optical astronomers, but refractive telescopes have a lens size limitation on their effectiveness which should not be exceeded. Large astronomical telescopes are built as reflecting telescopes. F-ratio, plate scale, light gathering power, resolving power and magnification were defined as the fundamental parameters of optical astronomy. These parameters will later be used in the evaluation of the available instrumentation for low cost seeing measurements.

Ground based optical astronomy is limited by the Earth's atmosphere. Weather, seeing, night sky radiation, atmospheric transparency and extinction are all ways in which the atmosphere affects the quality of astronomical observations, all of which also define the components of astronomical site testing. Mauna Kea in Hawaii and the Chilean Andes have been identified as the world's best observing sites. The high plateaus of Antarctica appear likely to join them, but much further research and site testing is required before we can boldly make such a classification.

This chapter has equipped the reader with fundamental background knowledge on optical astronomy and the components of a site survey. Much of these principles will be referred to through out the project, with the low cost measurement of astronomical seeing as the main focus. The next chapter aims to evaluate the past and present techniques and technologies used for the measurement of seeing in order to arrive at a low cost seeing measurement technique.

Chapter 3

Past and Present Methods for the Measurement of Seeing

3.1   Chapter Overview and Rationale

Ever since the problem of astronomical seeing was identified, astronomers have always been interested in being able to measure the seeing. The initial methods were empirical, relying on the human eye to see detail and make measurements. Because of the subjective nature of these visual methods, they often yielded different results, thus making comparisons between observatories difficult. With their advent, photographic emulsions were used to make a permanent record of the seeing, thus allowing a quantitative measurement of seeing to be made. These days the primary detection system used for optical astronomy is the Charged Coupled-device (CCD) which, in combination with computer processing power, has provided us with new techniques to accurately measure the astronomical seeing.

This chapter evaluates the past and present techniques and technologies used for the measurement of astronomical seeing. This study aims to identify the most appropriate technique for the low cost measurement of seeing. Due to the absence of an accessible, universal review on the practice of seeing, this chapter amalgamates all past and present seeing practices within the three categories of visual, photographic and digital.

While the current seeing measurement systems are not wholly suited for the low cost measurement of seeing in the Southern Hemisphere, the measurement of the Full Width Half Maximum (FWHM) of the stellar profile obtained through stellar imaging or stellar trail imaging was found to be the appropriate technique in terms of available equipment and the low cost criterion.

3.2 Visual

The visual method uses a scaling system to provide a qualitative measurement of astronomical seeing. Although many astronomers have in the past devised their own seeing scales, the **Pickering seeing scale** and the **Antoniadi scale** have been the two most popular scales used by astronomers. With qualitative measurements astronomers look through their telescopes at the zenith for a two to three magnitude star and from the appearance of the diffraction pattern (Pickering scale) or the jitter of the star (Antoniadi scale) they estimate the seeing.

3.2.1 Pickering Seeing Scale

Devised around 1910 by the American astronomer W.H. Pickering using a 5 inch refracting telescope, the Pickering Seeing Scale is the most detailed seeing scale. Pickering based his seeing scale on the appearance of the diffraction rings. The ten Pickering ratings were ordered from worst to best and are as follows (Christensen 2003):

1. Star image usually about twice the diameter of the third diffraction ring.

2. Image occasionally twice the diameter of the third ring.

3. Image about the same diameter as the third ring.

4. Central disc often visible, parts of the rings can be seen as arcs occasionally on bright stars.

5. Central disc always visible, arcs frequently seen on bright stars.

6. Central disc always visible, short arcs constantly seen.

7. Central disc sometimes sharply defined with either rings appearing intact or as long arcs.

8. Central disc always sharply defined with either long arcs or complete rings seen but in constant motion

9. Complete rings always seen but the innermost ring is stationary and the outer rings momentarily stationary.

10. Complete diffraction pattern is stationary.

Figure 3.1 is an artificial illustration produced by amateur astronomer Damian Peach (Peach 2006) where each image represents one of the ten Pickering Scales.

Some observers have grouped the ten values used in the Pickering scale and formed a new scale with only four values. The four scale values were devised based on Dawes' limit (see section 2.3.2) and are as follows (Christensen 2003):

1. Very bad seeing. Can at best separate stars at three times Dawes limit. (Pickering scales 1-3)

2. Poor seeing. Can at best separate stars at roughly twice Dawes limits. (Pickering scales 4-5)

3. Good seeing. Can sometimes reach Dawes limit. (Pickering scales 6-7)

4. Excellent seeing. Can reliably reach Dawes limit. (Pickering scales 8-10)

3.2.2   Antoniadi Scale

The Antoniadi Scale was devised by the Greek astronomer E.M. Antoniadi in the early twentieth century. Antoniadi used the movement of the image as the main measure to evaluate seeing. Although his method produced a simpler scaling than that of Pickering, his scale was more subjective. The Antoniadi scale is in reverse order to that of Pickering, organised from the best to the worst seeing, given as follows (Christensen 2003):

1. Perfect Seeing, image stable without a quiver.
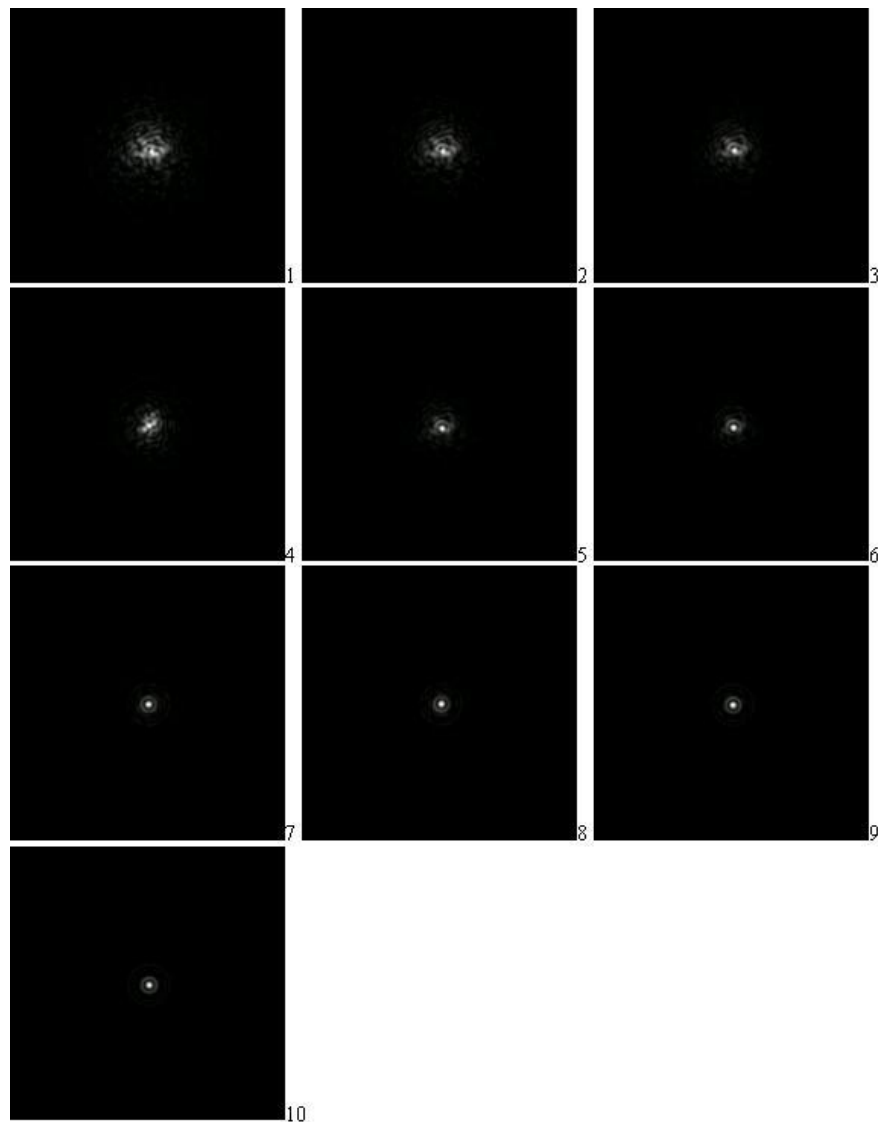
Figure 3.1: A Graphical Representation of the 10 Pickering Ratings. The diagram follows the order of the Pickering scale. (adapted from Peach (2006)).

2. Slight undulations, with moments of calm lasting several seconds.

3. Moderate seeing, with large tremors.

4. Poor seeing, with constant troublesome undulations.

5. Very bad seeing, scarcely allowing the making of a rough sketch.

Evaluation

Visual measurements are no longer an appropriate seeing measurement technique, because these seeing scales rely on the ability of the observer to see detail and are therefore highly subjective. In addition, the eye time constant is either too long to freeze the seeing effects entirely (required at low turbulence) or too short to integrate them (required at high turbulence) and therefore visual estimates are optimistic when turbulence is slow and pessimistic when turbulence is high.

3.3   Photographic

Anecdotal evidence suggests that photography of star trails has been used in the past as a technique to measure the seeing at an astronomical site. Although a thorough search was performed in order to obtain documented evidence of this practice, only one relevant paper was obtained. This paper dated back to 1965, where Harlan and Walker from the Lick Observatory at the University of California pursued *the development of a suitable test instrument that can be used at remote sites to determine what the appearance of a star image in a large telescope would be* (Harlan & Walker 1965).

3.3.1   The System of Harlan and Walker (1965)

System Description

The primary factor which the design of their instrument was based upon was the ability to operate it at remote sites. As a result, portability, a simple and rugged construction, rigid mounting, simplicity of operation and minimal power needs formed the system's physical requirements. This instrument measured seeing photography, which not only eliminated the need for electrical power but also satisfied the simplicity criteria of its design.

Polaris, the Northern Hemisphere pole star, was selected as the target star. Selecting a single star for seeing measurements allowed for the telescope to be based on a fixed mounting thus reducing the effect of wind shake. To ease the ground seeing effect (see section 2.4.2) the

telescope objective was placed seven feet (2.13m) above the ground and the mounting was situated on top of a sharp ridge with a steep drop-off.

The selection of the system components had to ensure that the equivalent focal length and film/plate resolution is large enough to produce a trail sufficiently resolvable. The system optics was a telescope with a 6.5-inch (165mm) aperture and 75.75-inch (1924mm) focal length. The telescope was visually focused on Polaris, and to maintain consistency this operation was performed by the same observer each night. Once focused, the eyepiece was removed and replaced by an assembly consisting of an eyepiece of about 18mm focal length followed by an Exakta Exa II camera system. The Exakta was a pioneer brand camera produced in Germany from 1912 to 1970 and certainly one of the better options at that time. The spacing of the eyepiece and camera body was such that the scale on the 35mm film in the focal plane of the camera was enlarged 7.5 times over the scale in the focal plane of the objective and equalled 15.5 arcseconds per mm. The exposure length was set to ten minutes which time was sufficient to carry Polaris out of the field of view of the camera.

Data Processing

The star trail images obtained were magnified to the point where seeing determined the resolution or that under the best atmospheric conditions resolution was set by the diffraction disk of the star. Harlan & Walker (1965) decided to correlate the star trails obtained with the seeing observed at the 120-inch (3m) telescope present at the Lick Observatory. To achieve this, for each star trail obtained, the star image diameter was measured simultaneously using the 120-inch reflector telescope in combination with a spectrograph. In a spectrograph the width of the spectral lines are affected by the seeing and can be measured to determine the seeing value. The correlation showed that the seeing indicated by the 6.5-inch telescope was at times poorer and at times better than that observed using the 120-inch telescope. The variations in the seeing value are due to the fact that seeing is a property of the path the light traveled, and while the values obtained from both methods, over long time periods, are representative of the site seeing conditions, it must be made clear that even slight variations between the telescope surroundings or their heights can influence the seeing value.

Figure 3.2 displays the star trails of Polaris with corresponding estimates of the image

diameter from the 120-inch reflector telescope-spectrograph. The longest trails correspond to exposures of 8.6 minutes and the scale of the reproduction is 0.8 arcseconds per mm. With knowledge of the scale and by measuring the width of the trail along the trail length, an average seeing value can be calculated. As we move to worst seeing values the changes in the width, density and frequency of wiggles in the star trail become obvious. The simple rule is that the thinner a star trail and the less its jitter, the better the expected seeing value.

Figure 3.2: Star trails of Polaris with estimates of the Stellar Image Diameter using the 120-inch Telescope (adapted from Harlan & Walker (1965)).

Evaluation

Harlan & Walker (1965) successfully built and tested a system which was cheap and simple while providing an objective estimate of the seeing. The fixed mounting would not be practical for the Southern Hemisphere where the lack of a bright Pole Star requires the telescope to have the flexibility to be pointed at other parts of the sky such as the galactic plane (i.e. plane of the Milky Way) where stars with a similar apparent magnitude as Polaris are more frequent. A rigid mounting is, however, of great importance when performing star trail photography to measure seeing, as wind shakes will add to the jitter and widen the trails, thus increasing the error in the measurements.

3.4   Digital

The digital method for the measurement of seeing may be divided into two categories, named **absolute image motion monitors** and **differential image motion monitors**. The absolute image motion monitors provide quantitative seeing measurements by measuring the variations in a single wavefront, producing a measure on how seeing changes over time. The **All Weather Seeing Monitor** may be classified as an absolute image motion monitor. While information from an absolute image motion monitor is more easily converted into an absolute seeing disk size, such systems are sensitive to tracking errors and telescope vibrations. The **differential image motion monitors** measure the seeing by measuring the difference between two wavefronts, hence provide an instantaneous seeing value. Due to their differential nature they are insensitive to tracking errors and telescope vibrations, hence providing a more accurate seeing measurement.

3.4.1   All Weather Seeing Monitor

The All Weather Seeing Monitor is manufactured by the Santa Barbara Instrument Group, Inc (SBIG) (SBIG 2005) and can be used to determine the quality of seeing each night. Due to its absolute measure of the image motion the monitor requires a rigid mounting in order to reduce errors due to wind shake and vibration. The seeing monitor is designed to use Polaris as its target star.

System Description

The Seeing Monitor is enclosed in a weather proof box with a clear window on the top, which is heated to prevent condensation on the outside surface of the glass (see Figure 3.3).

The lens system used in the Seeing Monitor has a 150mm focal length and an f-ratio of 5.3. This system is coupled to a modified version of SBIGs ST-402ME CCD Imaging Camera. This modified version does not use any form of cooling to reduce the dark current as this need was made redundant by using short exposure times. The camera was also designed shutterless which means that the CCD is constantly being exposed even at read out, hence the streaks

Figure 3.3: SBIGs Seeing Monitor (reproduced from SBIG (2005)).

below Polaris seen in Figure 3.4.

The ST-402ME uses a Kodak KAF-0402ME CCD image sensor chip. A summary of the relevant CCD specifications is tabulated in Table 3.1 (SBIG 2004).

Table 3.1: KAF-0402ME Specifications

Pixel Array	Number of Pixels	Pixel Size	CCD size (mm)	Peak QE	Full Well Capacity
765×510	390,000	9μm	4.6×6.9	83%	100,000e -

The Seeing Monitor is designed to capture the full orbit of Polaris about the North Celestial Pole. Polaris is at a declination of $+89°15'51''$ and the North Celestial Pole has a declination of $+90°00'00''$ [1]. From the declination of Polaris we can arrive at its angular separation (δ) with the North Celestial Pole. Twice this value is the minimum field of view (FoV) that SBIG would have needed to provide in order to capture the full orbit of Polaris. Figure 3.4 shows a sequence of superimposed images captured over one night (SBIG 2005). The North Celestial Pole is located at the centre of the marked circle.

The angular separation and field of view have been marked in Figure 3.4 and are calculated as follows:

$$\delta = (90°00'00'') - (89°15'51'') = 2709''$$

$$\text{FoV} = 2 \times \delta = 1.5°$$

---

[1]The declination of a star is comparable to latitude projected onto the celestial sphere and is measured in degrees north and south of the celestial equator (positive for the Northern Hemisphere and negative for the Southern Hemisphere)
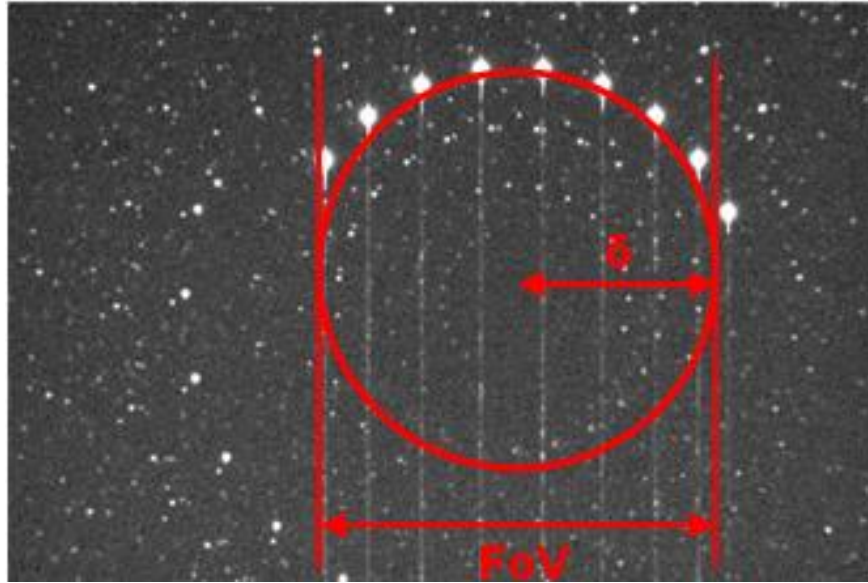
Figure 3.4: A Polaris Star Trail, produced from the superposition of many images (adapted from SBIG (2005)).

which sets the minimum FoV required by the Seeing Monitor. The actual Seeing Monitor FoV can be calculated using data from Table 3.1. The field of view is directly related to the CCD size and the focal length of the system optics. By modifying Equations 2.4 or 2.5 into Equation 3.1 we can calculate the FoV in radians.

$$s = \text{FoV} \times f \tag{3.1}$$

$$\text{FoV} = \frac{s}{f} = \frac{4.6\text{mm}}{150\text{mm}} = 0.0307\text{rad} = 1.75\,^\circ$$

This calculation therefore demonstrates the importance of sufficient FoV when designing for a non-tracking system. The resolution (ϕ) of the Seeing Monitor is related to the pixel size of the CCD and the focal length of the system optics, which can be calculated by modifying Equation 3.1 in order to obtain the scale plate for a single pixel. The resolution, provided by Equation 3.2, measures the angular fraction of the sky covered by one pixel in units of arcseconds per pixel.

$$\phi = \frac{s}{f} \times 206265 \tag{3.2}$$

$$\phi = \frac{0.009\text{mm}}{150\text{mm}} \times 206265 = 12.38 \text{ arcsecpixel}^{-1}$$

Ideally one would expect a resolution in the order of a fraction of an arcsecond per pixel in order to be able to measure useful seeing values. It is believed that SBIG have improved the resolution of the Seeing Monitor by performing centroid calculations in the order of 1/30th of a pixel accuracy, though no information on this technique has been provided.

Data Processing

The Seeing Monitor measures the seeing by measuring the horizontal jitter in the position of Polaris at high speed. The software then uses a set of equations to calculate the FWHM. In order to measure the jitter the CCD is being read out in Time Delay and Integration (TDI) mode.

The standard method of CCD imaging referred to as 'point and shoot', is to point the telescope at the target, track the telescope at the sidereal rate and integrate with the detector for the required time period. Once the required integration period is reached the shutter is closed and the CCD is read out. However in TDI mode the imaging system remains stationary, the shutter is left open and the readout is continuous (Howell 2000). The TDI readout image of Polaris is displayed in Figure 3.5. If looked at carefully, two effects become obvious: first is the fluctuation in the brightness due to the scintillation of the star; the second effect, which is not as clear, is the horizontal deviation in the position of Polaris due to the seeing effect. It is this motion that is detected by the software which is used to calculate the FWHM, corrected at the Zenith. A fast readout, in five millisecond intervals, prevents any undersampling of the seeing jitter.
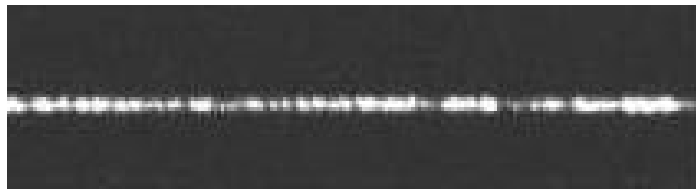
Figure 3.5: A TDI readout of Polaris (adapted from SBIG (2005)).

Evaluation

SBIG have successfully developed a seeing monitor which can be left outdoors for an indefinite period of time with minimum maintenance. Its simple and low maintenance design, combined with its remote operation, allows for seeing measurements to be taken for indefinite periods of time, and at a cost of U.S.\$1995.00 (OPT 2006) it is ideal for low cost measurement of seeing.

SBIG's Seeing Monitor, designed to use Polaris as its target star, is suited for the Northern Hemisphere. Sigma Octantis is the closest star to the South Celestial Pole and is considered as the Southern Hemisphere pole star. The South Star is a magnitude 5.42 star and compared to the North Star, Polaris, with an apparent magnitude of 1.97, it is a much fainter star. Zeilik (1981) provides a conversion from brightness ratio to apparent magnitude and vice versa. For two stars of apparent magnitudes m and n with respective apparent brightnesses I_m and I_n, their ratio of brightnesses I_n/I_m corresponds to the magnitude difference $m - n$ as follows:

$$\frac{I_n}{I_m} = 100^{(m-n)/5}. \tag{3.3}$$

Applying this relationship to the pole stars we have:

$$\frac{I_n}{I_m} = 100^{(5.42-1.97)/5}$$
$$= 24$$

which we conclude that Sigma Octantis is 24 times fainter than Polaris. This makes Sigma Octantis a poor pole star compared to Polaris. The Seeing Monitor is not an option for the Southern Hemisphere as by applying Equation 2.6 (i.e. light gathering power is proportional to the square of the telescope's aperture) a Southern Hemisphere equivalent to the SBIG's Seeing Monitor would require an aperture approximately 5 times as large.

3.4.2 Differential Image Motion Monitor

The Differential Image Motion Monitor (DIMM) is the most widely used method for seeing measurements and is based on the study of the differential motion of the image of a star. Much of the theory of atmospherically generated seeing was described by Roddier in 1981 (Sarazin & Roddier 1990). Following the advice of Roddier the European Southern Observatory decided to develop the first DIMM.

System Description

In section 2.4.2 we identified that the presence of turbulence in the atmosphere caused the stellar image formed by a telescope to move randomly. The DIMM method consists of measuring incoming wavefront slope differences over two small pupils some distance apart. A mask with two small circular sub-apertures is placed at the entrance of a small telescope, allowing for star light to travel through. The idea behind this design is that the light from a star passing through the two sub-apertures has travelled through slightly different atmospheric conditions, thus producing a tilt in the wavefront of one compared to the other. The size of the sub-apertures and their separation is critical to the accuracy of the results obtained. Improved results over the absolute image motion monitor are obtained only if the distance between the two sub-apertures exceeds their diameter by a few times. For a typical DIMM the two images are formed through the two sub-apertures of approximately 5cm diameter, and a separation of approximately 20cm (Wood, Rodgers & Russell 1995).

Using the DIMM instrumentation, the two images of a single star are recorded on the CCD camera detector. A small deflection is produced in one of the incoming light beams by placing a thin optical wedge in one of the sub-apertures causing two spatially-separated images to form on the CCD. Figure 3.6 displays the general layout of a typical DIMM system. A DIMM system consists of a small telescope, DIMM mask, CCD camera and a computer for image processing
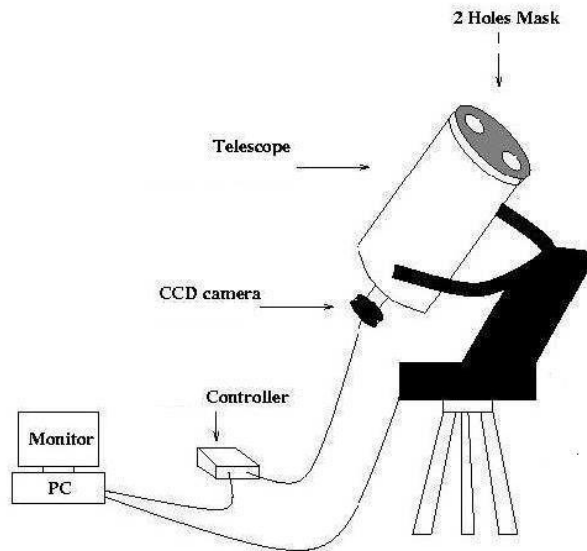
Figure 3.6: Schematic diagram of a typical DIMM setup (adapted from Wood et al. (1995)).

Data Processing

The aim of the data processing in a DIMM system is to convert the relative motion of the dual star image in the image plane into an absolute seeing scale. The absolute seeing scale is the FWHM.

For each captured frame the position of the image centroids are computed and the offset of one image from the other is calculated in both the longitudinal direction (between the two holes) and transverse direction. From a series of many images (minimum 100 frames) the mean image separations are obtained and the variance of these separations in both longitudinal and transverse directions is calculated (Dopita et al. 1996). An expression of the variances of centroid dispersion in both longitudinal and transverse directions takes into account the diameter of the sub-apertures on the DIMM mask and their separation and is given in Equations 3.4 and 3.6. These relationships have been derived in Appendix B as described by Roddier in 1981 (Sarazin & Roddier 1990). From these relationships we can arrive at the variance of the differential image motion (σ^2). The longitudinal variance is:

$$\sigma_l^2 = K_l \lambda^2 r_0^{(-5/3)} \tag{3.4}$$

$$K_l = 2[0.179D^{(-1/3)} - 0.0968d^{(-1/3)}] \tag{3.5}$$

and the transverse variance is:

$$\sigma_t^2 = K_t \lambda^2 r_0^{(-5/3)} \tag{3.6}$$

$$K_t = 2[0.179D^{(-1/3)} - 0.145d^{(-1/3)}] \tag{3.7}$$

where λ is the wavelength of light, D is the diameter of the sub-aperture and d is the separation between the two sub-apertures. All lengths are measured in centimetres and the variance is in radians (Sarazin & Roddier 1990).

The FWHM value can then be obtained from the variance of relative image motion calculated in Equations 3.4 and 3.6. Two FWHM measurements are made: a longitudinal one in the direction of the sub-aperture axis called Full Width Half Maximum Longitudinal ($FWHM_l$) and a transverse one that is perpendicular called Full Width Half Maximum Transverse ($FWHM_t$). The FWHM at the zenith is related to the variance of the image motion and its value measured in either direction, (subscript $*$ representing either longitudinal or traverse directions), is given in Equation 3.8.

$$FWHM_*[\text{radians}] = 0.976\lambda^{(-1/5)}(\frac{\sigma_*^2}{K_*})^{(3/5)} \tag{3.8}$$

Equation 3.9 calculates the value of seeing (in radians) at any point of time using the DIMM method. Its value is equal to the average of the $FWHM_l$ and $FWHM_t$ measurements, which must then be converted into arcseconds for an appropriate representation of the seeing measurement.

$$FWHM = \frac{1}{2}(FWHM_l + FWHM_t) \tag{3.9}$$

Use of the DIMM system here in Australia was made by Wood et al. (1995). The seeing measurements they made found that the seeing at Freeling Heights and at Siding Spring

Observatory both to be around 1.2 arcseconds (Wood et al. 1995). Figure 3.8 shows the seeing at Siding Spring through each night during which measurements were made. Figure 3.7 shows the histogram of seeing measures at Siding Spring, where all individual measurements were used.
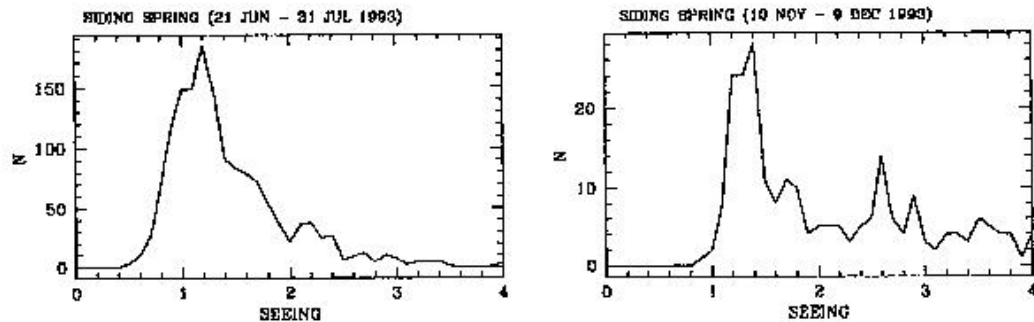
Figure 3.7: Histogram of seeing measurements at Siding Spring (reproduced from Wood et al. (1995)).

Evaluation

While DIMM systems produce the most accurate seeing measurements due to their differential nature, certain complexities make them less favourite for a low cost seeing measurement system. In order to obtain a seeing measurement which is representative of that particular site, seeing measurements need to be taken on a continuous basis for many months. The use of the DIMM is a labour intensive process. It requires the permanent attendance of an operator, which makes it a tiresome and expensive process for continuous operation. This also becomes a larger issue when the interest is in comparing multiple sites, therefore requiring simultaneous measurements. Seeing measurements at MKO have previously been made by Moller using the DIMM method. He recorded an average seeing value of 1.22 arcseconds (Moller 1996). This value was measured over a period of only two nights and is therefore not an accurate representation of the typical seeing at MKO. DIMMs require bright stars to get high time resolution as a result they are not suited to an un-driven telescope mount. This further limits the practicality and ease of use of the DIMM system.

Automated DIMMs (ADIMMs) solve some of the impracticalities associated with the DIMM. They generate automatic seeing measurements throughout each observing night, and collection of data is no longer dependent on the presence of an operator for each observing
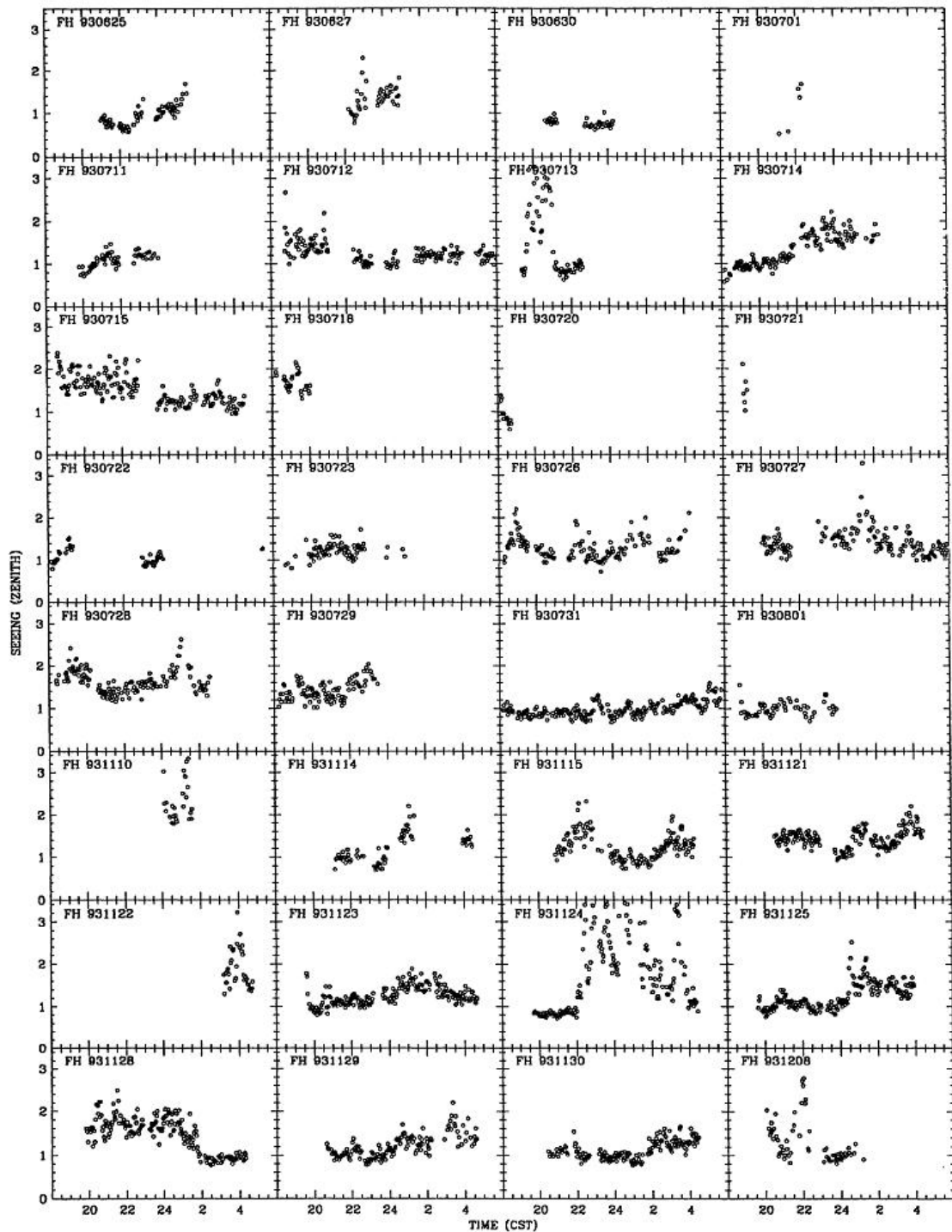
Figure 3.8: Seeing at Siding Spring plotted against Australian Central Standard Time (CST) (reproduced from Wood et al. (1995)).

night. Characteristics of such a system include: automatic selection of targets, pointing of the telescope and tracking of targets, and acquisition and processing of the data. It also requires the telescope to be placed inside an automated dome with a reliable power supply. These

autonomous systems have the obvious disadvantage of a much higher cost compared to a DIMM. The Automated Antarctic DIMM, part of the Automated Astronomical Site Testing Observatory (AASTO), is one such example where autonomous operation at very low temperatures is a key requirement (Dopita et al. 1996).

3.5 A Low-Cost Seeing Measurement Technique

SBIG's Seeing Monitor was identified as not suitable for the Southern Hemisphere while the DIMM measurement of seeing presented itself as a hands-on technique requiring the devotion of substantial observatory resources. Hence both methods are not suitable for a low cost implementation. Seeing measurements based on the **measurement of the FWHM of the stellar profile** obtained through **stellar imaging** or **stellar trail imaging** is therefore the appropriate low cost technique. This technique will also allow for the utilisation of the equipment made available by the University.

3.6 Chapter Summary

This evaluation of past and present methods for the measurement of seeing has amalgamated all seeing practices within the three categories of visual, photographic and digital. The visual method is a qualitative measurement that, owing to its subjective nature, provides inaccurate results, often varying between observers. Although the two scaling systems used detail to increase the accuracy of the visual method, they remained highly subjective. Photography of star trails allowed for seeing information to be recorded and a quantitative measurement to be made. Unfortunately, due to the shortage of literature on this topic, the discussion focused on one particular event only, where a simple and low cost design successfully produced an objective seeing value. SBIG's low maintenance, remotely operated and easy to use Seeing Monitor allows for seeing measurements to be taken for indefinite periods of time. However its operation is limited to the Northern Hemisphere due to the lack of a pole star in the Southern Hemisphere. The DIMM system was invented to produce accurate seeing measurements due to its differential nature; however its complex and labour intensive nature made it less suitable for continuous seeing measurements.

The measurement of the full width half maximum (FWHM) of the stellar profile obtained through stellar imaging or stellar trail imaging was found to be the appropriate technique in terms of available equipment and the low cost criterion. The next Chapter evaluates the capabilities of the equipment made available by the university for the measurement of seeing. This evaluation is based on the three identified critical design factors, namely field of view, signal to noise ratio and resolution.

Chapter 4

Evaluation of the Available Instrumentation Based on the Critical Design Factors

4.1   Chapter Overview and Rationale

This chapter explores in detail the capabilities of the available equipment to measure the seeing down to 1 arcsecond and with an accuracy of 0.5 arcseconds (i.e. as required by the project specification) based on the measurement of the FWHM of a stellar profile. In Chapter 3 it was concluded that SBIG's Seeing Monitor was not suited to the Southern Hemisphere while the DIMM measurement of seeing presented itself as a hands-on technique requiring the devotion of substantial observatory resources. The measurement of seeing has hence been based on the measurement of the FWHM of a stellar profile, using a non-tracking system.

This chapter aims to investigate the three identified critical design factors, namely **field of view and stellar density function**, **signal to noise ratio** and **resolution**, in order to examine the suitability of both the digital (CCD) and photographic implementations of the low cost stellar profile imaging system. While initial investigations have shown that both implementations fail to measure the seeing to that required by the project specifications, the

identified interrelation of signal to noise ratio and resolution have provided a way forward.

4.2   Equipment

An ST-4 Star Tracker and Imaging Camera, ST-6B Imaging Camera and a 10-inch Meade
LX200 f/10 telescope were available for the digital implementation. A Nikon SLR
(Single-Lens Reflex) camera and a Celestron-5 telescope was provided for the photographic
implementation.

4.2.1   Equipment for the Digital (CCD) Measurement of Seeing

The digital imaging of a stellar profile makes use of a CCD camera as the imaging detector in
combination with an optical telescope. The system will consist of an ST-4 Star Tracker and
Imaging Camera or the ST-6B Imaging Camera, in combination with the 10-inch Meade
LX200 f/10 telescope. Characteristics of the digital imaging system which are central to an
evaluation include:

- **telescope focal length**;

- **pixel size**;

- **pixel quantum efficiency**: The quantum efficiency (QE) of a CCD is the ratio of the
  incoming photons to those stored by the device. An ideal CCD would have a quantum
  efficiency of 100% (i.e. every photon detected is accounted for in the output). A higher
  QE means that the CCD can detect fainter objects during short exposures. The earlier
  CCDs had peak QEs of 40% while the QE curve for today's CCDs peak at 90% and are
  over 60% more efficient in more than two thirds of their spectral range (Howell 2000).

- **pixel full well capacity**: The full well capacity of a pixel is defined as the amount of
  charge a pixel can hold before it becomes saturated. Before a decision is made on using
  a particular CCD its saturation time must be accounted for.

- **pixel noise contributions**: The usefulness of a detector is very often determined by the

amount of inherent noise within the device itself, so it is therefore important to identify the sources of noise in a CCD so that the signal and noise can be separated.

- The **readout noise** is defined as the number of electrons introduced per pixel into the final signal upon readout of the device. For example, a CCD with a read noise of 50 will contain on average 50 extra electrons in each pixel upon readout. There are two components to this noise. The first component is due to the digitisation of the charge. Conversions from the same pixel with the same charge will not always yield exactly the same result from the analog to digital converter. The readout would be a statistical distribution of possible answers centred on a mean value. The second component of this noise is the unwanted signals introduced by the electronics which become digitised along with the pixel charge. The average level of this additive uncertainty is the readout noise level which CCD manufacturers often specify as an rms value.

- **Dark current** arises from thermal energy within the silicon lattice containing the CCD. Thermal noise is a property of any matter at a temperature above absolute zero (-273 degrees Celsius). These electrons are created over time, independent of the light falling on the detector and are collected within the potential well of a pixel. The amount of dark current is a function of the temperature of the CCD and, as a result, CCDs are cooled either using thermoelectric coolers or liquid nitrogen. Manufacturers often specify the dark current, however the dark current noise is the statistical variation of this specification. Since dark current noise follows Poisson statistics, the rms dark current noise is the square root of the dark current, expressed in units of electrons per pixel given by Equation 4.1. As a result the total dark current noise over a short exposure time has virtually no effect on the CCD output noise.

$$\text{Dark Current Noise}_{\text{rms}} = \sqrt{\text{Dark Current}} \qquad (4.1)$$

Equation 4.2 calculates the total noise for a CCD, measured in electrons per pixel (Phtometrics 2006).

$$\text{Total Noise} = \sqrt{\text{Read Noise}_{\text{rms}}^2 + \text{Dark CurrentNoise}_{\text{rms}}^2} \qquad (4.2)$$

- **CCD gain**: The CCD gain determines how the amount of charge collected in each pixel will be assigned to a digital number in the output image. It carries the units of electrons per Analog-to-Digital Unit (ADU) which translates into the number of electrons needed to produce one ADU step. Typical values range between 1 to 150 (Howell 2000).

- **CCD array size**.

ST-4 Star Tracker and Imaging Camera

The ST-4 Star Tracker and Imaging Camera has been manufactured by SBIG (SBIG 2002a). The ST-4 is an old model and is no longer in production. The ST-4 uses a Texas Instruments (TI) TC211 charge-coupled device. The TC211 CCD contains a total of 31872 pixels arranged in an array of 192 by 165 pixels (see Figure 4.1). The pixels are rectangular and have the dimensions of 16μm by 13.75 μm (SBIG 1999).
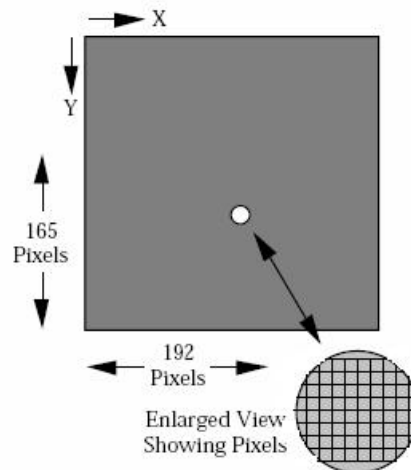
Figure 4.1: The TC211 CCD Configuration (adapted from SBIG (1999)).

The camera produces 8 bit grayscale digital images, where a full image consists of 31872 bytes. The camera operates through a microcontroller (see Figure 4.2) which can communicate with a PC over the ST-4's RS-232 serial link. This arrangement allows for a full image to be transmitted at 19.2K baud within 18 seconds over a distance of 30 metres (SBIG 2002a). The microcontroller allows for automatic tracking of the stars by calculating how far a star has drifted and generating a control signal to correct the position of the telescope in less than one second.

Figure 4.2: The ST-4 CCD and Star Tracker Imaging Camera (reproduced from SBIG (2002*a*)).

SBIG have reduced the thermal noise of the ST-4 CCD by thermoelectrically cooling it to -30 degrees Celsius and therefore allowing for the detection of dim stars. A CCD exposure of no longer than 5 minutes is recommended by the ST-4 manual as the accumulation of dark current will saturate the CCD. The dark current noise can be reduced by taking dark frames for the same exposure period used to capture an image and subtracting each dark frame from the captured image. The specifications for the ST-4 CCD camera have been summarised in Table 4.1. The manufacturer does not directly specify the quantum efficiency of the CCD. However this information has been extracted from the CCD Spectral Responsivity curve provided in the TI TC211 datasheet. The value for the quantum efficiency is given in Amperes per Watt which has been taken as an average value over the window of observation (400-700nm).

Table 4.1: ST-4 Specifications

Pixel Size	QE	Full Well Capacity	Dark Current	A/D Gain	Read Noise
μm	$A.W^{-1}$	e^-	$e^-.pixel^{-1}.s^{-1}$	$e^-.ADU^{-1}$	e^-
13.75$\times$16	0.3	80,000	250	150	150

ST-6B Imaging Camera

The ST-6B is an Imaging Camera manufactured by SBIG. The ST-6B is an old model and, as with the ST-4, is no longer in production. The ST-6B uses a TI TC-241 CCD, which contains a total of 91000 pixels arranged in an array of 375 by 214 pixels. The pixels are rectangular and have the dimensions of 23 by 27 micrometres (SBIG 1996).

The ST-6B (see Figure 4.3) is a much more advanced CCD camera compared to the ST-4. It has much reduced levels of noise, a larger pixel array, a lower A/D gain and a larger full well capacity. The ST-6 has a two stage thermoelectric cooler which reduces the amount of dark current to 10 electrons per pixel per second of exposure at -30 degrees Celsius, thus allowing for exposure times of up to 3600 seconds- much longer than that made possible using an ST-4 (SBIG 1996).

Figure 4.3: The ST-6B Imaging Camera (reproduced from SBIG (2002*b*)).

The specifications for the ST-6B CCD camera have been summarised in Table 4.2. The manufacturer does not directly specify the quantum efficiency of the CCD; however this information has been extracted from the CCD Spectral Responsivity curve provided in the TI TC241 datasheet. The value for the quantum efficiency is given in Amperes per Watt which has been taken as an average value over the window of observation (400-700nm).

Table 4.2: ST-6B Specifications

Pixel Size	QE	Full Well Capacity	Dark Current	A/D Gain	Read Noise
μm	$A.W^{-1}$	e^-	$e^-.pixel^{-1}.s^{-1}$	$e^-.ADU^{-1}$	e^-
23×27	0.4	400,000	10	6.7	23

10-inch Meade LX200

The 10-inch Meade LX200 has a focal length of 2500mm and an f-ratio of f/10. Two important aspects influenced the decision to use the Meade 10-inch. First was the fact that it was a portable telescope and second that it was compatible with a wide variety of imaging

equipment, in particular the SBIG ST-4 and ST-6B Imaging Cameras. Figure 4.4 shows the 10-inch Meade displayed on its fork mounting. The 10-inch Meade is constructed in a Schmidt-Cassegrain design. The Meade has an oversized primary mirror, allowing it to yield illuminated fields of view that are wider than those of telescopes with standard sized primaries (Meade 2006).

Figure 4.4: 10-inch Meade LX200 Telescope(reproduced from Meade (2006)).

4.2.2 Equipment for the Photographic Measurement of Seeing

The photographic imaging of a stellar profile makes use of photographic film for the imaging, in combination with an optical telescope. The photographic implementation is to be based on the measurement of a stellar trail, similar to the system set up by Harlan and Walker from the Lick Observatory (see section 3.3.1). This system consists of a Nikon SLR camera in combination with a Celestron-5 (C-5) optical telescope. Characteristics of the photographic imaging system which are central to an evaluation include:

- telescope focal length;

- film grain size;

- film quantum efficiency;

- film size.

The C-5 has a focal length of 1250mm and an aperture of 127mm (i.e 5-inch); the small size of the telescope allows for its mounting on the Nikon tripod. The use of the C-5 in combination with the Nikon camera was decided upon for two reasons: firstly the C-5's weight of only 2.77kg provides us with an easily portable system and secondly, an adapter for the connection of the Nikon camera to the telescope was available, while such an adapter for the Nikon-Meade combination had not been made.

The Nikon camera is to be used as a photographic plate, as its lens system is removed and replaced by the optics of the telescope (see Figure 4.5). The film made available was Ilford FP4 Plus black and white 35mm film, with a 6-micron grain size.

Figure 4.5: The Celestron-5 Telescope and SLR Camera.

4.3   Critical Design Parameters

Three critical design parameters for the non-tracking stellar profile measurement system have been identified:

- field of view and stellar density function;

- signal to noise ratio;

- resolution.

The design parameters must be selected for an optimised pixel angular resolution. Pixels which cover a large angle of the sky will not capture all the detail that the seeing and optics

allow and pixels too small in angular size will result in a small field of view and larger noise contributions.

4.3.1 Field of View and Stellar Density Function

The probability of capturing a star on the detector depends on both the field of view (FoV) of the imaging system and the stellar density function. While the field of view is a function of the telescope's focal length and the size of the imaging system, the stellar density function simply depends on the direction in the sky at which the telescope is pointing.

Field of View

The field of view refers to the sky area covered by an image taken with a telescope. The FoV depends on both the size of the imaging detector and the focal length of the telescope. Based on the plate scale equation (Equation 2.4) the angular area of the sky covered is inversely proportional to the focal length of the telescope. However, for our digital imaging systems, the main limitation in obtaining a wide FoV is the small size of the CCD arrays; the ST-4 has an array size of 16×13.75 microns and the ST-6B has a slightly larger array equal to 23×27 microns. The photographic system provides a larger FoV, mainly due to its much larger imaging area equal to 35mm across the diagonal of the film. (It must be noted that while the C-5 has a focal length equal to half of that of the Meade-10, this difference in focal length only improves the FoV by a factor of 2, and the main improvement in FoV is due to the larger detector size.) The ST-4 and ST-6B imaging cameras in combination with the Meade-10 have a field of view equal to 216.5 and 536.9 arcseconds respectively (see Appendix C, section C.2.1"Plate Scale" and "Field of View"). The field of view obtained by the photographic system follows similar calculations:

- Calculating the plate scale for the C-5:

$$s = \frac{\pi}{180} \times 1250$$

$$= 21.82 \text{ mm.degree}^{-1}$$

$$= \frac{21.82 \times 10^3}{3600}$$

$$= 6.06 \ \mu\text{m.arcseconds}^{-1}$$

- Calculating the FoV for the photographic system:

$$\text{FoV} = \frac{35000 \mu\text{m}}{6.06 \mu\text{m.arcsec}^{-1}}$$

$$= 5776 \text{ arcseconds}$$

Stellar Density Function

The stellar density function is defined as the star count per square degree of the sky. Star counts have been obtained from Allen (1973) who provided the average number of stars per square degree brighter than the visual magnitude m. Figure 4.6 is a graphical representation of the star counts, both at 90 degrees to the galactic plane (i.e. 90 degrees to the plane of the Milky Way) and along the galactic plane. Figure 4.6 shows that firstly the stellar density increases exponentially for an increase in stellar magnitude (i.e. a dimmer star) and secondly, the stellar density is greatest along the plane of the Milky Way and least at 90 degrees to the plane of the Milky Way.

As defined by Equation 4.3 the product of the stellar density function (N) and the field of view of the imaging system provide us with the star counts per CCD field of view (N_{FoV}). Because of the rectangular pixels of the ST-4 and ST-6B the FoV needed to be calculated along both x (FoV_x) and y (FoV_y) dimensions.

$$N_{\text{FoV}} = N \times \frac{\text{FoV}_x \times \text{FoV}_y}{3600^2} \qquad (4.3)$$
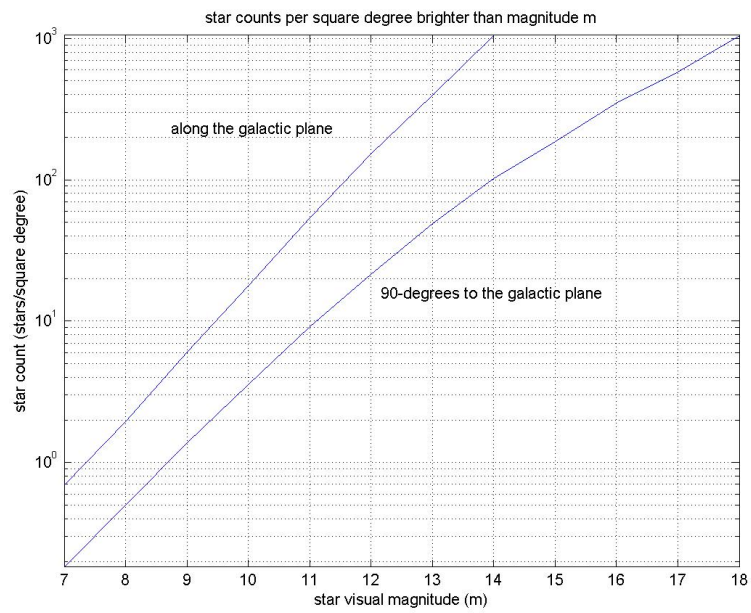
Figure 4.6: The stellar density increases exponentially for an increase in stellar magnitude (This Figure was generated from Table 117 (page 244) of Allen (1973).)

where 3600^2 provides the conversion from square degrees to square arcseconds. The following calculations illustrate the increase in the number of stars captured in the ST4 CCD FoV for the Meade-10 pointed at the plane of the Milky Way compared to when the imaging is at 90 degrees to the galactic plane, assuming a magnitude 12 target star:

- The ST-4 CCD FoV along x and y dimensions is:

$$\text{FoV}_{\text{x}} = 217.8 \text{ arcseconds}$$
$$\text{FoV}_{\text{Y}} = 216.5 \text{ arcseconds}$$

- The number of stars per square degree brighter than magnitude 12 at 90 degrees to the plane of the Milky Way are (see Figure 4.6):

$$\text{N}_{12} = 21.4 \text{ stars.degree}^{-2}$$

- Using Equation 4.3 to calculate the number of stars per CCD FoV:

$$N_{FoV} = 21.4 \times \frac{216.5}{3600} \times \frac{217.8}{3600}$$
$$= 0.078 \text{ stars.FoV}^{-1}$$

- The number of stars per square degree brighter than magnitude 12 along the plane of the Milky Way are (see Figure 4.6):

$$N_{12} = 151.3 \text{ stars.degree}^{-2}$$

- Using Equation 4.3 to calculate the number of stars per CCD FoV:

$$N_{FoV} = 151.3 \times \frac{216.5}{3600} \times \frac{217.8}{3600}$$
$$= 0.55 \text{ stars.FoV}^{-1}$$

These calculations have demonstrated that the number of captured stars in the ST-4 FoV have increased by a factor of 7 simply by changing the direction at which the telescope is pointing. The number of captured stars would also increase with longer exposure times. Hence, while the small size of the CCD FoV imposes limitations on the design of the digital stellar profile imaging system, these limitations may be overcome. For calculations on the number of 12 and 14 magnitude stars in the ST-4 field of view see Appendix C, section C.2.1, "12 and 14 Magnitude Star Count per Field of View".

4.3.2   Signal to Noise Ratio

The signal to noise ratio (S/N) is defined as the ratio of the zero to peak amplitude of the Gaussian stellar profile to the standard deviation of the noise (i.e noise count):

$$S/N = \frac{a_0}{\sigma_{noise}} \qquad (4.4)$$

where a_0 is the peak amplitude of the stellar profile, calculated as:

$$a_0 = \frac{a}{2\pi\sigma^2} \tag{4.5}$$

σ is the standard deviation of the stellar profile and holds the following relationship with the FWHM of the profile:

$$\sigma = \frac{\text{FWHM}}{2.355} \tag{4.6}$$

and a is the total signal count. The calculation of the signal count requires the measurement of the total flux of light collected from a star. This measurement is made by counting the number of electrons released by the incident photons while taking into consideration the quantum efficiency of the detector.

Signal Count

Signal count can be defined as the number of counts measured from a star of given magnitude with our equipment. It is therefore important to define the relationship between the magnitude of a star and its flux. Allen (1973) has shown that the flux per second, per unit area, per wavelength interval from a star of given magnitude outside Earth's atmosphere is given by:

$$\log \text{F} = -0.4m_v - 8.43 \tag{4.7}$$

where F is flux [erg.cm^{-2}.$\mathring{A}^{-1}$.s^{-1}] and m_v is the visual magnitude of the star. In applying Equation 4.7 the following assumptions have been made:

- seeing is perfect and light from the star falls on one pixel only;

- the flux at each 1 $\mathring{A}$ band is uniform across the wavelength interval of 400-700nm;

- the light lost due to the secondary mirror and its support structure is negligible (Schmidt-Cassegrain design of the available optical telescopes);

- the amount of flux lost due to atmospheric extinction can be ignored.

Due to the design for a non-tracking system, consideration needed to be given to an appropriate target stellar magnitude, in order to avoid the possibility of saturating the CCD pixels, in particular for stellar trail imaging. While the lower limit of the target star magnitude (i.e. brightest target star) depends on the type of imaging performed (i.e. stellar imaging or stellar trail imaging) the upper limit (i.e.faintest detectable star) for the purpose of this project will be taken as the stellar magnitude which produces a S/N equal to 1. While it is difficult to quantify a 'good' signal to noise ratio, it is shown in Chapter 5 that the appropriate S/N figure depends on the data analysis technique employed.

Lower Stellar Magnitude Limit

The calculation of the lower stellar magnitude limit is of particular concern when imaging a stellar trail as the CCD will remain exposed for the duration of the star trail. Its calculation requires knowledge of the residency time and pixel saturation time. The term 'residency time' refers to the period of time in which a star resides on a pixel [s.pixel^{-1}]. In setting the lower magnitude limit we need to ensure that the star residency time is less than the pixel saturation time or else the full well capacity of a pixel will exceed its limit causing the affected pixels to overflow.

In Figure 4.7 the saturation is noted at the location of a bright pixel with bright streaks (i.e. the excess charge) 'bleeding' along the readout columns. A saturated pixel does not contain its true value, hence its measurement is made redundant, and in the worst case the bleeding into surrounding pixels will make their measurements also useless.

The ST-4 residency time is 75.6ms and, with a full well capacity equal to 80,000 electrons, it has a saturation time of 4.8s (see Appendix C, section C.2.2:"Length of Time Star remains in CCD FoV", "Residency Time" and "Saturation Time"). These values in combination with the 16762 electrons accumulated per pixel over the residency time (see Appendix C, section C.2.2:"Star Flux" and "Electrons per Pixel"), allow for the lower limit of the stellar magnitude system to be determined:
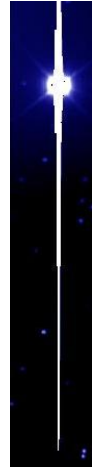
Figure 4.7: A Pixel Saturated by a Bright Star (adapted from Hainaut (1996)).

1. Determining the flux ratio (see Equation 4.7) for a one unit change in magnitude (for a star of magnitude n its flux is represented as F_n):

$$\log F = -0.4m_v - 8.43$$

$$\log F_{12} = (-0.4 \times 12) - 8.43$$

$$\log F_{11} = (-0.4 \times 11) - 8.43$$

$$\log F_{12} - \log F_{11} = 0.4$$

$$\frac{F_{12}}{F_{12}} = 2.51$$

$$\frac{F_{n+1}}{F_n} = 2.51$$

which means that for a star of one magnitude brighter the flux will increase by a factor of 2.51.

2. Replacing the saturation time with the residency time and solving for m (the number of magnitudes lower than a magnitude 12 star):

$$80,000 = 0.0756 \times 16762 \times 2.51^m$$

$$\log 63.13 = m \log 2.51$$

$$m = 4.5$$

3. Hence the lower limiting magnitude:

$$12 - 4.5 = 7.5$$

This calculation demonstrates that, for a CCD stellar trail imaging system, a target star of magnitude less than 7.5 will cause the pixels to saturate. However, for a stellar imaging system the acquisition time is less than the residency time, which allows for the imaging of bright stars of magnitudes less than 7.5. However the magnitude of the brightest target star will depend on the acquisition time.

Upper Stellar Magnitude Limit

While in theory there is no limit on the faintest detectable star, in practice the upper limiting magnitude depends on the inherent properties of the detector system. The faintest detectable star is one for which the signal to noise ratio over the exposure time reaches 1. For the ST-4 this limiting magnitude is approximately 14 (see Appendix C, section C.2.2:"Signal Count for a Magnitude 14 Star").

For a magnitude 12 target star the ST-4 CCD camera has a S/N of 12.9, while the ST-6B CCD camera provides an improved S/N of 540.8 due to its improved quantum efficiency and lower read noise, dark current noise and analog to digital gain (see Appendix C, section C.2.2:"Signal Count", "Noise Count" and "Ratio of Signal to Noise").

4.3.3   Resolution

The resolution of a star image may be limited by one or more of the following three factors:

- the Earth's atmosphere;

- optics;

- detector.

Images whose resolution is limited by the Earth's atmosphere may be referred to as 'seeing limited'. If the resolution of an image is set by the diffraction of the optics it is referred to as 'diffraction limited'. In principle, seeing limited images set the 'actual seeing value', while diffraction limited images and images whose resolution is limited to the resolution attainable by the detector set the 'theoretical seeing value'. A seeing measurement system will only

measure the seeing accurately if the system is designed such that the theoretical seeing value is below that of the actual seeing value.

Actual Seeing

The full resolving power of ground based telescopes is usually not attained owing to the deleterious seeing effects of the Earth's atmosphere, which means that the minimum resolution attainable at a particular observing site is limited by the seeing.

The project specification requires the seeing to be measured in the range of 1-10 arcseconds seeing and to an accuracy of 0.5 arcseconds. The lower limit of 1 arcsecond seeing may therefore be assumed as the actual seeing and the optics and detector system must not impose any limitations on achieving this resolution.

Theoretical Seeing

Diffraction limited resolution and detector resolution were classified as theoretical seeing values. This classification reemphasises the importance of a design in which the resolution limiting factor is the actual seeing.

Optics   As discussed in section 2.3.2, the Dawes' limit defines the diffraction limited resolution for an optical telescope, where the angular size of the diffraction disk was determined by the diameter of the aperture. Equation 2.9 has been used to calculate the Dawes' limit in arcseconds for the 10-inch Meade at the wavelength of observation (yellow light) equal to 550nm.

$$
\begin{aligned}
\Delta\theta &= 1.22 \times \frac{\lambda}{D} \\
&= \frac{1.22 \times 550 \times 10^{-9} \times 206265}{10 \times 2.54 \times 10^{-2}} \\
&= 0.54''
\end{aligned}
$$

The diffraction limitation for the Celestron-5 with an aperture diameter equal to half the Meade's will therefore equal 1.08 arcseconds. With non-diffraction limited optics and a rigid mount for the telescope, the FWHM is determined by the value of the seeing. However some blurring is contributed by each source such that the aggregate FWHM is given by (SBIG 2000):

$$\mathrm{FWHM}_{(\mathrm{aggregate})} = \sqrt{\mathrm{FWHM}^2_{(\mathrm{optics})} + \mathrm{FWHM}^2_{(\mathrm{trackingerror})} + \mathrm{FWHM}^2_{(\mathrm{seeing})}} \quad (4.8)$$

Since we require no tracking, the FWHM tracking error contribution is zero. Based on the project specification the FWHM seeing contribution (i.e. actual seeing) is 1 arcsecond. For the Celestron-5 the aggregate FWHM is:

$$\mathrm{FWHM}_{(\mathrm{aggregate})} = \sqrt{1.08^2 + 1^2}$$
$$= 1.47 \text{ arcseconds}$$

and for the Meade-10 the aggregate FWHM is:

$$\mathrm{FWHM}_{(\mathrm{aggregate})} = \sqrt{0.54^2 + 1^2}$$
$$= 1.14 \text{ arcseconds}$$

These results imply that for any seeing value larger than 1.14 arcseconds for the 10-inch Meade and 1.47 arcseconds for the Celestron-5, the resolution will be seeing limited. Therefore the Meade-10 optics does not impose much limitation on the measurement of seeing down to approximately 1 arcsecond, while the limitation imposed by the Celestron-5 is marginal.

Detector   The spatial resolution of the detector is determined by the plate scale and the size of the smallest element on the detector plate. The smallest element on a CCD detector is the pixel and that for the photographic detector refers to the grain size of the film.

As discussed in section 2.3.1, the plate scale determines the relationship between the smallest element on the detector plate and the angular size of an area of the sky imaged by each element. The plate scale is a function of the telescope's focal length and in determining the

spatial resolution it also depends on the detector element size. Equation 2.4 has been used to calculate the angular resolution obtained by the photographic system with a grain size of 6 micron.

$$s = \frac{\pi}{180} \times 1250$$
$$= 21.82 \text{ mm.degree}^{-1}$$
$$= \frac{21.82 \times 10^3}{3600}$$
$$= 6.06 \ \mu\text{m.arcseconds}^{-1}$$

$$\text{resolution} = \frac{6}{6.06}$$
$$= 1.00 \text{ arcseconds.grain}^{-1}$$

This result demonstrates that the photographic method provides an improved resolution over the digital implementation (1.32 arcseconds for the ST-4 and 2.23 arcseconds for the ST-6B) due to the smaller detector elements (see Appendix C, section C.2.3:"Detector Resolution").

Traditionally Nyquist's application to stellar profile sampling has been used to determine the minimum required spatial resolution of a CCD camera for the measurement of seeing. This theorem has been applied in the next section in order to determine whether our CCD detectors will provide the spatial resolution required to measure seeing accurately down to 1 arcsecond.

Nyquist Theorem Applied to CCD Imaging

Nyquist's sampling theorem states that for a continuous-time (analogue) signal to be represented by a sampled signal (digital), it should be sampled at twice the highest frequency component present in the continuous-time signal (Ogata 1995). The Nyquist Theorem, as stated above, applies to one-dimensional audio and electrical signals. However, the image of a star on a CCD is a two-dimensional image, with axis x, y defining the plane of the CCD and amplitude given by the S/N of the stellar profile. Therefore ideally one would want to sample the profile such that its centre and shape can be reconstructed to a high accuracy. The following three illustrations have been used to demonstrate the optimal sampling of the stellar

profile based on the Nyquist resolution criterion. Each illustration represents an x-y plot of a star image with its intensity represented by the colour of each pixel.

Illustration A Figure 4.8 represents a star image where the size of the star image spans one pixel only. It is seen that if the star image is detected at the centre of a pixel, the star will be reproduced as a square and for a star image that is detected at the intersection of a group of pixels, the star is reproduced as a larger and dimmer square. Both situations represent an undersampled star image where the image does not accurately represent the PSF.
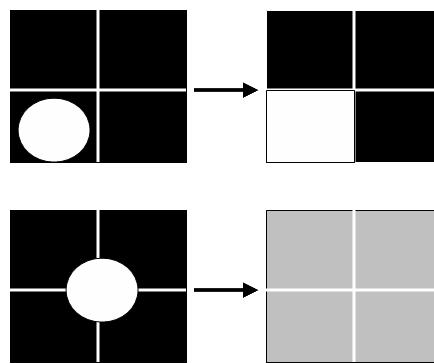
Figure 4.8: An Undersampled Star Image

Illustration B Figure 4.9 represents a star image sampled at the Nyquist frequency, (i.e. spans two pixels). It can be seen that a star image detected on the intersection of pixels will be reproduced as a square and a star image that that is detected on the centre of a pixel will be reproduced as a circular image. Therefore sampling at the Nyquist frequency only produces a better approximation to the PSF for star pixels which fall on the centre of a pixel.
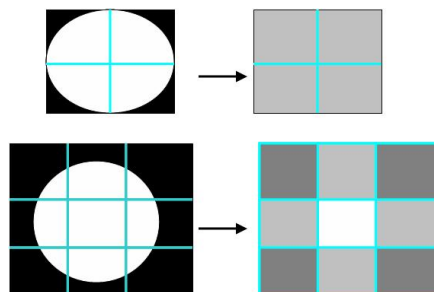
Figure 4.9: A Star Image Sampled at the Nyquist Sampling Rate

Illustration C Figure 4.10 represents a star image sampled at three times the sampling rate of Illustration A, (i.e. spans three pixels). It can be seen in both situations, where the star image is detected on the centre of one pixel or where it is detected on the intersection of pixels, it will be reproduced as a circular image, with the intensity values for each pixel more closely representing the PSF.
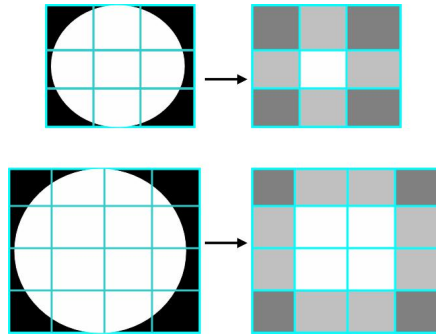
Figure 4.10: An Oversampled Star Image

These illustrations have demonstrated that an optimal sampling of the PSF of an astronomical source occurs when a star image is sampled over approximately three pixels.

Optimal Sampling according to Nyquist

Howell (2000) identifies the critical sampling as the sampling interval that is equal to the width of the stellar profile. Since the stellar profile can be approximated by a Gaussian distribution (see Figure 4.11), the width corresponds to the FWHM of the Gaussian distribution equal to 2.355 pixels.

Based on the Nyquist criterion Howell (2000) defines a sampling parameter, r, and considers the digital data undersampled for an r-value less than 1.5:

$$r = \frac{\text{FWHM}}{p} \tag{4.9}$$

where FWHM is the full-width half-maximum value of the PSF and p is the pixel size, both measured in the same units. Equation 4.9 can be used to determine whether the CCD cameras provide sufficient resolution based on the Nyquist criterion. The FWHM value is to be taken
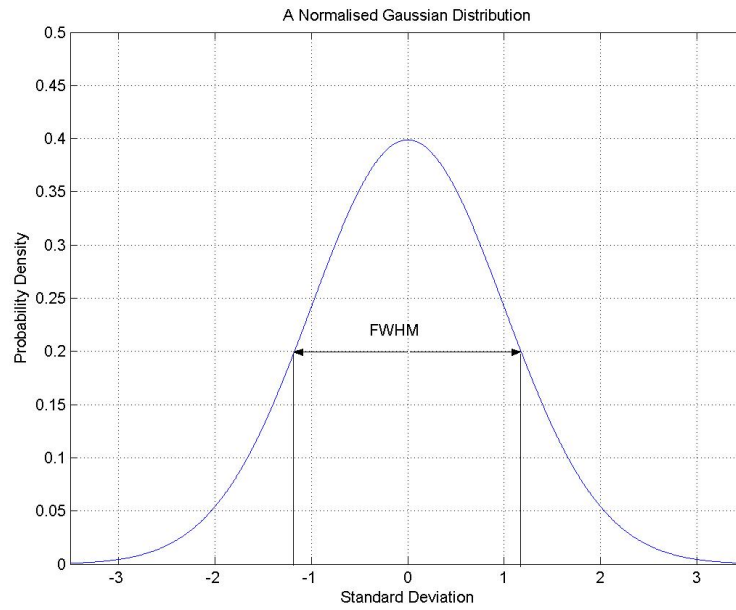
Figure 4.11: A Normalised Gaussian Distribution

as one arcsecond since we require to measure the seeing down to 1 arcsecond. Accordingly the value of p must correspond to the angular resolution of each pixel measured in arcseconds, hence we have:

$$r(\text{ST4}) = \frac{1}{1.32}$$
$$= 0.76$$
$$r(\text{ST6B}) = \frac{1}{2.23}$$
$$= 0.45$$

which suggests an undersampled stellar profile. We may conclude that based on the Nyquist criterion, the ST-4 and ST-6B cameras do not provide sufficient resolution to allow the measurement of seeing down to 1 arcsecond. However initial investigations, as explained in section 4.6, reveal otherwise.

4.4   Summary of the Critical Parameters

The previous sections have shown that the resolution of the available CCD cameras is inadequate, based on the Nyquist criterion given by Howell (2000). However it will be shown that this resolution criterion does not set the absolute limitation as poorer resolution can be tolerated if the signal to noise ratio is increased.

A summary of the calculations, which have been used to assess the capabilities of the available equipment for the measurement of seeing down to 1 arcsecond, has been provided in Table 4.3. Appendix C contains the calculations, while reference has been made to them throughout this chapter. Calculations used to determine the suitability of the ST-4 have been performed using data from Table 4.1 while ST-6B calculations made use of data in Table 4.2 and followed the format of the ST-4 calculations. Their working has hence not been included.

Table 4.3: ST-4 and ST-6B Seeing Measurement Suitability Calculation Results

Target Star	Magnitude 12		Magnitude 14	
CCD Camera	ST-4	ST-6B	ST-4	ST-6B
CCD FoV [arcsec]	216.5	536.9	216.5	536.9
Star Count per CCD FoV	0.078	0.6308	0.3722	3.02
Residency Time [ms]	75.6	127	75.6	127
Saturation Time [s]	4.8	17.9	30.1	112.9
Signal Count per Pixel [ADU]	8.45	422	1.3	66.9
Noise Count per Pixel [ADU]	1.00	3.44	1.00	3.44
Signal to Noise Ratio	12.9	540.8	2.02	85.7
Resolution [arcsec.pixel^{-1}]	1.32	2.23	1.32	2.23

4.5   Digital or Photographic?

It has been shown that film, compared to the CCDs that have been made available, is superior in both resolution and field of view. However, due to the analog nature of the image recorded on the film, quantitative seeing measurements are only possible once the image has been digitalised, which means that significant time needs to be committed to film changing,

processing and digitisation of the image. Another drawback of film is its extremely poor quantum efficiency as the film records only a few percent of the incident photons which corresponds to an extremely poor signal to noise ratio. Having taken into consideration the impracticalities associated with photographic film, the decision was made to proceed with a digital implementation, making use of the ST-4 CCD camera as a test bed.

4.6 Interrelation of Resolution and Signal to Noise – "A Way Forward?"

Traditionally the Nyquist theorem is referred to as the criterion which must be satisfied in order to be able to measure the seeing accurately, a principle which has been re-emphasised by Howell (2000). An immediate counter example would be the fact that if no noise is present in the imaging system, the measurement of the seeing can be made accurately, even with poor detector resolution (i.e. below the Nyquist resolution). This may be analysed as follows.

Assume that our system is defined by the following equation:

$$y = f(x, a_1, a_2, a_3, a_4, a_5)$$

where y is a function of x and is defined by the parameters a_1 through to a_5. The solving for the five parameters would require five equations to be solved simultaneously. Ignoring round-off errors caused by the computer processing, the solving of these equations will produce the exact values for the five parameters. Assuming that noise has now been added to the system, the function will have the following form:

$$y = f(x, a_1, a_2, a_3, a_4, a_5) + e$$

where e represents the error/noise term. The accuracy obtained in calculating the five parameters will now depend on the magnitude of the error term. What is now of interest is how large the noise/error component can grow, before it begins to affect the accuracy of the calculated parameters, beyond the accepted tolerance (i.e. project specification requires seeing measured within 0.5 arcsecond accuracy). Applying this principle to the requirements of the project, we arrive at the following question:

What is the minimum S/N at the resolution of our detectors that will allow us to

determine seeing within 0.5 arcseconds accuracy and down to 1 arcsecond

seeing?

Figure 4.12 is an intuitive sketch of a qualitative analysis in response to the raised question. The hash marked region has no defined boundaries as yet, however it separates the two regions A and C. Region C represents the area where the seeing can be resolved, while in region A the seeing cannot be resolved to the required accuracy. Figure 4.12 suggests that with a poor S/N and poor resolution we cannot resolve the seeing, however with a poor resolution and good S/N we will be able to resolve the seeing to a defined accuracy. Hence it is the magnitude of S/N that needs to be quantified.
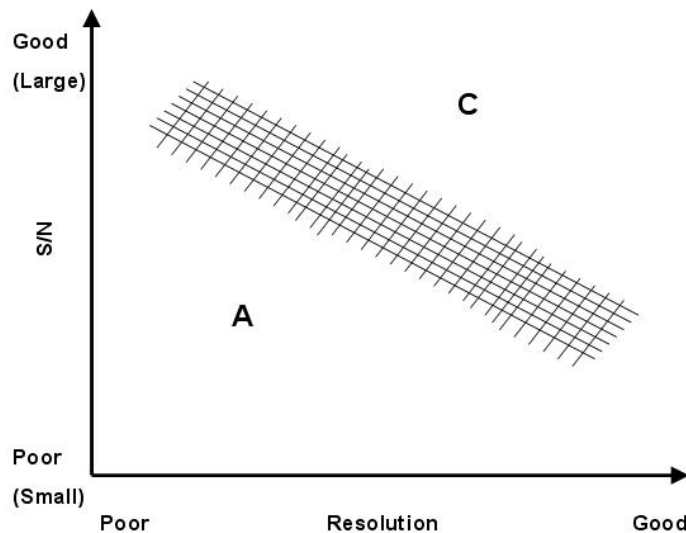
Figure 4.12: A qualitative sketch of the relationship between resolution and signal to noise ratio with respect to seeing measurements, C represents the region capable of resolving the seeing and A represents the region where seeing cannot be resolved.

Figure 4.13 is another qualitative sketch adding to the information provided by Figure 4.12. The lines marked A, B and C represent regions which have equal standard error (SE) in their measurement of the seeing where SE(A)>SE(B)>SE(C). This diagram clearly represents that for a fixed resolution marked R (i.e. camera resolution), as the S/N improves, the SE of the seeing decreases.

The next chapter will focus on quantifying Figures 4.12 and 4.13 for a stellar profile, in order to obtain an answer to the previously raised question:
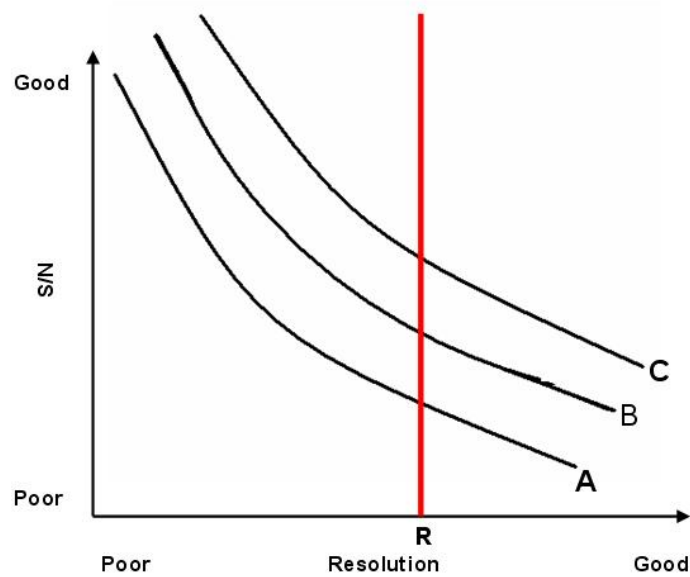
Figure 4.13: A qualitative sketch of the relationship between resolution and signal to noise ratio with respect to seeing measurements, demonstrating that for a fixed resolution, with an improvement in S/N the SE of the seeing measurement decreases (Note that: SE(A)>SE(B)>SE(C)).

What is the minimum S/N at the resolution of our detectors that will allow us to determine seeing within 0.5 arcseconds accuracy and down to 1 arcsecond seeing?

4.7   Chapter Summary

Both digital and photographic imaging system have been evaluated and the results demonstrate that both methods fail to measure the seeing to the required specifications. For the evaluation, three critical design factors were identified, namely field of view, signal to noise ratio and resolution. The field of view, in combination with the stellar density function was found to determine the probability of capturing a star on the CCD plane during the exposure time. The limitations imposed by the small CCD size of the ST-4 and ST-6B CCD cameras could then be overcome by pointing closer to the galactic plane. The signal to noise ratio required the calculation of both the signal count and the noise count. This calculation was based on the ratio of the zero to peak amplitude of the Gaussian stellar profile to the standard deviation of the noise. Residency time and saturation time were considered critical, in particular for a stellar trail imaging system. Diffraction limited resolution due to the optics

of the available telescopes was shown to not impose much limitation on the measurement of seeing down to 1 arcsecond. Overall the digital camera's shortcoming over photographic film was due to its poor Nyquist resolution.

Whilst Nyquist Theorem requires the FWHM of the PSF to cover 2.355 pixels, initial investigations show that this criterion does not always set the absolute limit. This is because it was shown that poorer resolution can be tolerated if the signal to noise ratio is increased. Hence while the photographic implementation provided improved resolution and field of view, its extremely poor S/N and associated impracticalities (e.g. film changing, processing and scanning) were considered a larger detriment and a digital implementation was decided upon.

The next chapter optimises seeing measurements made from stellar profiles. Both error estimation theory and fitting to simulated stellar profiles have been used in this study.

Chapter 5

Optimisation of Stellar Profile Seeing Measurements

5.1   Chapter Overview and Rationale

The initial investigations of Chapter 4 have suggested that the Nyquist theorem does not set the ultimate limit on the accurate measurement of seeing. Figure 4.13 demonstrated that the accuracy of fitting to a Gaussian stellar profile depends on the signal to noise (S/N) and the resolution of profile sampling.

Figure 5.1 represents the dependance of standard error (SE) of the fitting on resolution and S/N. The aim of this chapter is to determine how much below the Nyquist sampling resolution we can sample the stellar profile, and the S/N that we require, in order to make an acceptable fit to the signal (i.e. within 0.5 arcseconds as defined by the project specifications). In obtaining a solution both fitting error analysis and simulations were used.

To quickly gain some insight into this question, the IRIS astronomical image processing software (Buil 2006) was used on simulated Gaussian stellar profiles, generated with MATLAB. This demonstrated that the seeing can be measured accurately with resolution below that of the Nyquist resolution for a noise free system. However it became apparent that SE also depended on the fitting window size. Unfortunately this was difficult to control with

IRIS. Both error estimation theory and fitting to simulations were used to study the

dependencies shown in Figure 5.1. The methods were based on the Levenberg-Marquardt

(LM) technique of non-linear least squares fitting . This created an environment where all

influencing factors on the SE of the seeing could be controlled, and allowed for the

determination of the S/N and resolution required to measure the seeing within 0.5 arcseconds

and down to 1 arcsecond.
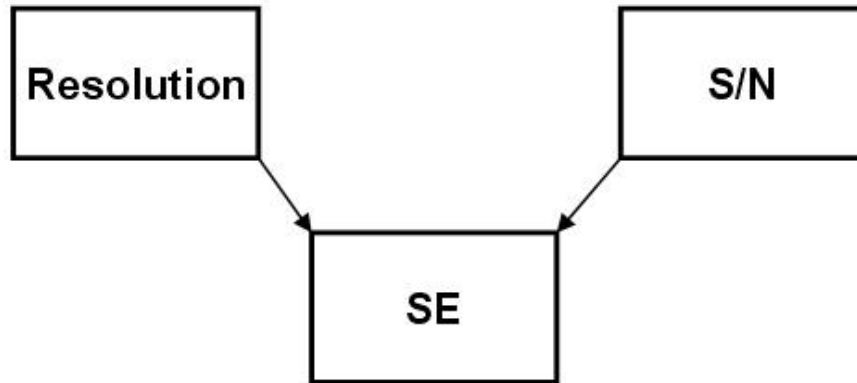
Figure 5.1: Initial Investigations show that the S/N and Resolution affect the SE of the seeing
obtained.

5.2   Preliminary Analysis of Fitting to Stellar Profiles

Initial investigations involved the simulation of MATLAB generated Gaussian stellar profiles

using IRIS.

5.2.1   Simulation of a Gaussian Stellar Profile

As discussed in section 2.4.2 the stellar profile may be approximated by a Gaussian PSF. A

one dimensional Gaussian function is the probability function of the normal distribution. The

one dimensional Gaussian distribution has the form (Jenkins 2003):

$$\mathrm{f}(x) = \frac{1}{\sigma\sqrt{2\pi}}\exp\{-\frac{x-a^2}{2\sigma^2}\} \tag{5.1}$$

where σ is the standard deviation, σ^2 is the variance and a is the mean. The full width at half

maximum is given by (Jenkins 2003):

$$\text{FWHM} = 2.355\sigma \tag{5.2}$$

In two dimensions, the circular Gaussian function may be used to approximate an averaged stellar profile and is given by (Jenkins 2003):

$$\text{f}(xx, yy) = \text{a}_0 \exp\{-\frac{(xx - a)^2 + (yy - b)^2}{2\sigma^2}\} \tag{5.3}$$

$$\text{a}_0 = \frac{\text{a}}{2\pi\sigma^2} \tag{5.4}$$

where xx and yy define the plane of the CCD, a and b are the peak locations in the xx and yy directions respectively, a is the total signal count [ADU] (i.e. area under the curve), f is the counts per unit area and a_0 is the peak amplitude of the stellar profile.

The MATLAB function `circgauss` generates a stellar profile based on the Gaussian distribution (see Appendix D, section D.2). It is defined as:

```
[n,a0] = circgauss(x,y,a,b,amp,sigma,noise)
```

where:

- `x` and `y` are equal length vectors of pixel positions;

- `a` and `b` define the stellar centroid on the CCD plane for `x` and `y` respectively;

- `amp` is the total signal count [ADU] (a in Equation 5.4);

- `noise` is the noise count [ADU] (i.e standard deviation of the gaussian noise);

- `sigma` is the standard deviation of the stellar profile, calculated using Equation 5.2. `sigma` is obtained by:

$$\text{sigma} = \frac{\text{FWHM [pixels]}}{2.355} = \frac{\text{seeing FWHM } [\mu m]}{2.355 \times \text{CCD resolution } [\mu m]} \tag{5.5}$$

- `n` is a matrix containing the stellar profile;

- `a0` is the peak amplitude of the stellar profile, calculated using Equation 5.4.

Using the relevant data from Table 4.3 the `circgauss` function was used to generate the stellar profile of a magnitude 12 target star using the ST-4 and ST-6B CCD cameras. The set of inputs to the `circgauss` function using the ST-4 CCD camera are:

```
[n] = circgauss(1:100,1:100,50,50,845,(1/1.32)/2.355,100).
```

The output, which is the stellar profile of a magnitude 12 star, is given in Figure 5.2. The set of inputs to the `circgauss` function using the ST-6B camera are:

```
[n] = circgauss(1:100,1:100,50,50,4220,(1/2.23)/2.355,34.4).
```

The output is given in Figure 5.3. When Figures 5.2 and 5.3 are compared, what is immediately apparent is the improved signal to noise ratio obtained using the ST-6B. However the ST-6B as previously discussed provides less spatial resolution compared to the ST-4.
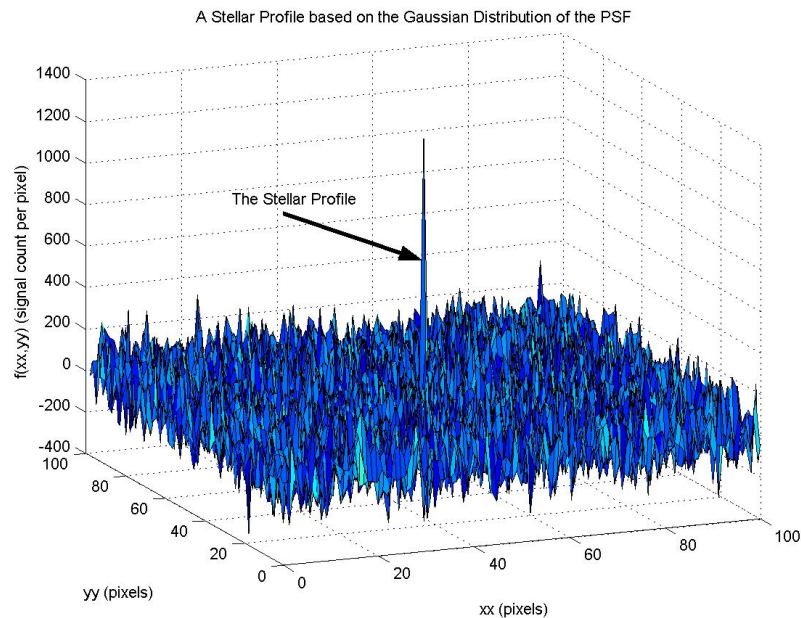
Figure 5.2: The Stellar Profile of a Magnitude 12 Star on the ST-4 CCD
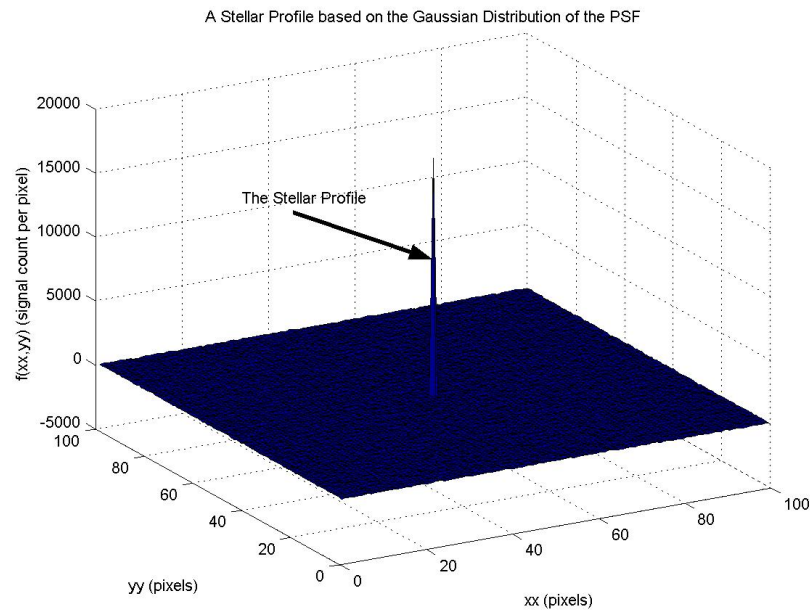
Figure 5.3: The Stellar Profile of a Magnitude 12 Star on the ST-6B CCD

5.2.2 Fitting Simulated Stellar Profiles with IRIS

The IRIS software package was chosen as a fast and convenient method for fitting to the simulated noisy Gaussian profiles of the previous section, so as to identify the impact of S/N and resolution on the SE of the seeing measurements. IRIS, unlike many other astronomical packages, was easy to learn and use. IRIS is software used for the image processing of digital astronomical images, written by Christian Buil (Buil 2006). The software has been particularly optimised to explore images captured on CCD cameras and provides a function for fitting to stellar profiles.

IRIS loads images in FITS format. The FITS format stands for flexible image transport system and was developed by astronomers to allow for the easy transfer of images between computers. Hence all astronomical image processing software has the capability to read and write FITS format files. The Gaussian stellar profiles shown in section 5.2.1 have been generated using MATLAB, which did not have an in-built FITS write function. A FITS conversion program was thus provided by project co-supervisor Dr. Rhodes Hart.

With the output of the MATLAB `circgauss` function converted to FITS format, IRIS was then used to calculate the FWHM of the stellar profile. IRIS returns the FWHM of the star

along both X and Y axis. For our purposes the stellar FWHM is calculated as the average of the X and Y FWHM values. To determine the SE for a particular stellar profile, a large number of simulations were run (typically hundreds), each with different sets of random noise. The standard deviation of the fitted FWHM's from the input FWHM was then calculated for the simulations and taken as the SE, hence determining the accuracy of the fit made by IRIS.

5.2.3 Results of Simulations

The procedure was first used to check the assertion of Chapter 4 that resolution below the Nyquist can be used in the absence of noise. IRIS was able to successfully demonstrate that if no noise is present in the imaging system, the measurement of seeing can be made accurately with a resolution below that of the Nyquist resolution. Figure 5.4 represents the stellar profile of a magnitude 12 star on the ST-4 CCD, with a FWHM of 0.75 pixels, and system noise which has been set to zero. The set of inputs to the `circgauss` function are: `[n] = circgauss(1:100,1:100,50,50,845,(1/1.32)/2.355,0)`. Figure 5.5 is the IRIS screen, which shows that IRIS has perfectly fitted to an undersampled stellar profile, thus accurately calculating the FWHM equal to 0.75 pixels. IRIS has hence confirmed our earlier argument that if no noise is present in the imaging system, the measurement of the seeing can be made accurately, even with poor detector resolution.

To explain why this is possible, an undersampled one-dimensional Gaussian, with a signal of 10, standard deviation of 0.75 and zero system noise was considered (see Figure 5.6). The FWHM of the Gaussian distribution covers only a fraction of one pixel, hence the sampling of this Gaussian occurs further out in the tails of the distribution (i.e neighbouring pixels). With no noise present in the system, sampling in the tails will be sufficient to accurately fit to the stellar profile. Using Equation 5.1 the function representing this distribution is:

$$y = 10 \exp\{-\frac{x^2}{2\sigma^2}\}$$

As the following calculations show, the point (2,0.29) in the distribution tail may be used to accurately calculate the standard deviation of the distribution in order to fit to the stellar profile.
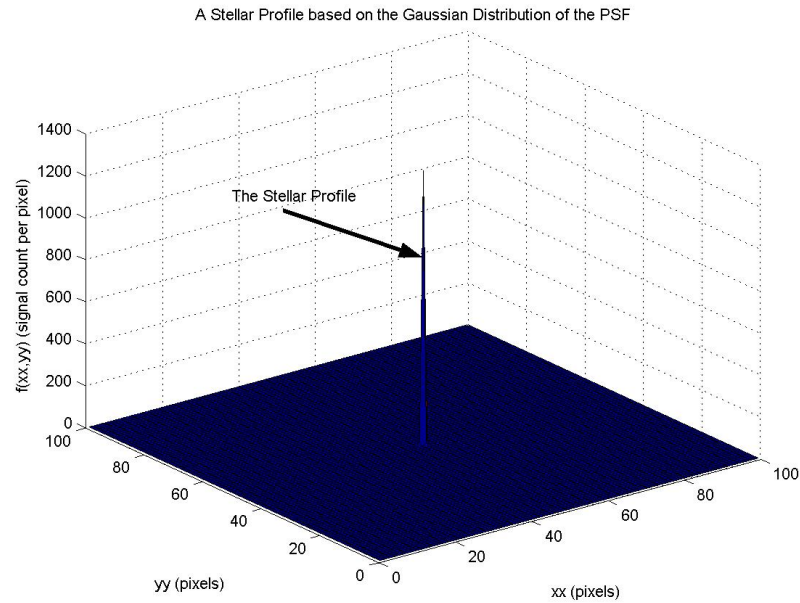
Figure 5.4: The Stellar Profile of an Undersampled Magnitude 12 Star on the ST-4 CCD and Zero System Noise.

$$0.29 = 10 \exp\{-\frac{2^2}{2\sigma^2}\}$$

$$\ln \frac{0.29}{10} = \frac{-4}{2\sigma^2}$$

$$\sigma = \sqrt{\frac{-4}{2 \times \ln \frac{0.29}{10}}}$$

$$= 0.75 \text{ pixels}$$

The next step was to investigate the impact when noise is added to this undersampled example. The S/N had been previously defined as the zero to peak of the Gaussian distribution (a_0) divided by the standard deviation of the Gaussian noise distribution. However with poor resolution the sampling of the Gaussian will be further out in the tails, where the effective signal is lower and hence the S/N is poorer:

$$S/N_{\text{effective}} = \frac{a_0}{\sigma_{noise}} \exp\{-\frac{x^2}{2\sigma_{Gaussian}^2}\} \tag{5.6}$$

For a lower effective S/N and the addition of system noise, the fitted gaussian will not be
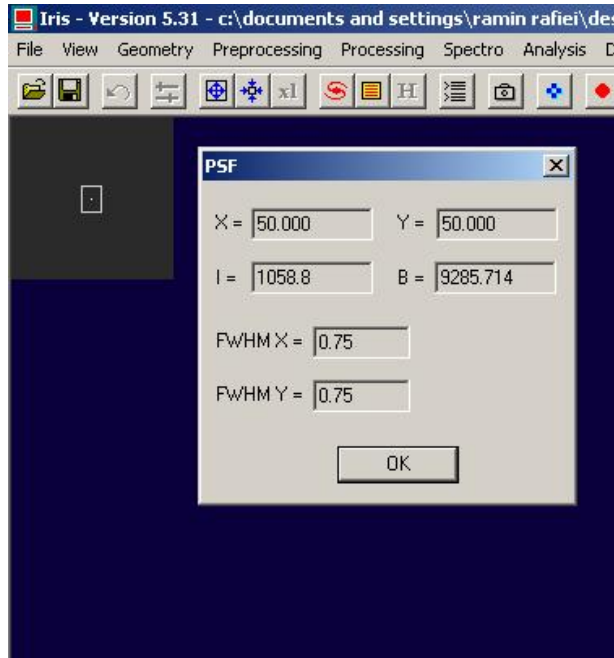
Figure 5.5: IRIS has fitted perfectly to an undersampled stellar profile with zero system noise.

representative of the true profile. The value of the distribution, as shown in Figure 5.7, at the point $x = 2$ no longer corresponds to its amplitude at that point, but it measures the amplitude of the noise distribution. The following calculations demonstrate that the profile of the fitted Gaussian has a standard deviation different to the value of 0.75 pixels and hence will not be representative of the true profile.

$$1.2 = 10 \exp\{-\frac{2^2}{2\sigma^2}\}$$
$$\ln \frac{1.2}{10} = \frac{-4}{2\sigma^2}$$
$$\sigma = \sqrt{\frac{-4}{2 \times \ln \frac{1.2}{10}}}$$
$$= 0.97 \text{ pixels}$$

When the procedure was applied to noisy simulations, it was discovered that the SE of the measurement depends on the size of the fitting window as well as the S/N and resolution. Indeed, from many simulations the accuracy of the fitting was found to be critically dependent on the size of the window selected around the stellar image. Figure 5.8 demonstrates the current understanding of the factors which affect the SE of the fitting.
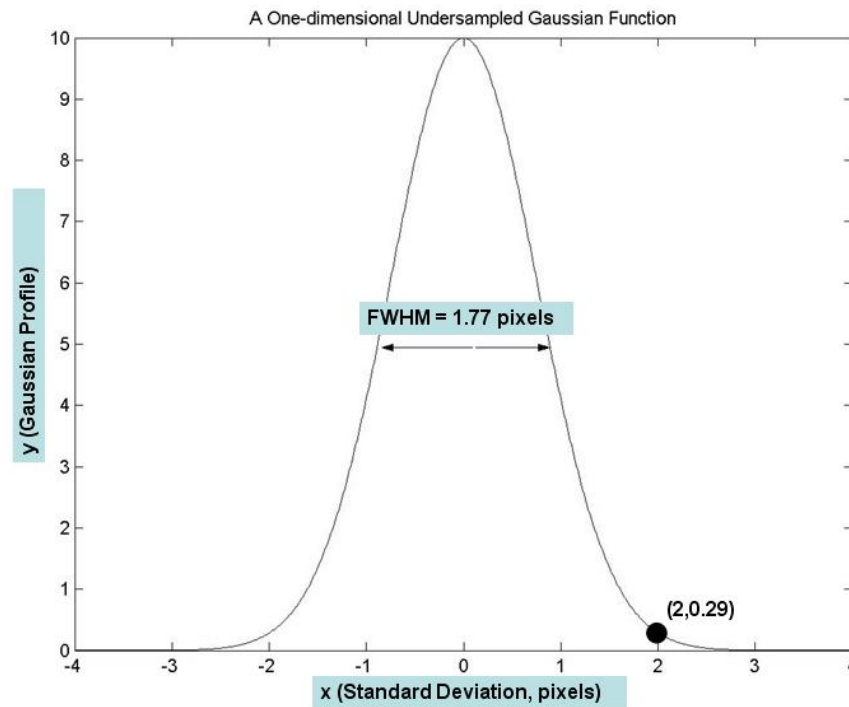
Figure 5.6: The sampling of an undersampled gaussian distribution, which has a FWHM less than one pixel wide, occurs in the neighbouring pixels.

While IRIS demonstrated that the SE is dependent also on the number of pixels in the fitting window, no optimum window size had been recommended by Buil (2006), and selecting a consistent window with IRIS was nearly impossible.

A decision was therefore made to build a simulation and fitting environment where the effects of S/N and resolution could be identified, with control of the fitting window.

5.3 Error Estimation Theory for Non-Linear Least Squares Fitting

In sections 5.3–5.5 we use error estimates for the Levenberg-Marquardt method of non-linear least squares fitting to investigate how much below the Nyquist theorem we could sample the signal and the S/N that we require, in order to make an acceptable fit to the stellar profile. The preliminary study with IRIS showed that beside the S/N and resolution, the size of the fitting window affects the SE of the fitting, but limitations imposed by IRIS meant the error
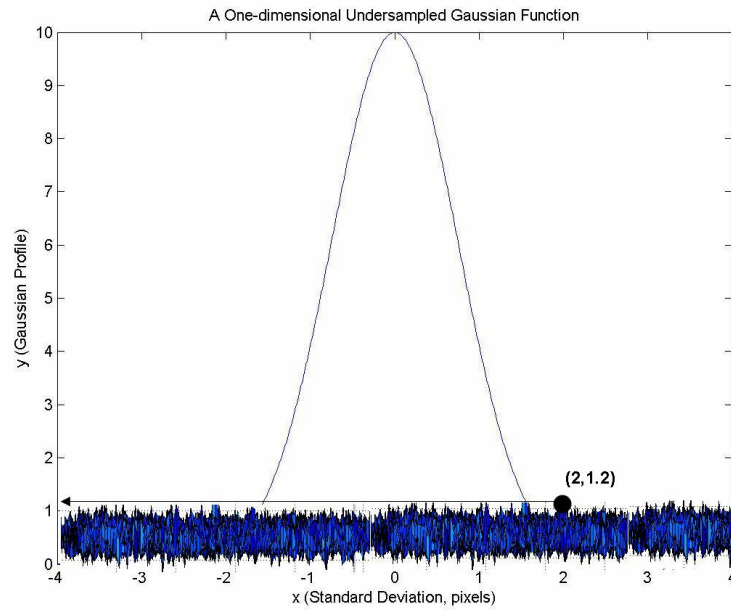
Figure 5.7: An undersampled gaussian distribution with system noise does not allow for an accurate fitting.

dependence on these parameters could not be explored adequately. An understanding of fitting theory was therefore required.

A commonly accepted approach to fit to a function that is non-linear in the fitting parameters is the Levenberg-Marquardt fitting algorithm (Borse 1997). A decision was therefore made to use this approach. In applying this method three assumptions were made:

- the stellar image is circular;

- point sampling is performed, although in practice CCD astronomy involves sampling over the pixel area;

- sampling time for the stellar profile is long enough to ensure that noise arises only from the CCD noise.

This method involves the minimisation of χ^2, which is defined as the sum of squared differences between the measured and predicted values, normalised by the standard deviation
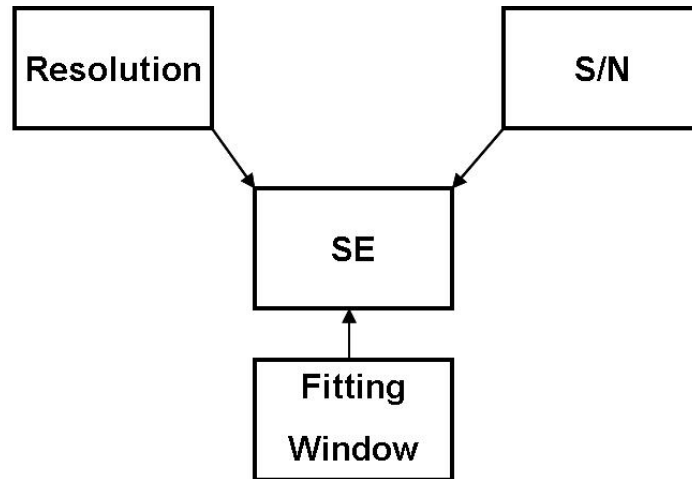
Figure 5.8: IRIS has demonstrated that the SE of the seeing obtained depends also on the size of the fitting window.

of noise (σ_i). That is:

$$\chi^2(a) = \sum_{i=1}^{N} [\frac{y_i - y(\vec{x}_i; \vec{a})}{\sigma_i}]^2 \tag{5.7}$$

where y defines the model to be fitted and is a function of the pixel positions, vector $\vec{x}_i$, and parameters given by vector $\vec{a}$. y_i is the measured data and N is the number of pixels in the sampling window (Press & Vetterling 1992). Uniform spatial and temporal Gaussian noise over the CCD plane has been assumed with the standard deviation equal to σ. χ^2 is therefore given by:

$$\chi^2(a) = \frac{1}{\sigma^2} \sum_{i=1}^{N} [y_i - y(\vec{x}_i; \vec{a})]^2 \tag{5.8}$$

The LM method shows that the covariance matrix of the standard errors (SE) in the fitted parameters, $\vec{a}$, is given by (Press & Vetterling 1992):

$$[C] = [\alpha]^{-1} \tag{5.9}$$

where the Hessian Matrix ($[\alpha]$) elements, for a constant measurement error, at indices kl are

given by (Press & Vetterling 1992):

$$\alpha_{kl} = \frac{1}{\sigma^2} \sum_{i=1}^{N} [\frac{\partial y(\vec{x}_i; \vec{a})}{\partial a_k} \frac{\partial y(\vec{x}_i; \vec{a})}{\partial a_l}] \tag{5.10}$$

For a set of five parameters the covariance matrix is given by:

$$[C] = \begin{pmatrix} \mathrm{SE}_{11}^2 & \mathrm{SE}_{12}^2 & \mathrm{SE}_{13}^2 & \mathrm{SE}_{14}^2 & \mathrm{SE}_{15}^2 \\ \mathrm{SE}_{21}^2 & \mathrm{SE}_{22}^2 & \mathrm{SE}_{23}^2 & \mathrm{SE}_{24}^2 & \mathrm{SE}_{25}^2 \\ \mathrm{SE}_{31}^2 & \mathrm{SE}_{32}^2 & \mathrm{SE}_{33}^2 & \mathrm{SE}_{34}^2 & \mathrm{SE}_{35}^2 \\ \mathrm{SE}_{41}^2 & \mathrm{SE}_{42}^2 & \mathrm{SE}_{43}^2 & \mathrm{SE}_{44}^2 & \mathrm{SE}_{45}^2 \\ \mathrm{SE}_{51}^2 & \mathrm{SE}_{52}^2 & \mathrm{SE}_{53}^2 & \mathrm{SE}_{54}^2 & \mathrm{SE}_{55}^2 \end{pmatrix} \tag{5.11}$$

The diagonal terms of the covariance matrix are the squares of the estimated standard errors (Press & Vetterling 1992), given by:

$$\mathrm{SE}^2 = \begin{pmatrix} \mathrm{SE}_{11}^2 \\ \mathrm{SE}_{22}^2 \\ \mathrm{SE}_{33}^2 \\ \mathrm{SE}_{44}^2 \\ \mathrm{SE}_{55}^2 \end{pmatrix} \tag{5.12}$$

This interpretation of the standard errors holds only if the fitted parameters are uncorrelated. The correlation, ρ, is given by (Jenkins 2003):

$$\rho_{kl} = \frac{[\alpha^{-1}]_{kl}}{\sqrt{[\alpha^{-1}]_{kk}[\alpha^{-1}]_{ll}}} \tag{5.13}$$

where $0 < \rho < 1$ and $\rho = 0$ signifies no correlation. Therefore the correlation matrix, $[\rho]$ can

be represented as:

$$[\rho] = \begin{pmatrix} 1 & \dfrac{\text{SE}_{12}^2}{\text{SE}_{11}\text{SE}_{22}} & \dfrac{\text{SE}_{13}^2}{\text{SE}_{11}\text{SE}_{33}} & \dfrac{\text{SE}_{14}^2}{\text{SE}_{11}\text{SE}_{44}} & \dfrac{\text{SE}_{15}^2}{\text{SE}_{11}\text{SE}_{55}} \\ \dfrac{\text{SE}_{21}^2}{\text{SE}_{22}\text{SE}_{11}} & 1 & \dfrac{\text{SE}_{23}^2}{\text{SE}_{22}\text{SE}_{33}} & \dfrac{\text{SE}_{24}^2}{\text{SE}_{22}\text{SE}_{44}} & \dfrac{\text{SE}_{25}^2}{\text{SE}_{22}\text{SE}_{55}} \\ \dfrac{\text{SE}_{31}^2}{\text{SE}_{33}\text{SE}_{11}} & \dfrac{\text{SE}_{32}^2}{\text{SE}_{33}\text{SE}_{22}} & 1 & \dfrac{\text{SE}_{34}^2}{\text{SE}_{33}\text{SE}_{44}} & \dfrac{\text{SE}_{35}^2}{\text{SE}_{33}\text{SE}_{55}} \\ \dfrac{\text{SE}_{41}^2}{\text{SE}_{44}\text{SE}_{11}} & \dfrac{\text{SE}_{42}^2}{\text{SE}_{44}\text{SE}_{22}} & \dfrac{\text{SE}_{43}^2}{\text{SE}_{44}\text{SE}_{33}} & 1 & \dfrac{\text{SE}_{45}^2}{\text{SE}_{44}\text{SE}_{55}} \\ \dfrac{\text{SE}_{51}^2}{\text{SE}_{55}\text{SE}_{11}} & \dfrac{\text{SE}_{52}^2}{\text{SE}_{55}\text{SE}_{22}} & \dfrac{\text{SE}_{53}^2}{\text{SE}_{55}\text{SE}_{33}} & \dfrac{\text{SE}_{54}^2}{\text{SE}_{55}\text{SE}_{44}} & 1 \end{pmatrix} \tag{5.14}$$

5.4 Error Estimation for Fitting with Five Parameters

In this section, we apply the error estimation theory of the previous section to the case where the fit to the stellar profile is made for five parameters, namely:

- signal count;

- standard deviation of the Gaussian profile;

- star centroid location in the x-direction;

- star centroid location in the y-direction;

- CCD pedestal voltage.

5.4.1 Application of Theory to Fitting with Five Parameters

The general form of a two-dimensional Gaussian profile was presented in section 5.2.1. Equation 5.15 represents the two-dimensional Gaussian profile where the five parameters defined by $\vec{a}$ are represented as a_1 through to a_5.

$$y = \frac{a_1}{2\pi a_2^2}\exp\{-\frac{(x_1 - a_3)^2 + (x_2 - a_4)^2}{2a_2^2}\} + a_5 + e \tag{5.15}$$

where:

- a_1: signal count- total counts if all light from a star was collected by one pixel (i.e. area under the Gaussian curve)

- a_2: standard deviation of the gaussian;

- a_3 and a_4: star centroid location;

- a_5: CCD pedestal voltage. For an unexposed pixel the value for the zero collected photoelectrons will translate, upon readout and A/D conversion, into a mean value with a small distribution about zero. A pedestal voltage is applied by the hardware in order to prevent the occurrence of a negative voltage;

- e: combination of all error terms;

- x_1 and x_2: define the plane of the CCD detector.

For the five parameter fitting, Equation 5.10 is represented as:

$$\alpha_{kl} = \frac{1}{\sigma^2} \sum_{i=1}^{N} [\frac{\partial y(x_{1_i}; x_{2_i}, a_1, a_2, a_3, a_4, a_5)}{\partial a_k} \frac{\partial y(x_{1_i}; x_{2_i}, a_1, a_2, a_3, a_4, a_5)}{\partial a_l}] \tag{5.16}$$

The partial derivatives for each parameter were calculated as:

$$\frac{\partial y}{\partial a_1} = \frac{1}{2\pi a_2^2} \exp[-\frac{(x_1 - a_3)^2 + (x_2 - a_4)^2}{2a_2^2}] \tag{5.17}$$

$$\frac{\partial y}{\partial a_2} = \frac{a_1}{2\pi a_2^2} \exp[-\frac{(x_1 - a_3)^2 + (x_2 - a_4)^2}{2a_2^2}][\frac{-2}{a_2} + \frac{(x_1 - a_3)^2 + (x_2 - a_4)^2}{a_2^3}] \tag{5.18}$$

$$\frac{\partial y}{\partial a_3} = \frac{a_1}{2\pi a_2^2} \exp[-\frac{(x_1 - a_3)^2 + (x_2 - a_4)^2}{2a_2^2}][\frac{x_1 - a_3}{a_2^2}] \tag{5.19}$$

$$\frac{\partial y}{\partial a_4} = \frac{a_1}{2\pi a_2^2} \exp[-\frac{(x_1 - a_3)^2 + (x_2 - a_4)^2}{2a_2^2}][\frac{x_2 - a_4}{a_2^2}] \tag{5.20}$$

$$\frac{\partial y}{\partial a_5} = 1 \qquad (5.21)$$

Using these partial derivatives the Hessian Matrix may be defined as:

$$[\alpha] = \frac{1}{\sigma^2} \begin{pmatrix} \sum_{i=1}^{N} \frac{\partial y}{\partial a_1} \frac{\partial y}{\partial a_1} & \sum_{i=1}^{N} \frac{\partial y}{\partial a_1} \frac{\partial y}{\partial a_2} & \sum_{i=1}^{N} \frac{\partial y}{\partial a_1} \frac{\partial y}{\partial a_3} & \sum_{i=1}^{N} \frac{\partial y}{\partial a_1} \frac{\partial y}{\partial a_4} & \sum_{i=1}^{N} \frac{\partial y}{\partial a_1} \frac{\partial y}{\partial a_5} \\ \sum_{i=1}^{N} \frac{\partial y}{\partial a_2} \frac{\partial y}{\partial a_1} & \sum_{i=1}^{N} \frac{\partial y}{\partial a_2} \frac{\partial y}{\partial a_2} & \sum_{i=1}^{N} \frac{\partial y}{\partial a_2} \frac{\partial y}{\partial a_3} & \sum_{i=1}^{N} \frac{\partial y}{\partial a_2} \frac{\partial y}{\partial a_4} & \sum_{i=1}^{N} \frac{\partial y}{\partial a_2} \frac{\partial y}{\partial a_5} \\ \sum_{i=1}^{N} \frac{\partial y}{\partial a_3} \frac{\partial y}{\partial a_1} & \sum_{i=1}^{N} \frac{\partial y}{\partial a_3} \frac{\partial y}{\partial a_2} & \sum_{i=1}^{N} \frac{\partial y}{\partial a_3} \frac{\partial y}{\partial a_3} & \sum_{i=1}^{N} \frac{\partial y}{\partial a_3} \frac{\partial y}{\partial a_4} & \sum_{i=1}^{N} \frac{\partial y}{\partial a_3} \frac{\partial y}{\partial a_5} \\ \sum_{i=1}^{N} \frac{\partial y}{\partial a_4} \frac{\partial y}{\partial a_1} & \sum_{i=1}^{N} \frac{\partial y}{\partial a_4} \frac{\partial y}{\partial a_2} & \sum_{i=1}^{N} \frac{\partial y}{\partial a_4} \frac{\partial y}{\partial a_3} & \sum_{i=1}^{N} \frac{\partial y}{\partial a_4} \frac{\partial y}{\partial a_4} & \sum_{i=1}^{N} \frac{\partial y}{\partial a_4} \frac{\partial y}{\partial a_5} \\ \sum_{i=1}^{N} \frac{\partial y}{\partial a_5} \frac{\partial y}{\partial a_1} & \sum_{i=1}^{N} \frac{\partial y}{\partial a_5} \frac{\partial y}{\partial a_2} & \sum_{i=1}^{N} \frac{\partial y}{\partial a_5} \frac{\partial y}{\partial a_3} & \sum_{i=1}^{N} \frac{\partial y}{\partial a_5} \frac{\partial y}{\partial a_4} & \sum_{i=1}^{N} \frac{\partial y}{\partial a_5} \frac{\partial y}{\partial a_5} \end{pmatrix}$$
$$(5.22)$$

The MATLAB function `cgfiterr` calculates the standard error of the five fitting parameters based on the LM theory of error estimation (see Appendix D, section D.3). `cgfiterr` is defined as:

```
[sde,cor,cov] = cgfiterr(amp,sig,const,pixfact)
```

where:

- `amp` is the signal count (i.e. area under the Gaussian curve and equivalent to a_1 in Equation 5.15);

- `sig` is the standard deviation of the Gaussian profile (a_2 in Equation 5.15);

- `const` is the pedestal voltage (a_5 in Equation 5.15);

- `pixfact` is the number of standard deviations across the fitting window;

- `sde` is the standard error of the five fitting parameters calculated using Equation 5.12;

- `cor` is the maximum correlation between the fitted parameters, where the correlation matrix is calculated using Equation 5.14;

- `cov` is the covariance matrix.

The `cgfiterr` function calculates the Hessian Matrix as given by Equation 5.10 using the partial derivatives defined by Equations 5.17 through to 5.21. The Hessian Matrix is then used to calculate the covariance matrix which was defined as its inverse (see Equation 5.9). The standard errors in the measurement of the fitting parameters are the square-root of the diagonal terms of the covariance matrix, given by Equation 5.12. The `cgfiterr` function also returns the maximum correlation between the fitted parameters as the above interpretation of the covariance matrix holds only if the fitted parameters are uncorrelated (see Equation 5.14).

The `cgfiterr` function also calculates the 'condition number' of the Hessian Matrix using Singular Value Decomposition (SVD). The SVD of matrix (A) returns three matrices named U, S and V for which (Press & Vetterling 1992):

$$A = USV^{T} \tag{5.23}$$

where U and V are orthogonal $n \times n$ matrices, and S is an $n \times n$ diagonal matrix whose entries contain the singular values of A. The condition number is calculated as the ratio of the largest singular value to the smallest (Press & Vetterling 1992):

$$\text{condition number} = \frac{S_{largest}}{S_{smallest}} \tag{5.24}$$

A large condition number indicates a close to singular Hessian Matrix. When the reciprocal of such a number approaches the machine's floating point precision the accuracy of the calculation of the inverse matrix is not trusted (Press & Vetterling 1992). The precision of MATLAB is 1 in 10^{16}.

5.4.2   Discussion of Results

Tables E.1, E.2 and E.3 in Appendix E contain the estimated standard errors produced by the MATLAB function `cgfiterr`. In order, the column headings for these tables are as follows:

- a_1 is the signal count - total counts if all light from a star was collected by one pixel (i.e. area under the Gaussian curve);

- a_2 is the standard deviation of the gaussian profile;

- a_5 is the CCD pedestal voltage;

- `pixfact` is the number of standard deviations across the fitting window;

- `npix` is the size of the fitting window in pixels;

- SE(a_1) is the standard error in parameter a_1;

- SE(a_2) is the standard error in parameter a_2;

- SE(a_3) is the standard error in parameter a_3;

- SE(a_4) is the standard error in parameter a_4;

- SE(a_5) is the standard error in parameter a_5;

- Max Corr is the maximum correlation between the fitted parameters (Equation 5.13);

- S/N is the signal to noise ratio (equal to $\frac{a_1}{2\pi a_2^2}$ for $\sigma_{noise} = 1$);

- Cond is the condition number (see 5.4.1).

For each window size (`npix`) in the set 3, 5, 7 and 9 pixels wide, the amplitude (a_1) is increased in multiples of 10 within the range of 10 to 10^5, and the standard error of a_2 (SE(a_2)) is displayed. The process is then repeated for Gaussian profiles with standard deviations decrementing from 5 pixels to 1 pixel.

The accuracy requirement in the measurement of seeing, as given by the project specification, is 0.5 arcseconds. Tables E.1, E.2 and E.3 provide some insight into how well this condition is met and the corresponding S/N. For the ST-4 CCD camera which has a resolution of 1.32 arcseconds per pixel, the measurement of 0.5 arcseconds FWHM corresponds to a standard error in the measurement of a_2 equal to:

$$\text{FWHM} = \frac{0.5}{1.32}$$

$$= 0.38 \text{ pixels}$$

$$\begin{aligned}
\text{SE}(a_2) &= \frac{\text{FWHM}}{2.355} \\
&= \frac{0.38}{2.355} \\
&= 0.16 \text{ pixels}
\end{aligned}$$

Hence for any values of SE(a_2) less than 0.16 pixels we have achieved the accuracy goal of measuring the seeing within 0.5 arcseconds (this is not to be confused with the resolution requirement which requires the measurement of seeing down to 1 arcsecond). For a S/N of 1.6 and fitting window equal to 3 pixels wide (see Table E.3), the SE(a_2) is equal to 0.15 pixels. This example best represents the boundary case (in terms of S/N and SE) at which the measurement of seeing with an accuracy of 0.5 arcseconds is achievable (i.e a SE of a_2 less than 0.16 pixels) .

The data in tables E.1, E.2 and E.3 also indicate that for a fixed S/N, the SE of a_2 decreases as the number of pixels in the sampling window increase. For example in Table E.1, for a S/N of 6.4 the SE(a_2) decreases from 4.7×10^{-2} pixels to 8.2×10^{-3} pixels as the sampling window increases from 3 to 9 pixels wide (relevant table entries have been highlighted in bold font). Also observed is that as the size of the fitting window (`npix`) increases, the required S/N decreases. These findings hint at the existence of an optimum sampling window, which is explored further in section 5.5.2.

The condition number and maximum correlation have also been calculated as they indicate the trustworthiness of the results and the validity of the interpretation of SE as the actual error in a_2 respectively. Large condition numbers in the order of 10^{14}, 10^{15} and 10^{16} for a large number of results indicate an ill-conditioned Hessian Matrix. The singularity of the Hessian Matrix becomes obvious in the final line of Table E.3 where the standard deviation of a_2 approaches zero and the standard deviation for a_3 and a_4, which form the exponential term of the Gaussian function, approach infinity.

To reduce this tendency of the Hessian Matrix to become ill-conditioned, a decision was made to keep the stellar centroid, defined by parameters a_3 and a_4, fixed and to perform the estimation of errors based on the remaining three parameters only. Techniques for finding the stellar centroid independently are readily available to astronomers.

5.5 Error Estimation for Fitting with Three Parameters

While results from the previous section which had an acceptable condition number (i.e. in the order of 10^{12} and less) were used to identify the boundaries of the fitting accuracy, most of the results produced using the five parameter error estimation were considered inaccurate due to the large condition numbers. This method was hence considered unreliable in determining how S/N, resolution and fitting window affect the SE of a_2. In this section, we apply the error estimation theory of section 5.3 to the case where the fit to the stellar profile is made for three parameters, namely:

- signal count;

- standard deviation of the Gaussian;

- CCD pedestal voltage.

5.5.1 Application of Theory to Fitting with Three Parameters

The three parameter approach uses the general form of a two-dimensional Gaussian as defined by Equation 5.15 while its only difference with the 5 parameter fitting is that parameters a_3 and a_4 are held fixed. For the three parameter fitting, Equation 5.10 is represented as:

$$\alpha_{kl} = \frac{1}{\sigma^2} \sum_{i=1}^{N} [\frac{\partial y(x_{1_i}; x_{2_i}, a_1, a_2, a_5)}{\partial a_k} \frac{\partial y(x_{1_i}; x_{2_i}, a_1, a_2, a_5)}{\partial a_l}] \qquad (5.25)$$

The partial derivatives for each parameter were calculated as:

$$\frac{\partial y}{\partial a_1} = \frac{1}{2\pi a_2^2} \exp[-\frac{(x_1 - a_3)^2 + (x_2 - a_4)^2}{2a_2^2}] \qquad (5.26)$$

$$\frac{\partial y}{\partial a_2} = \frac{a_1}{2\pi a_2^2} \exp[-\frac{(x_1 - a_3)^2 + (x_2 - a_4)^2}{2a_2^2}][\frac{-2}{a_2} + \frac{(x_1 - a_3)^2 + (x_2 - a_4)^2}{a_2^3}] \qquad (5.27)$$

$$\frac{\partial y}{\partial a_5} = 1 \tag{5.28}$$

Using these partial derivatives the Hessian Matrix may be defined as:

$$[\alpha] = \frac{1}{\sigma^2} \begin{pmatrix} \sum_{i=1}^{N} \frac{\partial y}{\partial a_1} \frac{\partial y}{\partial a_1} & \sum_{i=1}^{N} \frac{\partial y}{\partial a_1} \frac{\partial y}{\partial a_2} & \sum_{i=1}^{N} \frac{\partial y}{\partial a_1} \frac{\partial y}{\partial a_5} \\ \sum_{i=1}^{N} \frac{\partial y}{\partial a_2} \frac{\partial y}{\partial a_1} & \sum_{i=1}^{N} \frac{\partial y}{\partial a_2} \frac{\partial y}{\partial a_2} & \sum_{i=1}^{N} \frac{\partial y}{\partial a_2} \frac{\partial y}{\partial a_5} \\ \sum_{i=1}^{N} \frac{\partial y}{\partial a_5} \frac{\partial y}{\partial a_1} & \sum_{i=1}^{N} \frac{\partial y}{\partial a_5} \frac{\partial y}{\partial a_2} & \sum_{i=1}^{N} \frac{\partial y}{\partial a_5} \frac{\partial y}{\partial a_5} \end{pmatrix} \tag{5.29}$$

The MATLAB function `cgfiterrfixedcentre` calculates the standard error of the three fitting parameters based on the LM theory of error estimation (see Appendix D, section D.4). `cgfiterrfixedcentre` is defined as:

`[sde,cor,cov] = cgfiterrfixedcentre(amp,sig,const,pixfact)`

where:

- `amp` is the signal count (i.e. area under the Gaussian curve and equivalent to a_1 in Equation 5.15);

- `sig` is the standard deviation of the Gaussian profile (a_2 in Equation 5.15);

- `const` is the pedestal voltage (a_5 in Equation 5.15);

- `pixfact` is the number of standard deviations across the fitting window;

- `sde` is the standard error of the five fitting parameters calculated using Equation 5.12;

- `cor` is the maximum correlation between the fitted parameters, where the correlation matrix is calculated using Equation 5.14;

- `cov` is the covariance matrix.

The `cgfiterrfixedcentre` function follows a similar algorithm to that of `cgfiterr` but for a fixed stellar centroid. Low condition numbers and small maximum correlations for the results, provided in Appendix E (Tables E.4 through to), indicate a healthy procedure.

5.5.2 Discussion of Results – The Dependence of SE of Fitted Parameters on S/N, Fitting Window and Resolution

Dependence of SE of Fitting Parameters on S/N

Data in Table E.4, produced using the MATLAB function `cgfiterrfixedcentre`, has been used to identify the dependence of SE of the fitted parameters on the S/N of the Gaussian stellar profile. For a fixed window size (`npix`) , the amplitude (a_1) is increased in multiples of 2 and 5 consecutively within the range of 5 to 10^3, and the standard error of a_2 (SE(a_2)) is displayed. Figures 5.9 and 5.10 indicate a linear relationship between the inverse of the signal to noise ratio and the standard error in the measurement of a_2. a_2 was defined as the standard deviation of the Gaussian distribution, and is proportional to the FWHM by Equation 5.2. Due to the direct relationship between the FWHM and the resolution of the measurement, this parameter provides an indication of the obtainable resolution.

Figure 5.8 identified that resolution, fitting window and S/N all affect the SE of the fitting parameters. This relationship may also be represented as:

$$\mathrm{SE} = \mathbf{f}(\mathrm{resolution},\ \mathrm{fittingwindow},\ \mathrm{S/N}) \tag{5.30}$$

which, having identified the relationship between S/N and SE, may be represented as:

$$\mathrm{SE} = \frac{1}{\mathrm{S/N}}\mathbf{g}(\mathrm{resolution},\ \mathrm{fittingwindow}) \tag{5.31}$$

The theory of LM fitting also confirms the identified relationship between the S/N and SE of a_2. Using the matrix relationship:

$$\mathrm{Inv}(c\mathrm{A}) = \frac{1}{c}\mathrm{Inv}(\mathrm{A}) \tag{5.32}$$

where c is a constant and A is a non-singular matrix, based on Equation 5.10 it may be shown
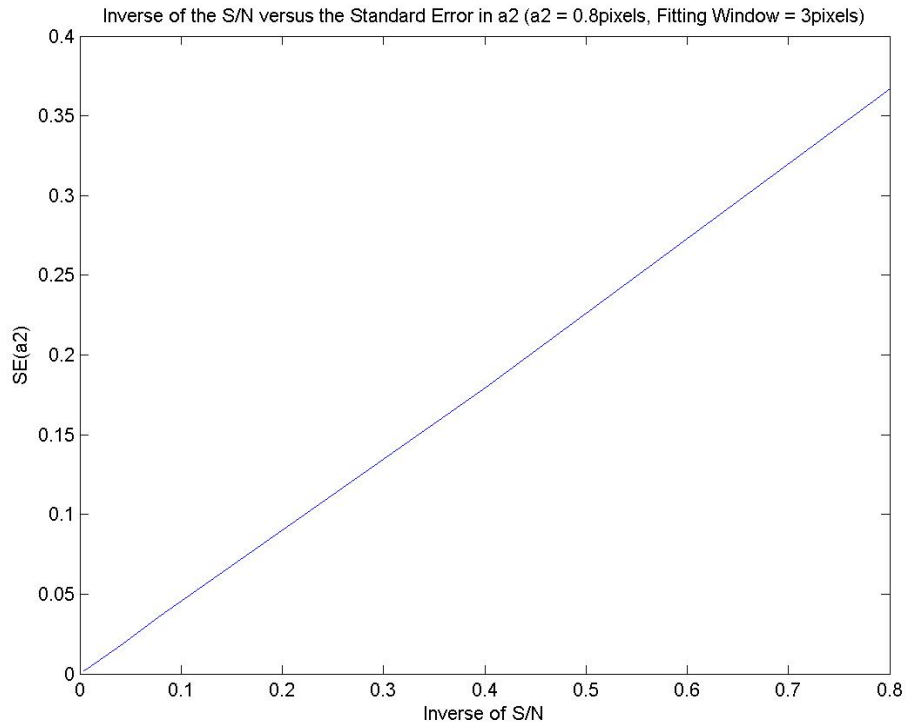
Figure 5.9: A linear relationship exits between the inverse of the S/N and the SE of a_2

that:

$$[\alpha] \propto \frac{1}{\sigma_{\text{noise}}^2}$$

$$\therefore [\alpha]^{-1} \propto \sigma_{\text{noise}}^2$$

Since the elements of the inverse Hessian Matrix are the squares of the estimated standard errors:

$$\text{SE}^2 \propto \sigma_{\text{noise}}^2$$

$$\therefore \text{SE} \propto \sigma_{\text{noise}}$$

and confirms the relationship between S/N and SE. Therefore:

$$\text{SE} = \frac{1}{\text{S/N}}\mathbf{g}(\text{resolution, fittingwindow})$$

Figures 5.9 and 5.10 allow for the quantification of Figure 4.13. Figure 4.13 provided a qualitative sketch on the dependence of the SE in the measurement of seeing on the S/N
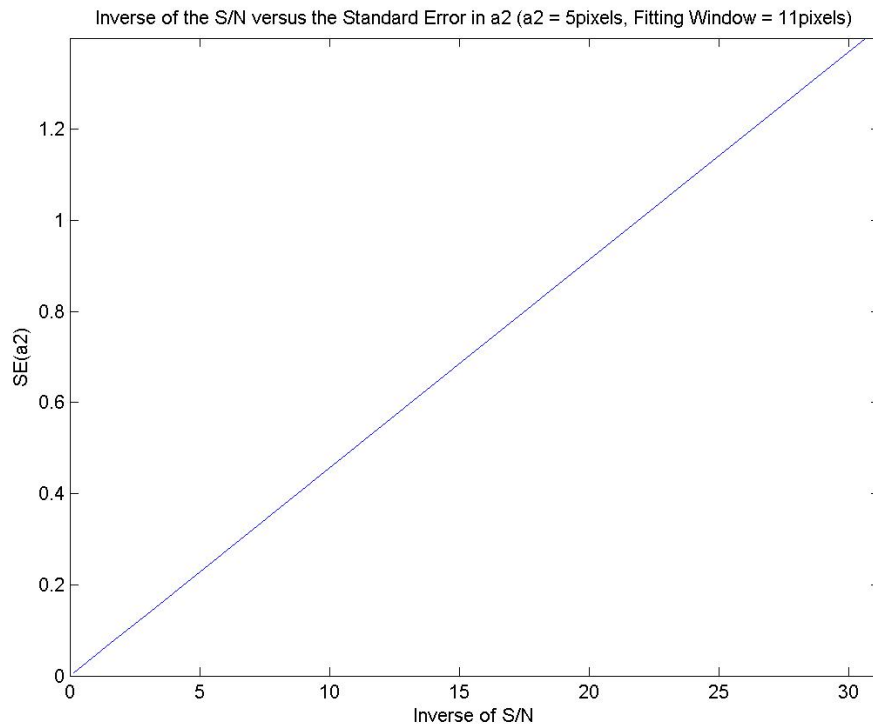
Figure 5.10: A linear relationship exits between the inverse of the S/N and the SE of a_2

provided by the imaging system. This intuitive sketch of a qualitative analysis clearly indicates that for a fixed resolution, the SE in the measurement of seeing decreases as the S/N improves. The validity of Figure 4.13 has now been proven, having identified a linear relationship between the inverse of the S/N and the SE in the measurement of the resolution and hence can be quantified at any fixed resolution.

Dependence of SE of Fitting Parameters on Fitting Window

The dependence of SE of fitting parameters on the fitting window was originally identified using IRIS. However the effect could not be investigated using IRIS as the user could not control the size of the fitting window. The procedure of the previous section was hence used to produce data for the SE of a_2 as a function of window size for a fixed S/N and resolution. The data used has been summarised in Table E.5.

Figure 5.11, plotted using the data from Table E.5, contains two typical examples (for $a_2 = 2$,

S/N = 4 and for $a_2 = 4$, S/N = 5) and indicates the existence of an optimum fitting window at each resolution. An optimum fitting window, measured in pixels, is defined as one in which the SE in the measurement of resolution (i.e. standard deviation of the stellar profile, a_2) is at a minimum. The identification of the type of relationship between fitting window and SE also helped understand why the accuracy of the fitting in IRIS depended so critically on the size of the fitting window.
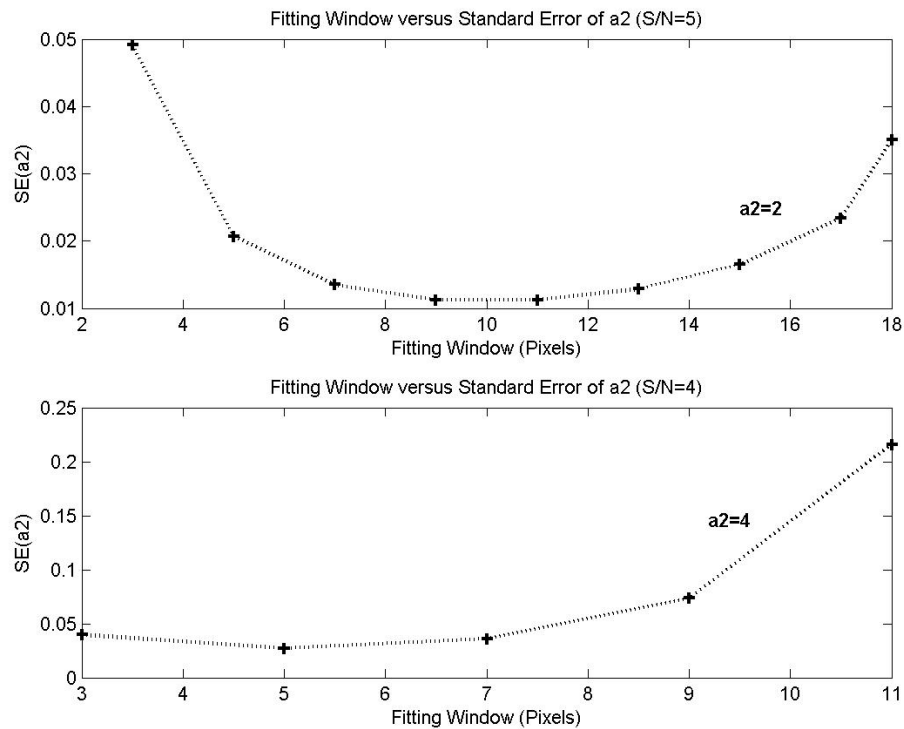
Figure 5.11: An optimum fitting window exists for each resolution. The top figure (for $a_2 = 2$ and S/N = 4) has an optimum fitting window of 10 pixels wide while for the bottom figure (for $a_2 = 4$ and S/N = 5) the optimum fitting window is 5 pixels wide.

The identified dependence between SE of fitting parameters and the fitting window can also be explained by studying the underlying principles. As expected from the analysis in section 5.4.2, as the size of the fitting window increases the effective S/N decreases and vice-versa. It was also concluded from Figures 5.9 and 5.10 that an increasing S/N corresponds to a lower SE in the measurement of a_2. Figure 5.12 represents a Gaussian profile with system noise, where the boundaries of the fitted window have been identified with a pair of vertical lines. This selected fitting region is considered optimum and provides a good S/N and minimum SE in the measurement of a_2.

To understand why the SE of a_2 increases with a larger than optimum fitting window consider Figure 5.13. In Figure 5.13 the boundaries of the fitted window are wider than the optimum window size demonstrated in Figure 5.12. This fitting hence incorporates a larger number of data points (n) thus improving the accuracy of the fit as $\sqrt{n}$. However as we move towards the tails of the Gaussian profile, the S/N drops rapidly due to the profile's exponential behaviour. The rapid drop in S/N therefore results in a high SE in the measurement of a_2.

To understand why the SE of a_2 also increases with a smaller than optimum fitting window consider Figure 5.14. In Figure 5.14 the boundaries of the fitted window are narrower than the optimum window size demonstrated in Figure 5.12. The selected region provides an excellent S/N. However as the relatively flat peak region is used to extrapolate the behaviour of the Gaussian, the information from the sides of the profile which define its width are ignored. This also results in a high SE in the measurement of a_2.
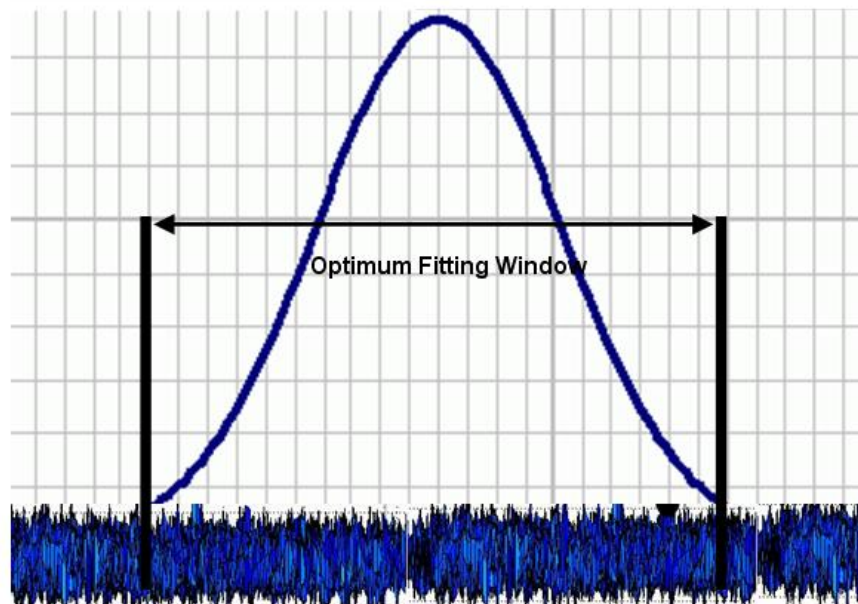
Figure 5.12: A qualitative sketch, illustrating an optimum sampling window which provides good S/N and minimum SE in the measurement of a_2.

Figure 5.11 also illustrates how the optimum window used also depends on the resolution. The top figure (for $a_2 = 2$ and $S/N = 4$) has an optimum window size of 10 pixel, while that for the bottom figure (for $a_2 = 4$ and $S/N = 5$) is 5 pixels.
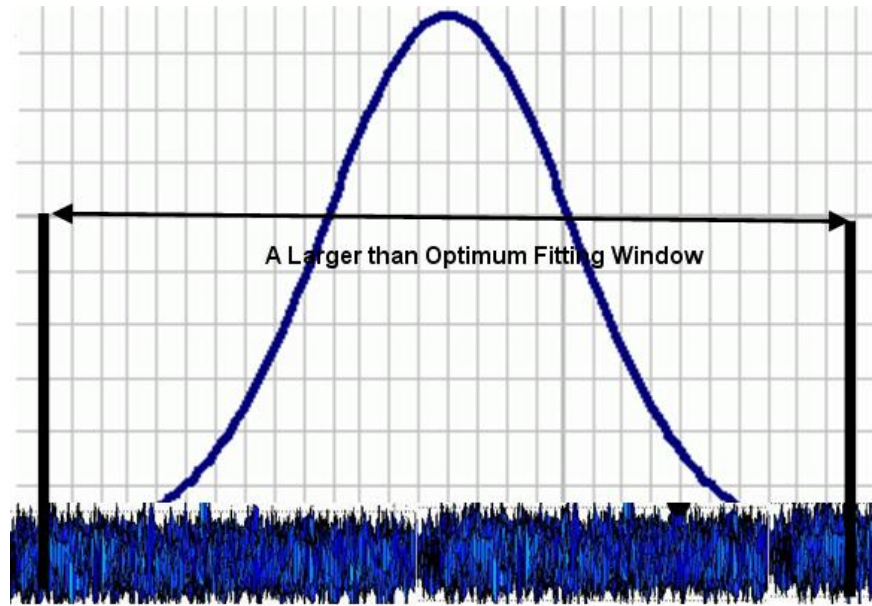
Figure 5.13: A qualitative sketch, illustrating a wider than optimum sampling window size which results in an increase in the SE of a_2.

Dependence of SE of Fitting Parameters on Resolution

To demonstrate the dependence of SE of fitting parameters on resolution, we fixed the S/N for all calculations at 10 (see Tables E.6 and E.7). From Figures 5.9 and 5.10, the SE of other S/N values can exactly be calculated by the established relation that the SE is proportional to the inverse of the S/N.

As the project aims to measure the seeing down to 1 arcsecond, we want to find how low a sampling resolution we can use for a_2 (in pixels) and still have an acceptable SE in the measurement of a_2. Therefore lower values of a_2 correspond to poorer sampling resolution which also corresponds to increased capabilities in resolving good seeing.

We choose to illustrate the resolution dependence by plotting curves of SE versus window width, for various values of resolution. This is because the dependence of SE on window width and resolution was found to be interrelated. Figure 5.15 shows this dependence for fitting windows ranging between 3 and 11 pixels wide and resolution represented by $a_2 = \{0.8, 2, 3, 4, 5\}$. It can be seen that as a_2 decreases (i.e. measuring smaller seeing values), the SE at the optimum fitting window also increases. For example for $a_2 = 2$ the SE at the optimum fitting window of 5 pixels is equal to 1.8×10^{-2}, while for $a_2 = 3$ the SE at
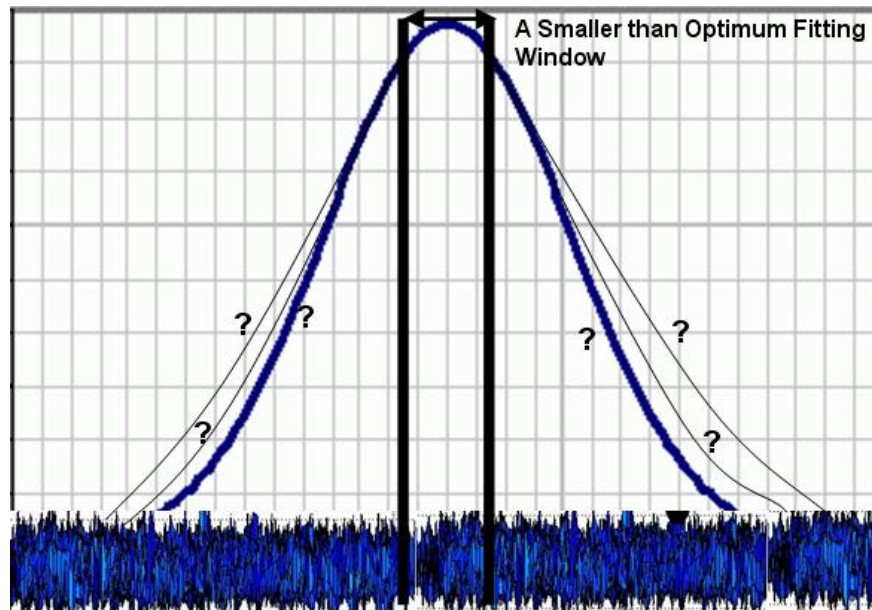
Figure 5.14: A qualitative sketch, illustrating a narrower than optimum sampling window size which results in an increase in the SE of a_2. The multiple profiles demonstrate the fact that the information from the relatively flat peak of the profile is insufficient for correctly extrapolating the behaviour of the Gaussian

the optimum fitting window of 7 pixels is equal to 7.37×10^{-3}.

The dependence of SE on the sampling window size, discussed in the previous section, is obvious for most values of a_2. In fact each curve has a J-like shape. This shape is most obvious for $a_2 = 2$ which reaches its optimum fitting window at 5 pixels, but also occurs for other a_2 values.

For low values of a_2, the calculation failed for large window sizes, such that for $a_2 = 0.8$, only one point was produced. For $a_2 < 0.8$ the method of estimating the standard errors failed owing to the high correlation between the fitted parameters. This procedure also failed to produce the standard errors in the measurement of a_1 and a_2. For example for a S/N equal to 10 and $a_2 = 0.5$, this method produces a maximum correlation of 241% and zero SE in the measurement of a_1 and a_2.

We have thus shown that the lowest resolution that can be explored with our error estimation technique is $a_2 = 0.8$ pixels. This resolution corresponds to a S/N equal to 10 where the fitting can be made with an accuracy of 0.046 pixels (see Table E.5).
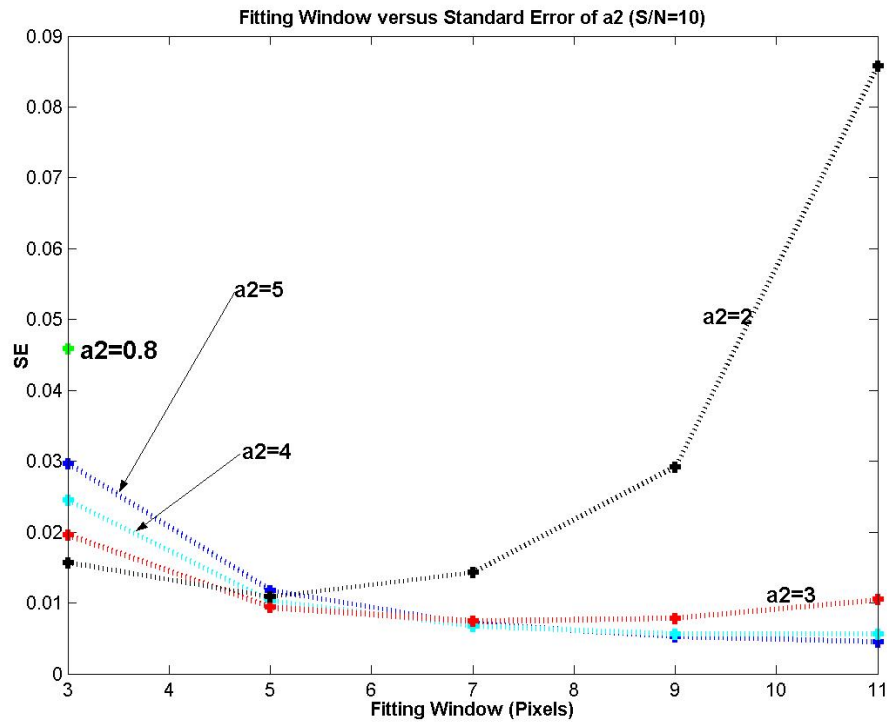
Figure 5.15: For $a_2 < 0.8$ the Method of Calculating the Standard Errors Fails.

Application of Results to ST-4 CCD Camera and Meade-10 Telescope   These values could hence be used to evaluate the performance of the ST-4 CCD camera. The SE required to measure the seeing FWHM within 0.5 arcseconds is 0.16 pixels (see section 5.4.2). The ST-4 and Meade-10 produce a S/N of 12.9 for a magnitude 12 target star (see Table 4.3). The required S/N is therefore:

$$S/N = \frac{10 \times 0.046}{0.16}$$
$$= 2.9$$

which is below that provided by the ST-4 and Meade-10 (i.e we have sufficient S/N). To determine whether the ST-4 and Maede-10 will provide sufficient resolution, based on our new findings, requires the calculation of the number of arcseconds of seeing below which fitting theory does not assist with the error estimation. Using Equation 5.2 the FWHM of the Gaussian distribution is:

$$FWHM = 2.355 \times 0.8 = 1.88 \text{ pixels}$$

To convert this to arcseconds for the ST-4, we multiply by 1.32 arcseconds per pixel so that the FWHM can be obtained as:

$$\text{seeing FWHM} = 1.32 \times 1.88 = 2.5 \text{ arcseconds}$$

Therefore the error estimation fails to assist with the calculation of the SE for the measurement of 1 arcsecond seeing as required by the project specification. However the error estimation shows that for the ST-4, with a S/N ratio of 2.9, seeing FWHM can be measured down to 2.5 arcseconds with an accuracy well within the target of 0.5 arcseconds.

The lowest resolution this method could prove as obtainable was $\text{FWHM} = 2.5$ arcseconds (at $\text{SE} = 0.5$ arcseconds). This is a modest improvement to the Nyquist resolution which requires the FWHM to cover at least 2.355 pixels, which for the ST-4 corresponds to 3.1 arcseconds. Because the method failed below 0.8 pixels resolution, it was of interest to see if further improvement could be obtained.

5.6   Simulations

In this section noisy Gaussian stellar profiles will be simulated and then fitted for the FWHM using the Levenberg-Marquardt technique. By repeating this method for different sets of noise, the expected SE of FWHM can be calculated for given fitting parameters. Simulations have been performed as:

- They provide an environment in which the theory can be tested;

- it is easy to obtain the complete range of test data (rather than wait for the sky to produce them);

- theory has been unable to provide all the answers (i.e. it failed below $a_2 = 0.8$ pixels);

- they allow us to investigate whether we can improve on the best obtainable seeing (so far $a_2 = 0.8$ pixels).

Although the simulations aim to provide an environment to test the real data, for simplicity the following assumptions have been made:

- the stellar image is circular;

- the noise is normally distributed and independent (i.e. independent from pixel to pixel).

Although these assumptions result in a simulation which is partially artificial, it provides us with a confirmation on the correct application of the LM theory. The simulations also enable us to fit in an environment where we can control the influencing parameters on the SE of the fitting parameters, such as the window size, hence providing a superior environment compared to IRIS.

5.6.1   Practical Application of the LM Technique

As discussed in section 5.3 the LM technique is a way of finding the parameters which minimises the sum of the squared differences between the data and the model, in the case where the model is a non-linear function of parameters. To provide some practical insight into this technique, consider a function of y of two parameters a_1 and a_2. Then:

$$\chi^2(a) = \frac{1}{\sigma^2} \sum_{i=1}^{N} [y_i - y(\vec{x}_i, a_1, a_2)]^2$$

where y_i are the observations and $y(\vec{x}_i, a_1, a_2)$ is the model.

A simplified qualitative sketch of the surface defined by χ^2 is provided in Figure 5.16. The LM technique will find the values of the parameters a_1 and a_2 at which χ^2 is a minimum and hence calculates the best fit equation. To illustrate this minimisation, consider the linear function $y = y(\vec{x}_i, a_1, a_2)$. A graphical representation of this linear function is provided in Figure 5.17, where the position of the line has been optimised to minimise the sum of the squared deviations (represented by the vertical lines) of the data y_i from the line.

For this linear case, a formula can be given to directly calculate the two parameters from the data y_i and the $\vec{x}_i$. For a non-linear case (i.e. a function with non-linear dependencies on the parameters) the minimisation of χ^2 requires an iterative technique. The aim of this technique is to calculate the minimum point on the surface defined by χ^2. For example for a five
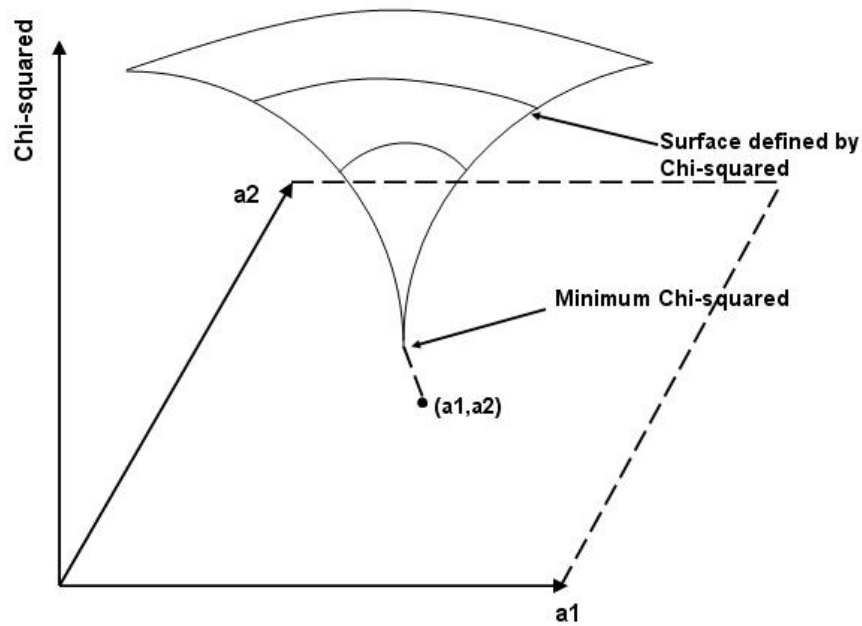
Figure 5.16: A simplified qualitative sketch of the surface defined by χ^2. The LM technique will find the values of a_1 and a_2 at which χ^2 is a minimum.

parameter fitting, the χ^2 function defines a surface in 6 dimensional space $(a_1, a_2, a_3, a_4, a_5, \chi^2)$ and the algorithm will aim to solve for the minimum point on this surface. Given trial values for the parameters a_1, a_2, a_3, a_4 and a_5, it develops a procedure that improves the trial solution. The procedure is then repeated until χ^2 effectively stops decreasing. The procedure for improving the trial solution is as follows:

- perform local linearisation at the trial point $(\vec{a}_i)$;

- step down the gradient of the surface using the Hessian Matrix (its elements were given by Equation 5.10) at this point;

- calculate the new trial point;

- repeat the procedure until the minimum point is reached.

5.6.2   The Simulation Function

The MATLAB function `cgaussianmodelfit` performs the simulation (see Appendix D, section D.5). `cgaussianmodelfit` is defined as:
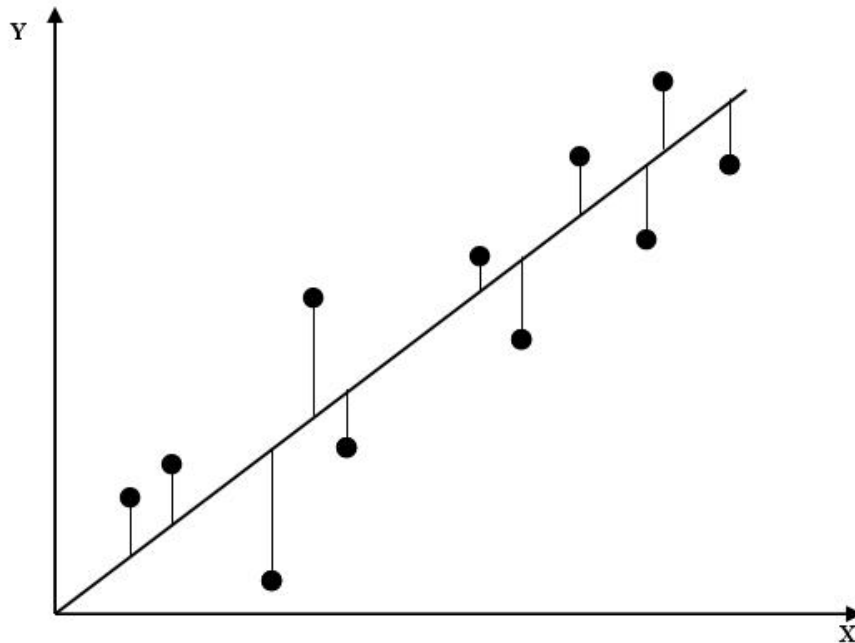
Figure 5.17: The position of the line $y = a_1 x + a_2$ has been optimised for a minimum χ^2 value.

```
cgaussianmodelfit(npix,a,aguess,ause,noised,endcond,pstep)
```

where:

- `npix` defines the size of the fitting window;

- `a=[amp sd x10 x20 const]` is the parameter vector:

  - `amp` is the signal count (i.e. area under the Gaussian distribution),

  - `sd` is the standard deviation of the Gaussian profile,

  - `x10` and `x20` define the stellar centroid on the CCD plane,

  - const is the pedestal voltage;

- `aguess` is a vector of initially guessed parameters;

- `ause` is a vector defining the number of parameters to fit for (e.g. for a 3 parameter fitting to `amp`, `sd` and `const ause=[1 1 0 0 1]`);

- `noisesd` id the standard deviation of the noise;

- `endcond` defines when to stop the iterations (i.e. when the minimum χ^2 value has been reached);

- `pstep` can be set to 1 in order to step through each iteration.

`cgaussianmodelfit` calls on the function `lmnlsqfit`. `lmnlsqfit` fits to a non-linear function using LM method (see Appendix D, section D.6) and in doing so it calls on `mrqmin` which performs a single iteration. `mrqmin` is a MATLAB implementation of the C code provided by Press & Vetterling (1992) for one iteration (see Appendix D, section D.7). `lmnlsqfit` repeats each iteration while:

- the fractional change in χ^2 is positive (`fractdcs`≥ 0): This shows that χ^2 has increased in the last step, so the step was not adjusted optimally, OR

- the fractional change in χ^2 is negative AND its absolute change is larger than the final resolution required (`(fracdcs< 0)`&`(fracdcs)`<`(-endcond)`): Press & Vetterling (1992) recommend an `endcond` set to a fractional amount like 10^{-3}, which suggests stopping on the first or second occasion that χ^2 decreases by a negligible amount.

`marqmin` performs the local linearisation. The linearised solution used by the LM technique is given by:

$$\vec{a}_{next} - \vec{a}_{cur} = -\text{constant} \times \nabla\chi^2(a_{cur}) \tag{5.33}$$

where:

- $\vec{a}_{next}$ is the new set of parameters;

- $\vec{a}_{cur}$ is the current set of parameters;

- $\nabla\chi^2(a_{cur})$ is the curvature of the surface defined by χ^2 at the point of the current parameters;

- The constant is set small enough to ensure the step size is not too large. Its value is proportional to the inverse of the curvature of the surface. This is because for a large change in gradient (i.e curvature) the step size must be small, since a large step size may

result in a gradient which is not the true representation (i.e the linear approximation fails).

`mrqmin` calls the function `mrqcof` for the computation of the Hessian Matrix. `mrqcof` is also a MATLAB implementation of the C code provided by Press & Vetterling (1992) (see Appendix D, section D.8). In turn `mrqcof` calls `afitfun`, which for input values of $\vec{x}$ and $\vec{a}$ calculates the vector of derivatives, $dydx$, and the model Gaussian function, `ymod`=$y(x_i; \vec{a})$ (see Appendix D, section D.9).

5.6.3   Simulations, Results and New Findings

In this section we have applied the functions introduced in the previous section to fit to simulated noisy Gaussian stellar profiles using the non-linear least squares Levenberg-Marquardt technique. In order to obtain statistically significant results each simulation was repeated 1000 times, and the mean value of the results was used to check for statistical bias while the standard deviation provided the expected standard error in the measurement of the a_2 value (i.e. resolution). This method was successful in extending the capabilities of the error estimation theory (see section 5.5.2), which failed for resolutions below 0.8 pixels. It was found that it is possible to improve over the Nyquist resolution limitation by a factor larger than two and by a factor of near two over that obtained based on the error estimation theory. The simulations have also allowed for the quantification of the concepts proposed in section 4.6 of chapter 4 that helped understand the dependence of SE on S/N and resolution.

It has been shown that the measurement of seeing down to 1 arcsecond is not possible by using the ST-4 CCD camera. However much improvement has been obtained over the Nyquist resolution limitation and the project specifications are almost within reach.

Method

The functions introduced in section 5.6.2 have been used to simulate and fit to the noisy Gaussian stellar profiles. As random Gaussian noise was introduced into each stellar profile

multiple iterations were performed. To do this the `manylm` MATLAB function was written. To perform the simulations `manylm` calls on the `cgaussianmodelfit` function. The number of simulations to be performed are set by the `numit` input parameter. The function is as follows:

```
% Function:    manylm.m
% Purpose:     To call on the cgaussianmodelfit function,
%              in order to simulate a user defined number
%              of circular Gaussian stellar profiles and fit
%              using the LM technique.
% Syntax:      [fit]=manylm(npix, a, aguess, ause, noisesd,
%                           endcond, numit)
% Input:       npix = size of the fitting window
%                     (both x and y)
%              a = [amp sd x10 x20 const] is the parameter vector:
%                  amp = signal count
%                  (i.e. area under the Gaussian distribution)
%                  sd = standard deviation of the Gaussian profile
%                  x10 and x20 = stellar centroid on the CCD plane
%                  const = pedestal voltage
%              aguess = vector of initially guessed parameters
%              ause = vector defining the number of parameters
%              to fit for (e.g. for a 3 parameter fitting
%              ause=[1 1 0 0 1])
%              noisesd = standard deviation of the noise
%              endcond = condition at which to stop the
%                        iterations (i.e. when the fractional
%                        change in chi-squared is less than
%                        the end condition value set,
%                        Vetterling (1992) recommends endcond=0.001)
%              numit = user defined number of simulations
% Output:      fit = vector containing the mean a2 values
%                    and their standard deviation
```

```
function [fit]=manylm(npix, a, aguess, ause, noisesd, endcond,numit)


% Define the vector of a2 values
a2s=zeros(1,numit);


% Perform the simulation and fitting 'numit' times
for (i=1:numit)
    % Simulate and fit to the Gaussian stellar profile
    a2 = cgaussianmodelfit(npix, a, aguess, ause, noisesd, endcond);
    % Populate the a2 vector with the fitted values
    a2s(i)=a2;
end


% Calculate the mean of the a2 values
fit(1)=mean(a2s)
% Calculate the standard deviation of the a2 profile
fit(2)=std(a2s)
% Plot a histogram of the a2 values
hist(a2s);
```

`manylm` returns the vector `fit` which contains the mean and standard deviation of the fitted a_2 values. The mean value has been calculated as it is to be compared with the user specified a_2 value (i.e. input parameter `sd` in the `manylm` function) to ensure the absence of statistical bias in the results. The standard deviation of this distribution represents the fact that 68% (i.e. one standard deviation) of the time, the error obtained in fitting to the noisy Gaussian stellar profile will lie within this value. It therefore represents the SE in fitting to a_2.

An a_2 value of 0.8 pixels was taken as a starting point for the simulations. Error estimation theory failed to assist with the calculation of the SE for the measurement of 1 arcsecond seeing as required by the project specification. However the error estimation successfully showed that using the ST-4, with a S/N ratio of 2.9, seeing FWHM can be measured down to

2.5 arcseconds (i.e. 0.8 pixels) with an accuracy well within the target of 0.5 arcseconds.

The main focus then was to decrement the a_2 value from the starting point of 0.8 pixels to 0.32 pixels, which is the resolution in pixels corresponding to 1 arcsecond seeing:

$$\text{FWHM} = \frac{1}{1.32}$$
$$= 0.75 \text{ pixels}$$
$$a_2 = \frac{\text{FWHM}}{2.355}$$
$$= \frac{0.75}{2.355}$$
$$= 0.32 \text{ pixels}$$

Lower values of a_2 were also considered in order to test the idea that, with a high S/N and poor resolution, fitting to a noisy Gaussian stellar profile is possible (see Figure 4.12).

The S/N obtained by the ST-4 CCD Camera for the measurement of a magnitude 12 target star was 12.9. A range of S/N values was used in the simulations as it was found that for larger S/N values (i.e. greater than that provided by the ST-4) the fitting was possible down to 1 arcsecond seeing. It was important to vary the S/N over a wide range as it was found that there is a limiting S/N below which we cannot obtain a fitting at a particular resolution.

The width of the fitting window (`npix`) was varied in order to ensure that its behaviour was consistent with the findings in section 5.5.2.

Interpretation of Results

From the many simulations that were performed, the following seven critical cases have been selected as they demonstrate:

- the obtained improvements over the error estimation theory;

- the identification of the boundary which separates regions which can and can not be fitted;

- the regions where the fitting fails.

Case A (Improvement) This case confirms the conclusion of section 5.5.2 that a resolution of 0.8 pixels can be achieved. This is achieved by showing a modest improvement in the lowest obtainable resolution over that provided by the error estimation theory.

The resolution has been set to 0.7 pixels while the signal count (`amp`) has been set to 19, which corresponds to a S/N of 6.2 (calculated using Equations 4.4, 4.5 and 4.6). A S/N of 6.2 corresponded to the minimum S/N (at 0.7 pixels resolution) at which fitting was found to succeed.

Figure 5.18 shows that the fitted a_2 values are centred about 0.7 pixels and typically lie within ± 0.1 pixels of this value. Indeed this distribution has a mean value of 0.7096 pixels and a standard deviation (i.e. SE(a_2)) equal to 0.1073 pixels, which is in agreement with Figure 5.18. Thus we can say that the fitting procedure has succeeded. The closeness of this mean to the input resolution of 0.7 pixels shows that the fitting procedure is statistically unbiased, and the standard deviation of this distribution shows that we can typically fit within 0.1 pixels of the true value. Figure 5.19 is a screen shot of MATLAB showing the convergence of χ^2 towards its minimum value (see section 5.6.1) for a single iteration. It was obtained by setting the input parameter `pstep` to 1 in the `cgaussianmodelfit` function.
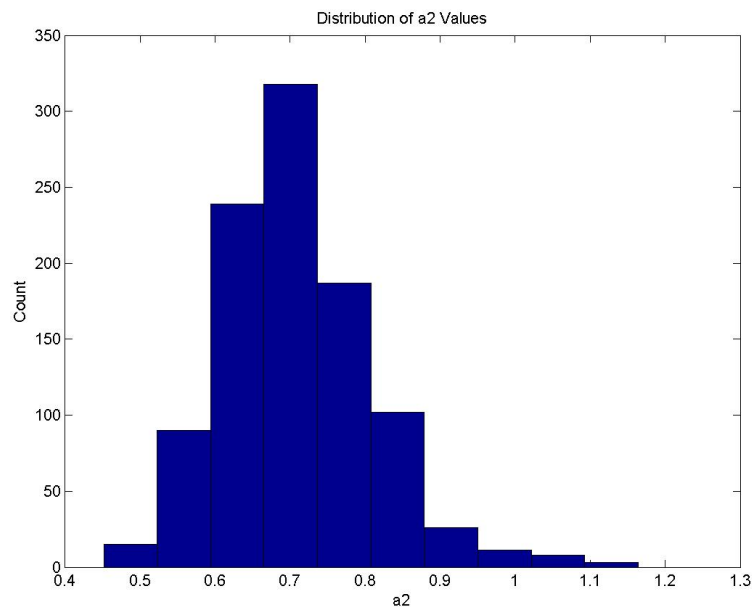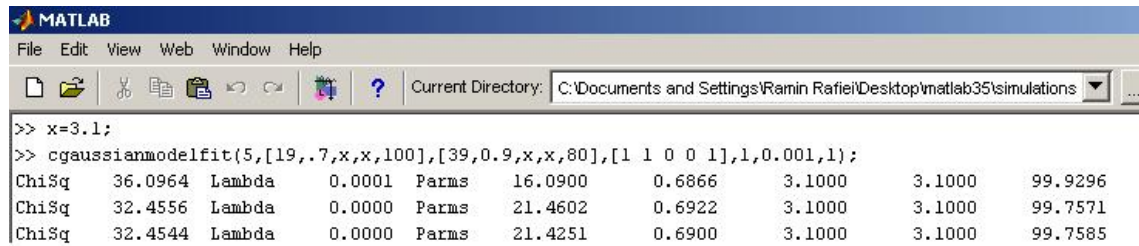
Figure 5.18: Case A – Distribution of the 1000 fitted a2 Values.

Figure 5.19: MATLAB ouput, showing the convergence of χ^2 towards its minimum value for a single iteration.

Case B (Improvement)   This case shows a substantial improvement in the lowest obtainable resolution over Case A. The resolution has been lowered to 0.5 pixels, while the signal count has been set to 19 (i.e. S/N equal to 12.1). 12.1 is the minimum S/N at the resolution of 0.5 pixels in which fitting was found to succeed.

Figure 5.20 shows that the fitted a_2 values are centred about 0.5 pixels and typically lie within ± 0.05 pixels of this value. This distribution has a mean value of 0.4987 pixels with a SE(a_2) equal to 0.0463 pixels, in agreement with Figure 5.20. The closeness of this mean to the input resolution of 0.5 pixels shows that the fitting procedure is statistically unbiased, and the standard deviation of this distribution shows that we can typically fit within 0.05 pixels of the true value. Compared to Case A it can be clearly seen that for fitting at lower resolutions, a
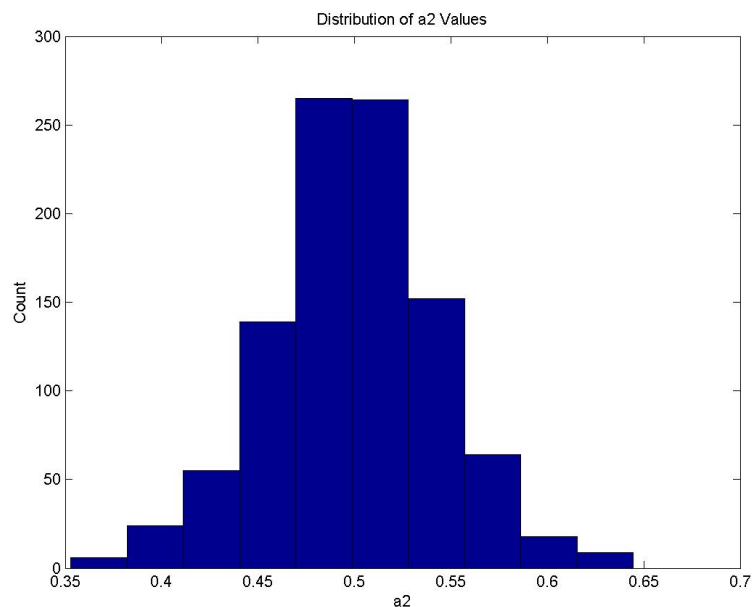
Figure 5.20: Case B – Distribution of the 1000 fitted a2 Values.

higher S/N is required.

Case C (Boundary Region)   This case demonstrates the lowest obtainable resolution at the S/N of the ST-4 CCD camera (i.e equal to 12.9). This resolution is equal to 0.45 pixels, for a signal count of 16.4 (or S/N of 12.9). Figure 5.21 shows that the fitted a_2 values are centred about 0.45 pixels and typically lie within ± 0.05 pixels of this value. This distribution has a mean value of 0.445 pixels and the $SE(a_2)$ equal to 0.0518 pixels, which is in agreement with Figure 5.21. The closeness of this mean to the input resolution of 0.45 pixels shows that the fitting procedure is statistically unbiased, and the standard deviation of this distribution shows that we can typically fit within 0.05 pixels of the true value.
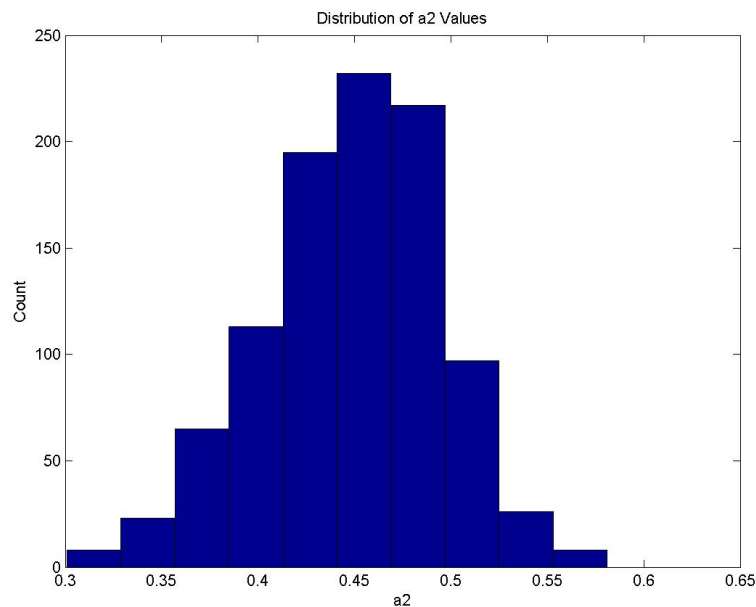
Figure 5.21: Case C – Distribution of the 1000 fitted a2 Values.

This case demonstrates the boundaries of performance of the ST-4 CCD camera. Although the resolution of 0.32 pixels for the measurement of seeing down to 1 arcsecond has not been reached, the minimum obtainable resolution has been improved by a factor of 1.8 over that provided by the error estimation theory (i.e. 0.8 pixels). Most important is the improvement shown over the Nyquist resolution limitation which requires the FWHM of the stellar profile to cover at least 2.355 pixels. Therefore, based on this criterion and using the ST-4 with a resolution of 1.32 arcseconds per pixel, it is expected that seeing can be measured down to

only 3.1 arcseconds:

$$\text{seeing(arcseconds)} = 2.355 \times 1.32$$

$$= 3.1 \text{ arcseconds}$$

Using Equation 5.2, a resolution of 0.45 pixels corresponds to a FWHM of 1.1 pixels which, using the ST-4, corresponds to a seeing value of 1.4 arcseconds:

$$\text{seeing(arcseconds)} = 1.1 \times 1.32$$

$$= 1.4 \text{ arcseconds}$$

thus showing an improvement factor of 2.1 over the Nyquist resolution limitation.

Case D (Boundary Region)   Case D demonstrates that fittings can be made to Gaussian stellar profiles down to the 1 arcsecond (i.e. 0.32 pixels) resolution as required by the project specification. However the minimum S/N required for this fitting is much greater than that provided by the ST-4 CCD camera. The minimum S/N at the resolution of 0.32 pixels was 54.4, which is over 4 times greater than that provided by the ST-4. Figure 5.22 shows that the fitted a_2 values are centred about 0.32 pixels and typically lie within ± 0.02 pixels of this value. This distribution has a mean value of 0.3175 pixels and the SE(a_2) equal to 0.0273 pixels, which is in agreement with Figure 5.22. The closeness of this mean to the input resolution of 0.32 pixels shows that the fitting procedure is statistically unbiased, and the standard deviation of this distribution shows that we can typically fit within 0.03 pixels of the true value.

Case E (Boundary Region)   Case E identifies the minimum resolution at which a simulated Gaussian stellar profile can be fitted to, and its corresponding limiting S/N. Simulations have shown that the minimum obtainable resolution is 0.25 pixels. It was found that for a resolution below 0.25 pixels, independent of S/N, the fitting failed. At 0.25 pixels resolution, the minimum S/N requirement was 382. This resolution corresponds to a FWHM of 0.6 pixels wide, almost 4 times smaller than the 2.355 pixels required by the Nyquist resolution limitation.
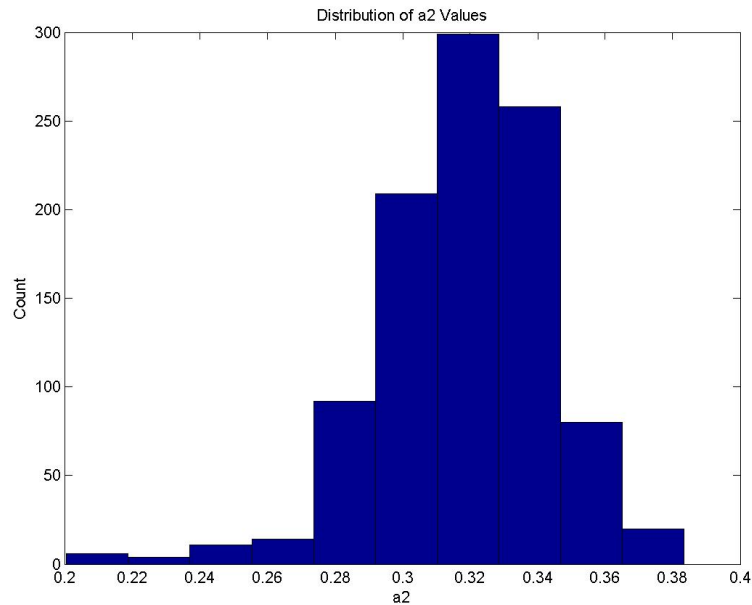
Figure 5.22: Case D – Distribution of the 1000 fitted a2 Values.

Figure 5.23 shows that the fitted a_2 values are centered about 0.25 pixels and typically lie within ± 0.01 pixels of this value. This distribution has a mean value of 0.2477 pixels and the SE(a_2) equal to 0.0146 pixels, which is in agreement with Figure 5.23. The closeness of this mean to the input resolution of 0.25 pixels shows that the fitting procedure is statistically unbiased, and the standard deviation of this distribution shows that we can typically fit within 0.015 pixels of the true value.

Case F (Boundary Region)   Case F demonstrates that if no noise is present in the imaging system (or for a very large S/N), the fitting to the Gaussian stellar profile can be made with zero SE. This finding is similar to that identified by using IRIS (see section 5.2.3) where for an imaging system with zero noise, the seeing was measured accurately for resolutions below that of the Nyquist resolution. In this simulation the resolution has been set to 0.7 pixels and a S/N of 1624. The distribution in Figure 5.24 has a mean value of 0.7000 pixels and the SE(a_2) equal to 0.0004 pixels. From Figure 5.24 it can be confidently deduced that each fitting has been made accurately with close to zero SE (i.e a very small standard deviation in the a_2 values).
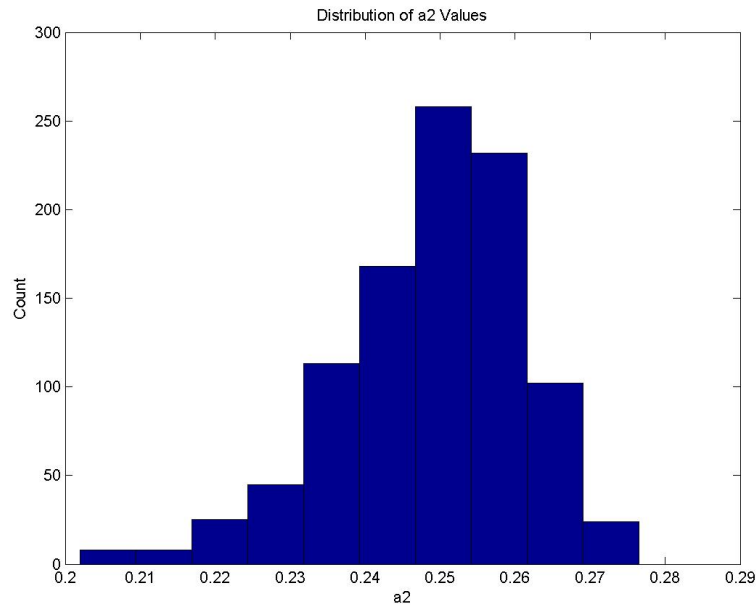
Figure 5.23: Case E – Distribution of the 1000 fitted a2 Values.

Case G (Failure)   Case G demonstrates the outcome when the S/N is reduced below the limiting S/N. The limiting S/N value for a fit at 0.45 pixels resolution was identified in Case C to be 12.9. In this case the S/N has been reduced to 9. During the simulation the Hessian Matrix became singular on many iterations which indicates the existence of a limiting S/N below which we can not reliably obtain a fitting for a particular resolution. The inability to reliably fit to this stellar profile can also be seen in Figure 5.25. In a few cases the fitting was performed well below the supplied parameter of 0.45 pixels, indicating problems within the fitting procedure (i.e. in obtaining the inverse of the Hessian Matrix). It was also surprising to find that in quite a few cases, accurate results were obtainable.

New Findings

From the many simulations that have been performed, of which seven critical cases were reported in the previous section, the following 'new findings' have been made:

- **Improvement over Error Estimation Theory**: It has been shown that $a_2 = 0.8$ pixels is the lowest resolution that can be explored using the error estimations technique. Cases A, B, C, D and E all demonstrate that fittings to Gaussian stellar profiles can be
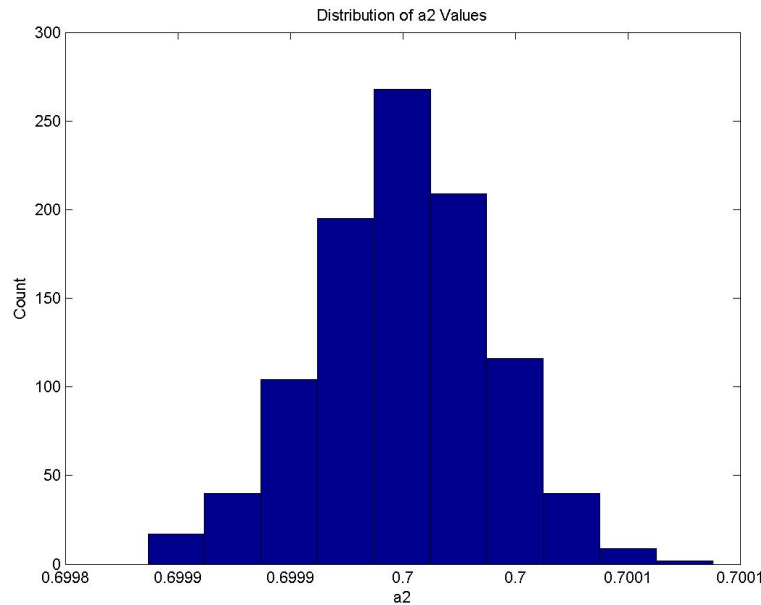
Figure 5.24: Case F – Distribution of the 1000 fitted a2 Values.

made at resolutions below 0.8 pixels.

- **Improvement over the Nyquist Resolution Limitation**: As previously defined, the Nyquist sampling resolution criterion requires a Gaussian distribution with a FWHM corresponding to 2.355 pixels. Based on this criterion the measurement of seeing at the spatial resolution of the ST-4 is expected down to 3.1 arcseconds only. Case C has shown that the measurement of seeing at the S/N of the ST-4 CCD camera is possible down to 1.4 arcseconds. This finding shows an improvement factor of 2.1 over the Nyquist resolution criterion.

- **Existence of a limiting S/N**: A comparison between Cases C and G have identified the existence of a limiting S/N below which a fitting can not be made to the stellar profile. Case C identifies that for a resolution of 0.45 pixels a minimum S/N equal to 12.9 is required. Case G reduces this limiting S/N to 9, and shows that the fitting fails.

- **Lowest Obtainable Resolution**: The lowest obtainable resolution and its minimum corresponding S/N have been calculated in Case E. The minimum resolution corresponds to a stellar profile with a FWHM equal to 0.6 pixels, obtained with a limiting S/N of 382. Although a FWHM of 0.6 pixels corresponds to the measurement of seeing down to 0.8 arcseconds, it requires a S/N 30 times greater than that provided
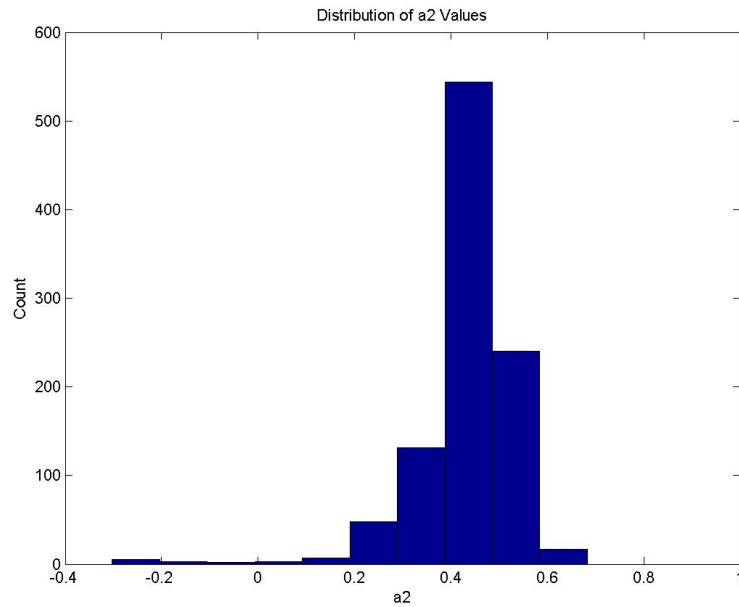
Figure 5.25: Case G – Distribution of the 1000 fitted a2 Values.

by the ST-4 CCD Camera.

- **Quantification of Figure 4.12**:

In section 4.6 the following question was raised:

> *What is the minimum S/N at the resolution of our detectors that will allow us*
> *to determine seeing within 0.5 arcseconds accuracy and down to*
> *one-arcsecond seeing?*

In obtaining a solution to this question, Figure 4.12 was drawn, which provided an intuitive sketch of a qualitative analysis to the solution. Figure 5.26 has successfully quantified the boundaries between regions at which the seeing can (i.e. fitting region) and can not be resolved (i.e. non-fitting region). Hence it can be said that the minimum S/N at the resolution of the ST-4 that will allow us to determine the seeing within 0.5 arcseconds accuracy and down to 1 arcsecond seeing (i.e. resolution equal to 0.32 pixels) is 54.4 (4 times greater than the obtainable S/N by the ST-4). However what is also seen is the minimum resolution at which we can fit at the S/N provided by the ST-4 (resolution of 0.45 pixels corresponds to a S/N of 12.9). Figure 5.26 also shows that for a resolution below 0.25 pixels, independent of S/N, the fitting fails.
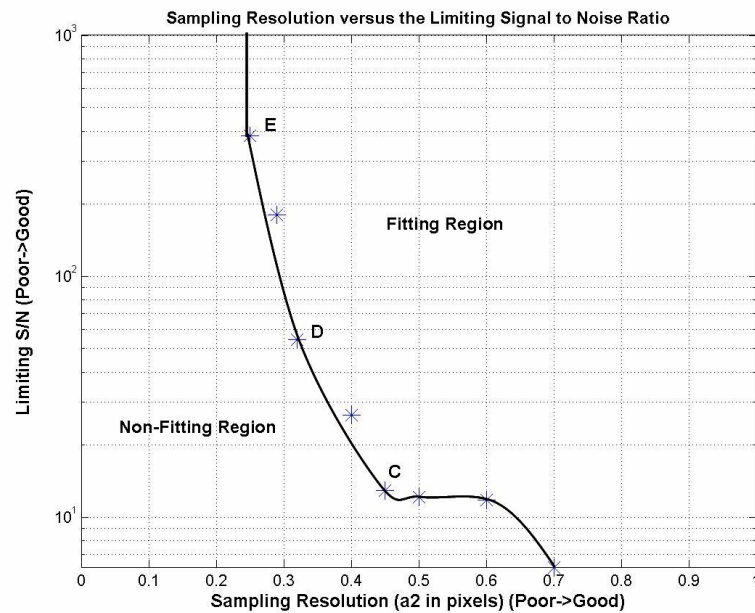
Figure 5.26: Quantification of Figure 4.12. The boundary line separates regions within which the seeing can and can not be resolved. It clearly identifies the lowest sampling resolutions (i.e. poorest resolutions) and their corresponding S/N which allow for the seeing to be resolved. The letters correspond to the points calculated in the boundary cases of the previous section.

5.7 Estimated System Performance against Conventional Limitations

The project aim was to evaluate the low-cost measurement of astronomical seeing within the range of 1-10 arcseconds and to an accuracy of 0.5 arcseconds. In Chapter 4 it was shown that conventional limitations gave a Nyquist resolution requiring the FWHM of the Gaussian stellar profile to be 2.355 pixels wide, which for the ST-4 corresponded to the measurement of seeing down to 3.1 arcseconds. The simulated LM fitting to Gaussian stellar profiles has shown that the measurement of seeing at the S/N of the ST-4 CCD camera is possible down to 1.4 arcseconds with an accuracy of 0.16 arcseconds. The results summarised in Table 5.1 show that although the project aim can not be achieved using the ST-4 CCD camera, the LM fitting technique has exceeded conventional limitations and the results lie very close to the project requirements.

Table 5.1: A Comparison Between the Project Requirements, Conventional Limitations and Achieved Results

	Resolution (arcseconds)	Accuracy (arcseconds)
Project Target	*1*	*0.5*
Nyquist Criterion	3.1	–
Error Estimation Theory	2.5	0.14
Fitting Simulations	1.4	0.16

5.8   Chapter Summary

This chapter has successfully proven the initial investigations made in Chapter 4 that Nyquist does not set the ultimate limit on the accurate measurement of seeing. While simulations have shown that the ST-4 CCD can not be used for the measurement of seeing down to 1 arcsecond, simulations based on the Levenberg-Marquardt non-linear least-squares fitting technique have exceeded conventional limitations by a factor of 2.1 and have shown that seeing measurements down to 1.4 arcseconds are possible.

Chapter 4 identified the dependence of the accuracy of seeing measurements (i.e. SE of the fitting) on the S/N and resolution of the profile sampling. The use of IRIS in this chapter made the dependency of the SE of the fitting on the fitting window size apparent, but this relationship could not be studied. The nature of these dependencies was later identified using error estimation theory, which showed a moderate improvement over the Nyquist resolution criterion but had difficulties with singularities for resolutions below 0.8 pixels.

To examine actual error distributions from fitting to Gaussian stellar profiles, Levenberg-Marquardt non-linear least-squares fitting was performed on a large number of simulated profiles. From this it was shown that, using the ST-4, seeing measurements down to 1.4 arcseconds are possible. The study also identified the lowest S/N as a function of resolution for which the fitting is successful (see Figure 5.26), thus quantifying the qualitative boundary suggested in Figure 4.12. Finally the lowest obtainable resolution of 0.25 pixels (i.e FWHM equal to 0.6 pixels) was calculated, below which independent of the S/N the fitting failed at all times.

Although these studies have focused on the ST-4 CCD camera in combination with the Meade-10 telescope, this system of simulations can be used for any camera-telescope system in order to find their expected performance and system limits.

Chapter 6

Improvements from Fitting to Simulated Stellar Trails

6.1   Chapter Overview and Rationale

While fitting to simulated Gaussian stellar profiles has shown that significant improvements can be obtained over the Nyquist resolution limitation, this chapter aims to investigate the further potential gains by fitting to simulated stellar trails.

A stellar trail involves a line, generated by the star's motion across the sky, about which the seeing scatters the incoming light. The seeing can vary with time, so that both the stellar centroid and the FWHM of the stellar profile vary along the trail, which introduces great complexity into the modelling of a stellar trail. Having produced a model for the general star trail case, the approach adopted was to average the seeing along the stellar trail, producing an average seeing value over the CCD exposure time.

Simulations of stellar trails were used to investigate improvements over fitting to stellar profiles. As in chapter 5, the simulations were based on the Levenberg-Marquardt (LM) technique of non-linear least squares fitting. It was found that the project target for the measurement of seeing down to 1 arcsecond could be achieved using the ST-4 CCD camera. In addition, this target was found to set the absolute performance limitation for this camera.

6.2   Description of Stellar Trails

The imaging of stellar trails for the measurement of seeing was first introduced in Chapter 3. The system of Harlan & Walker (1965), which was based on the photographic imaging of stellar trails, provided a low cost technique for the measurement of seeing (see section 3.3.1). A series of Polaris star trails, captured by the system of Harlan & Walker (1965), were presented in Figure 3.2. This Figure clearly displayed the vertical jitter in the stellar centroid and the variations in trail thickness over time, both corresponding to variations in seeing. It was seen that worst seeing values corresponded to wider star trails with increased frequency in the vertical jitter.

The lower and upper stellar magnitude limits were calculated in section 4.3.2, where the lower stellar magnitude was found to be of critical importance when imaging stellar trails. The lower stellar magnitude limit referred to the brightest star that could be imaged without saturating the CCD pixels, and for the ST-4 CCD camera this was a 7.5 magnitude star. To prevent pixel saturation in stellar trail imaging it was identified as critical that the residency time (T_r), or time at which a star resides on a pixel, be less than the pixel saturation time. For the ST-4 a residency time of 75.6ms and a saturation time of 4.8s was calculated (see Appendix C, section C.2.2:"Length of Time Star remains in CCD FoV", "Residency Time" and "Saturation Time"). From Figure 4.6 it can be seen that a 7.5 magnitude star is very unlikely to appear in the field of view of the camera during the exposure time and that a magnitude 12 star is much more likely. Hence for a low-cost, non-tracking system saturation will not in general be a problem.

The average length of a star trail was needed in the modelling of stellar trails. The calculation of the average length of a star trail (N), measured in pixels, depends on the CCD exposure time. It has been assumed that our exposure time is limited to the length of time a star remains in the CCD field of view (FoV) (i.e. 14.5s for the ST-4). Based on this assumption, and an expected normal distribution of stars on the CCD plane, it is expected that on average a stellar trail will cover half the width of the CCD along the direction of imaging. For the ST-4 with an exposure time of 14.5s, and 192 pixels in the x-direction (i.e. assumed direction of imaging),

on average the length of each trail will be:

$$N = \frac{192}{2}$$

$$= 96 \text{ pixels}$$

6.3   Modelling of Stellar Trails

The modelling of stellar trails assumed that a stellar profile can be approximated by a two dimensional Gaussian function. Its general form was initially given by Equation 5.3 and has been purposefully reproduced in Equation 6.1 with variation in syntax and order of terms.

$$\mathrm{f}(x,y).dx.dy = \frac{\mathrm{a}}{2\pi\sigma^2}\exp\{-\frac{(y-y_0)^2 + (x-x_0)^2}{2\sigma^2}\}.dx.dy \tag{6.1}$$

where y and x define the plane of the CCD, y_0 and x_0 are the peak locations in the y and x directions respectively (i.e. stellar centroid), a is the total signal count where its calculation was based on the assumption that all light from a star falls on one pixel, $f(x,y)$ is the counts per unit area and σ is the standard deviation of the Gaussian stellar profile.

The modelling of stellar trails assumes that the trails are produced as straight lines, parallel to the x-axis only. This can be simply achieved by ensuring that the x-axis of the camera (i.e. that of the CCD) is in parallel with right ascension (RA) and away from the South Celestial Pole. Figure 6.1 represents an instant of a stellar trail as a single stellar profile centred at (x_0, y_0) on the CCD plane, which is travelling in the direction of the positive x-axis at a velocity of v. As the star travels (i.e. as the stellar trail is produced) the value of the seeing also changes. The trail has been selected between the start point of x_n at time t_n and end point of x_m at time t_m. End effects can be minimised by selecting only middle parts of the trail (3 seeing FWHMs from the ends should provide sufficient clearance).

In Figure 6.1 (x, y) represents a pixel at location (x, y). The total signal count at pixel (x, y)
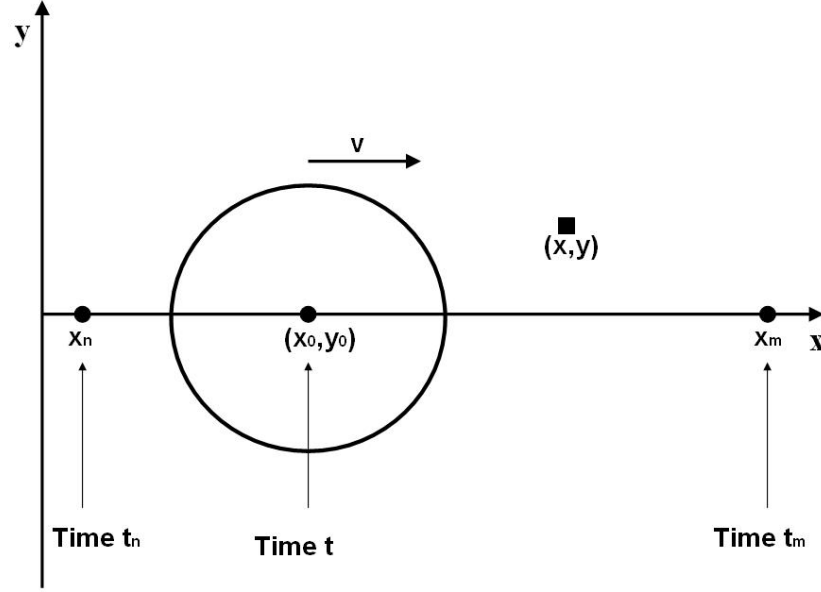
Figure 6.1: An instant of a stellar trail. The circle represents the stellar profile at time t on the CCD plane. The profile is travelling at speed v along the x-axis, hence producing a stellar trail. The stellar trail modelling initially calculates the total signal count contribution from the stellar trail at a single pixel with location (x, y).

from the star trail may be calculated by Equation 6.2.

$$F(x, y) = \int_{t=t_n}^{t=t_m} \frac{a}{2\pi\sigma(t)^2} \exp\{-\frac{(y - y_0(t))^2 + (x - (x_n + v(t - t_n)))^2}{2\sigma(t)^2}\} \cdot \frac{dt}{T_r} \qquad (6.2)$$

$y_0(t)$ represents the stellar centroid jitter (i.e. vertical jitter along the star trail) and is a function of time. $\sigma(t)$ represents the variation in the standard deviation of the Gaussian stellar profile along the trail (i.e. seeing variations over time) and is also a function of time. A conversion factor, T_r, has also been introduced. Since the signal count a was calculated over the residency time, T_r provides the conversion factor from signal count per residency time to signal count. The stellar centroid along the x-axis has been represented in terms of the selected trail start point (x_0), time of travel from the selected trail start point ($t - t_n$) and the velocity of the star along the CCD (v):

$$x_0 = x_n + v(t - t_n) \qquad (6.3)$$

From the expression for the total signal count at a single pixel (x, y), given by Equation 6.2, we now wish to calculate the sum of the signal contributions along each line of pixels defined by the equation $y = \mathrm{constant}$. This count will then be projected onto the y-axis (i.e. line of $x = 0$), producing a one-dimensional profile given by Equation 6.4 and in its expanded form by Equation 6.5 (see Figure 6.2).

$$\mathrm{F}(y) = \int_{x=x_n}^{x=x_m} F(x, y) . \frac{dx}{x_{pix}} \tag{6.4}$$

$$\mathrm{F}(y) = \int_{x=x_n}^{x=x_m} \int_{t=t_n}^{t=t_m} \frac{a}{2\pi\sigma(t)^2} \exp\{-\frac{(y - y_0(t))^2 + (x - (x_n + v(t - t_n)))^2}{2\sigma(t)^2}\} . \frac{dt}{T_r} . \frac{dx}{x_{pix}} \tag{6.5}$$

x_{pix} refers to the width of a pixel in the x-direction. The following three steps explain the need for this conversion factor:

1. Initially the integration is across a single pixel. The pixel begins at location x_i where i is the pixel index and ends at location $x_i + x_{pix}$.

$$\mathrm{F}(y) = \int_{x=x_i}^{x=x_i+x_{pix}} \int_{t=t_n}^{t=t_m} \frac{a}{2\pi\sigma(t)^2} \exp\{-\frac{(y - y_0(t))^2 + (x - (x_n + v(t - t_n)))^2}{2\sigma(t)^2}\} . \frac{dt}{T_r} . dx$$

2. Having assumed uniform intensity across one pixel, the integration can be evaluated as follows:

$$\mathrm{F}(y) = \int_{t=t_n}^{t=t_m} \frac{a}{2\pi\sigma(t)^2} \exp\{-\frac{(y - y_0(t))^2 + (x - (x_n + v(t - t_n)))^2}{2\sigma(t)^2}\} . \frac{dt}{T_r} \int_{x=x_i}^{x=x_i+x_{pix}} dx$$

$$= \int_{t=t_n}^{t=t_m} \frac{a}{2\pi\sigma(t)^2} \exp\{-\frac{(y - y_0(t))^2 + (x - (x_n + v(t - t_n)))^2}{2\sigma(t)^2}\} . \frac{dt}{T_r} \times x_{pix}$$

3. Hence to integrate over the stellar trail (i.e. many pixels) we require division by x_{pix}.

$$\mathrm{F}(y) = \int_{x=x_n}^{x=x_m} \int_{t=t_n}^{t=t_m} \frac{a}{2\pi\sigma(t)^2} \exp\{-\frac{(y - y_0(t))^2 + (x - (x_n + v(t - t_n)))^2}{2\sigma(t)^2}\} . \frac{dt}{T_r} . \frac{dx}{x_{pix}}$$

Finding an analytical solution to Equation 6.5 would prove troublesome, since as time progresses the standard deviation of each profile ($\sigma(t)$) and the stellar centroid jitter ($y_0(t)$) both also vary in time. Therefore for the modelling of a stellar trail a different approach was considered in an attempt to obtain an analytical solution for both varying seeing and jitter.
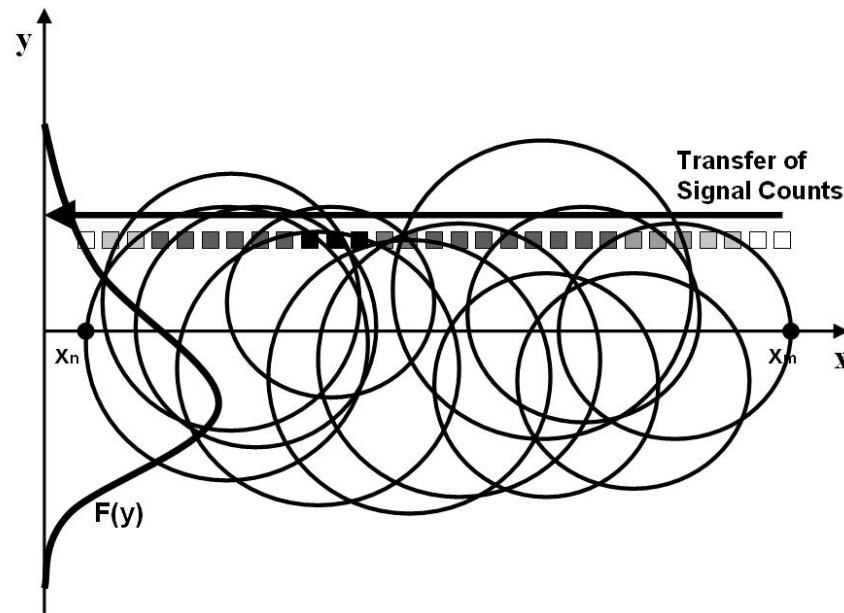
Figure 6.2: This Figure is a continuation of Figure 6.1. It shows a stellar trail which consists of a series of stellar profiles at each instant in time. The circles vary both in diameter and vertical position, representing variations in FWHM and vertical jitter (i.e. centroid motion) respectively. The second stage in the modelling of a stellar trail consists of summing the signal contributions along each line of pixels. Variations in the amount of signal per pixel have been represented with pixel colours ranging from white to black with a black coloured pixel representing the maximum intensity. $F(y)$ is the resulting profile obtained from projecting each line of pixels onto the y-axis.

For the purpose of modelling an averaged trail it was considered reasonable to fix the stellar centroid such that $y_0(t) = y_0 = \text{constant}$. We had previously calculated the signal contribution from the stellar trail at each pixel over time t, and projected the sum of signal counts along each line of pixels (i.e. given by $y = \text{constant}$) onto the y-axis, hence producing a one-dimensional profile defined by $F(y)$. An improved solution would be first to consider the contribution of one stellar profile at an instant in time. With this approach, the FWHM is constant such that $\sigma(t) = \sigma = \text{constant}$. The sum of the contributions of all pixels along each line at time t produces a Gaussian profile. This profile can then be projected onto the y-axis to produce a one-dimensional Gaussian profile, given by Equation 6.8. The final profile is the sum of all individual Gaussian profiles from each position of the stellar centroid.

Equation 6.6 defines the contribution of one stellar profile at time t. By ignoring the end

effects, it was possible to extend the limits of integration to $\pm\infty$.

$$\mathrm{G}(x,y) = \int_{x=\infty}^{x=-\infty} \frac{\mathrm{a}}{2\pi\sigma^2} \exp\{-\frac{(y-y_0)^2 + (x-(x_n+v(t-t_n)))^2}{2\sigma^2}\}.dx \qquad (6.6)$$

Using the definite integral given by Equation 6.7:

$$\int_{-\infty}^{\infty} e^{-(ax^2+bx+c)}.dx = \sqrt{\frac{\pi}{a}}e^{\frac{b^2-4ac}{4a}} \qquad (6.7)$$

Equation 6.6 can be evaluated, producing a one-dimensional Gaussian, given by Equation 6.8:

$$\mathrm{G}(y) = \frac{\mathrm{a}}{\sqrt{2\pi}\sigma} \exp\{-\frac{(y-y_0)^2}{2\sigma^2}\} + a_5 \qquad (6.8)$$

where a_5 is the pedestal voltage as described in chapter 5. The final profile is the sum of all the individual Gaussian profiles. However since the sum of two or more Gaussian profiles does not necessarily produce a Gaussian profile, no single equation can describe the sum of these Gaussian profiles. Hence for the modelling of a stellar profile it is also necessary to assume that the seeing is fixed. The following calculations demonstrate that the assumption of constant seeing during the 14.5s of stellar trail formation is a valid approximation such that the sum of N equal Gaussian profiles can be approximated by Equation 6.15, where N is the average length of a stellar trail.

Let the standard deviation (σ) be represented as the sum of its mean value (σ_0) and its variation about this value ($\Delta\sigma$):

$$\sigma = \sigma_0 + \Delta\sigma$$

$$= \sigma_0(1 + \frac{\Delta\sigma}{\sigma_0})$$

$$\frac{1}{\sigma} = (\sigma_0(1 + \frac{\Delta\sigma}{\sigma_0}))^{-1}$$

Also:

$$\sigma^2 = \sigma_0^2 + 2\sigma_0 \Delta\sigma + \Delta\sigma^2$$
$$= \sigma_0^2 (1 + \frac{2\Delta\sigma}{\sigma_0} + (\frac{\Delta\sigma}{\sigma_0})^2)$$

Therefore using the first two terms from the Taylor expansion of $\frac{1}{\sigma}$:

$$G(y) = \sum_{i=1}^{N} \frac{a(1 - \frac{\Delta\sigma}{\sigma_0})}{\sqrt{2\pi}\sigma_0} \exp\{-\frac{(y - y_0)^2}{2\sigma_0^2(1 + \frac{2\Delta\sigma}{\sigma_0} + (\frac{\Delta\sigma}{\sigma_0})^2)}\} \qquad (6.9)$$

where $(\frac{\Delta\sigma}{\sigma_0})^2$ becomes negligible if we consider $\Delta\sigma \ll \sigma$ for the short duration of a trail.

Using the first two terms from the Taylor expansion of σ^2:

$$G(y) = \sum_{i=1}^{N} \frac{a(1 - \frac{\Delta\sigma}{\sigma_0})}{\sqrt{2\pi}\sigma_0} \exp\{-\frac{(y - y_0)^2}{2\sigma_0^2}(1 - \frac{2\Delta\sigma}{\sigma_0})\} \qquad (6.10)$$

$$G(y) = \frac{a}{\sqrt{2\pi}\sigma_0} \exp\{-\frac{(y - y_0)^2}{2\sigma_0^2}\} \sum_{i=1}^{N} (1 - \frac{\Delta\sigma}{\sigma_0}) \exp\{\frac{(y - y_0)^2 \Delta\sigma}{\sigma_0^2 \sigma_0}\} \qquad (6.11)$$

Hence using the first two terms from the Taylor expansion of $\exp\{\frac{(y-y_0)^2 \Delta\sigma}{\sigma_0^2 \sigma_0}\}$ for y close to y_0:

$$G(y) = \frac{a}{\sqrt{2\pi}\sigma_0} \exp\{-\frac{(y - y_0)^2}{2\sigma_0^2}\} \sum_{i=1}^{N} (1 - \frac{\Delta\sigma}{\sigma_0})(1 + \frac{(y - y_0)^2 \Delta\sigma}{\sigma_0^2 \sigma_0}) \qquad (6.12)$$

$$G(y) = \frac{a}{\sqrt{2\pi}\sigma_0} \exp\{-\frac{(y - y_0)^2}{2\sigma_0^2}\} \sum_{i=1}^{N} 1 + \frac{\Delta\sigma}{\sigma_0}(\frac{(y - y_0)^2}{\sigma_0^2} - 1) - (\frac{\Delta\sigma}{\sigma_0})^2 (\frac{(y - y_0)^2}{\sigma_0^2})$$

$$(6.13)$$

The dominant term , $\frac{\Delta\sigma}{\sigma_0}(\frac{(y-y_0)^2}{\sigma_0^2} - 1)$, adds to zero in the summation as for every $+\Delta\sigma$ a $-\Delta\sigma$ will exist if σ is symmetrically distributed about σ_0. The final term in the summation may be neglected as $\Delta\sigma \ll \sigma$. Hence we have:

$$G(y) = \frac{a}{\sqrt{2\pi}\sigma_0} \exp\{-\frac{(y - y_0)^2}{2\sigma_0^2}\} \sum_{i=1}^{N} 1 \qquad (6.14)$$

showing that the assumption $\sigma = \sigma_0$ is a valid approximation for a short trail imaging duration of 14.5 seconds. Reinserting the pedestal voltage, a_5, we have the sum of N equal Gaussian profiles, given by:

$$G(y) = N \frac{a}{\sqrt{2\pi}\sigma} \exp\{-\frac{(y - y_0)^2}{2\sigma^2}\} + Na_5 \qquad (6.15)$$

Now that a model for star trails has been developed, the next section simulates and fits to these trails, in order to quantify the potential gains over stellar profile fitting.

6.4 Fitting to Simulated Stellar Trails

In this section averaged stellar trails, as described by Equation 6.15, will be simulated and then fitted to for the FWHM using the Levenberg-Marquardt technique (see section 5.3). The procedure is similar to that used in Chapter 5 for stellar profile fitting. The fitting is made in three parameters:

- a: signal count;

- σ: standard deviation of the Gaussian;

- a_5: CCD pedestal voltage.

Techniques for finding the position of the trail independently are readily available to astronomers. The partial derivative for each parameter was calculated as:

$$\frac{\partial G(y)}{\partial a} = N \frac{1}{\sqrt{2\pi}\sigma} \exp\{-\frac{(y - y_0)^2}{2\sigma^2}\} \qquad (6.16)$$

$$\frac{\partial G(y)}{\partial \sigma} = N \frac{a}{\sqrt{2\pi}\sigma^2} \exp\{-\frac{(y - y_0)^2}{2\sigma^2}\}(\frac{(y - y_0)^2}{\sigma^2} - 1) \qquad (6.17)$$

$$\frac{\partial G(y)}{\partial a_5} = N \qquad (6.18)$$

which have been used to define the Hessian Matrix. The simulations have been performed using the MATLAB function `cgaussianmodelfit`, described in section 5.6.2. Only minor modifications to `cgaussianmodelfit` and `afitfunc` were required in order to make use of the functions previously written for fitting to Gaussian stellar profile FWHMs and hence have not been reproduced. The most notable changes were:

1. the definition of the simulated noisy Gaussian profile in `cgaussianmodelfit` to that defined by Equation 6.15 with the addition of $\sqrt{N}$ Gaussian random noise per pixel[1];

2. the model Gaussian function ($ymod$) in `afitfunc`, to that defined by Equation 6.15;

3. the vector of derivatives ($dydx$) in `afitfunc`, to that defined by Equations 6.16 to 6.18.

With the implementation of these changes, what immediately became obvious was the effective gain obtained in the S/N equal to $\frac{N}{\sqrt{N}}$ or $\sqrt{N}$. Again, similar to stellar profile fitting, simulations were repeated 1000 times using the `manylm` MATLAB function. As will be shown in the next section, the mean value of the results was used to check for statistical bias while their standard deviation provided the expected standard error in the measurement of seeing. Simulations immediately reveal that the project specifications are achievable, that is the seeing can be measured down to 1 arcsecond using the ST-4 CCD camera. However no further gains were possible, with the project aim setting the absolute limit of performance of the ST-4 CCD camera.

6.5   Achievement of the Project Aim

The following case demonstrates the achievement of the project aim, which requires the measurement of seeing down to 1 arcsecond. The measurement of 1 arcsecond seeing, using the ST-4 CCD camera, as previously calculated, corresponds to a standard deviation of

---

[1]From statistical theory, $\sigma^2(\mu_N) = \frac{\sigma^2(x)}{N}$, where μ_N is the mean of N samples from a parent distribution with a variance $\sigma^2(x)$. Hence we have: $\sigma(\mu_N) = \frac{\sigma(x)}{\sqrt{N}}$, where σ is the standard deviation. The addition of N pixels of uncorrelated, Gaussian random noise, has a noise standard deviation given by: $\sigma(N\mu) = \frac{N\sigma}{\sqrt{N}} = \sqrt{N}\sigma$.

0.32 pixels. The ST-4 has a S/N of 12.9, equal to a signal count of 8.45. Figure 6.3 shows that the fitted σ values are centred about 0.3 pixels and lie within ± 0.05 pixels of this value. This distribution has a mean value of 0.3134 pixels and the SE(σ) equal to 0.0348 pixels, which is in agreement with Figure 6.3. The closeness of the mean of this distribution to the input mean of 0.32 pixels shows that the fitting procedure is statistically unbiased.
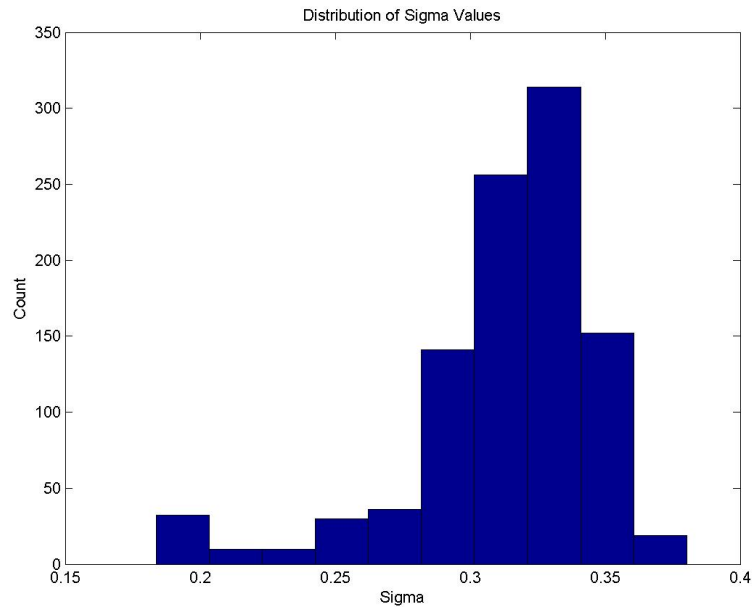
Figure 6.3: Case A - Distribution of the 1000 fitted sigma Values

Calculations in chapter 4, based on the Nyquist sampling criterion showed that the ST-4 camera does not provide sufficient resolution to allow the measurement of seeing down to 1 arcsecond. Here we have shown that with this technique, the ST-4 can indeed be used for this measurement.

To achieve this however an average seeing value is recorded every 14.5s, as opposed to instantaneous seeing values obtained in profile sampling. Such a sacrifice in time resolution (i.e. sampling rate) is considered appropriate for the application of site identification, where comparisons are made between sites, by making simultaneous measurements of seeing and instantaneous seeing is not of interest.

This case also demonstrates the boundary of performance of the ST-4 CCD camera based on the stellar-trail imaging technique, and hence its absolute performance limit, as simulations for resolutions below 0.32 pixels at the S/N of the ST-4 CCD camera have failed.

The results summarised in Table 6.1 show the progression from the conventional thinking to the achievement of the project aim.

Table 6.1: The Progression from Conventional Thinking to the Achievement of Project Target.

	Resolution (arcseconds)	Accuracy (arcseconds)
Project Target	*1*	*0.5*
Nyquist Criterion	3.1	–
Error Estimation Theory	2.5	0.14
Fitting Simulations	1.4	0.16
Trail Simulations	1	0.11

6.6   Chapter Summary

This chapter has successfully proven that stellar trail measurements provide significant gains, in resolving seeing, over measurements of the stellar profile. With these improvements the low cost measurement of astronomical seeing based on the stellar trail technique can just be performed with existing equipment down to 1 arcsecond and with an accuracy of 0.11 pixels.

While the achievement of the project target was based on a seeing value averaged over the exposure time (i.e. 14.5s for the ST-4), a sacrifice in time resolution has been considered as appropriate. This was due to the site identification application which requires simultaneous site measurements, where instantaneous seeing values are not of interest.

This chapter has concluded the final stage in the improvements obtained in resolvable seeing, and has therefore quantified the extent to which the application of Nyquist theorem to stellar profile sampling (i.e. conventional thinking on the limits of seeing measurement), can be exceeded. While the focus has been the ST-4 CCD camera in combination with the Meade-10 telescope, due to their availability, the developed techniques are widely applicable to the design of seeing measurement systems and the analysis of their data

Chapter 7

Conclusions and Further Work

This project has optimised the low cost measurement of astronomical seeing, achieving an accuracy better than 0.5 arcseconds, within the range of 1-10 arcseconds. Seeing is the parameter which at a given instant defines the lowest obtainable spatial resolution of astronomical objects through a telescope. It effectively quantifies the steadiness or lack of turbulence in the atmosphere. Therefore seeing is one of the most important factors in selecting a site for a new observatory and where this selection process requires comparisons between multiple sites, low cost seeing techniques make this process affordable.

A review of the fundamentals of optical astronomy, the first objective of this project, identified the importance of seeing measurements in site evaluation. From a study of the seeing measurement techniques and technologies, the measurement of the FWHM of the stellar profile obtained through stellar imaging or stellar trail imaging has been identified as the appropriate technique for low cost seeing measurement. Initial investigations, using the conventional application of Nyquist's theorem to stellar profile sampling, indicated that the available instrumentation could measure seeing only down to 3.1 arcseconds. This was well above the project specification of 1 arcsecond. After major work optimising the low cost technique and further extending it to the imaging of stellar trails, the project showed that the low cost instrumentation is capable of seeing measurements down to 1 arcsecond, thus meeting the project specification. These techniques constitute the original research outcome of this project. While the ST-4 CCD camera was used as a test bed, the techniques developed in this project are immediately applicable to all astronomical imaging systems.

7.1   Project Objectives and Method of Achievement

The following objectives have been addressed:

Research into the Fundamentals of Optical Astronomy and Site-Evaluation   Telescopes, both reflective and refractive, are the primary tools for optical astronomy. As the Earth's atmosphere (through seeing) and the optics used (through Dawes' limit) influence the obtainable image quality, an understanding of these factors was the first essential step in the development of a low cost seeing technique. Fundamental parameters of optical astronomy include f-ratio, plate scale, light gathering power, resolving power and magnification which were defined for later use in the evaluation of available instrumentation. Weather and climate, astronomical seeing, transparency and extinction and night sky radiation are all factors which influence the quality of ground based observations and hence are the deciding factors in the building of an observatory. A study on the location of the world's modern large telescopes shows that they effectively define the characteristics of an ideal site.

Analysis of Seeing Measurement Techniques and Technologies   Analysis of the past and present techniques and technologies used for the measurement of seeing identified the most suitable low cost method. This evaluation has amalgamated all past and present seeing practices within the three categories of visual, photographic and digital. The Pickering Seeing Scale, based on the appearance of the diffraction rings; and the Antoniadi Scale, based on the stellar jitter, form the two most widely used visual techniques. As the visual method is qualitative, its subjective nature provides inaccurate results, often varying between observers. The photography of star trails, based on the system of Harlan and Walker, was identified as a low cost analog technique for seeing measurements. The digital methods of seeing measurement were categorised into absolute and differential image motion monitors. While SBIG's All Weather Seeing Monitor provides a simple and low cost solution, its operation is limited to the Northern Hemisphere only. The Differential Image Motion Monitor, while providing the most accurate seeing measurements due to its differential nature, is complex and labour intensive and hence not suited for simultaneous seeing measurements at multiple sites. The measurement of the full width half maximum (FWHM) of the stellar profile obtained through stellar imaging or stellar trail imaging was found to be the appropriate technique in

terms of available equipment and the low cost criterion.

Evaluation of the Available Instrumentation for Low Cost Seeing Measurements   Both digital and photographic implementations of the low cost technique have been evaluated for the existing equipment. For the evaluation, three critical design factors were identified, namely field of view, signal to noise ratio and resolution. The field of view, in combination with the stellar density function, was found to determine the probability of capturing a star on the CCD plane during the exposure time. The limitations imposed by the small CCD size of the ST-4 and ST-6B CCD cameras could then be overcome by pointing closer to the galactic plane. The signal to noise ratio required the calculation of both the signal count and the noise count. This calculation was based on the ratio of the zero to peak amplitude of the Gaussian stellar profile to the standard deviation of the noise. Residency time and saturation time were considered critical, in particular for a stellar trail imaging system. Diffraction limited resolution, due to the optics of the available telescopes, was shown not to impose much limitation on the measurement of seeing down to 1 arcsecond. Overall the digital camera's shortcoming with respect to photographic film was due to its poor Nyquist resolution, which requires the FWHM of the stellar profile to cover 2.355 pixels. However, it was concluded that this resolution criterion does not set the absolute limitation, because, as it was shown, poorer resolution can be tolerated if the signal to noise ratio is increased. Hence, while the photographic implementation provided improved resolution and field of view, its extremely poor S/N and associated impracticalities (e.g. film changing, processing and scanning) were considered a significant detriment and a digital implementation was decided upon.

Optimisation of the Low Cost Seeing Measurement Technique   Initial investigations made use of IRIS astronomical image processing software which demonstrated that seeing can be measured with resolution below that of the Nyquist resolution for a noise free system. Through this process the dependency of the SE of seeing measurements on the fitting window became apparent. The nature of these dependencies was identified using error estimation theory, which also showed a moderate improvement over the Nyquist resolution. Error estimation for fitting with five parameters was initially implemented. However, to reduce the tendency of the Hessian matrix to become ill-conditioned, a decision was made to keep the stellar centroid fixed and perform the estimation of errors based on the remaining three

parameters only. With techniques for independently finding the stellar centroid, readily available to astronomers, this refinement was considered appropriate. The three parameter fitting successfully identified the dependence of SE of fitting parameters on S/N, fitting window and resolution. To examine actual error distributions from fitting to Gaussian stellar profiles, Levenberg-Marquardt non-linear least-squares fitting was performed on a large number of simulated profiles. From this it was shown that, using the ST-4, seeing measurements down to 1.4 arcseconds are possible – a major improvement over the Nyquist criterion. The study also identified the lowest S/N as a function of resolution for which the fitting is successful and the lowest useable resolution of 0.25 pixels, below which, independent of the S/N, the fitting failed at all times.

Improvements from Fitting to Simulated Stellar Trails   While fitting to simulated Gaussian stellar profiles provided significant improvements over the Nyquist resolution limitation, further gains were found to be possible by fitting to simulated stellar trails. With these improvements the measurement of seeing can just be performed with existing equipment down to 1 arcsecond and with an accuracy of 0.11 pixels. Due to the variations of seeing with time, the modelling of a stellar trail proved difficult. A model for the general star trail was produced which accounted for variations in both the location of the stellar centroid and the FWHM of the stellar profile along the stellar trail. As this model could not be evaluated analytically, the approach adopted was to average the seeing along the stellar trail, producing an average seeing value over the CCD exposure time. Simulations of stellar trails were used to investigate improvements over fitting to stellar profiles. It was found that the project target for the measurement of seeing down to 1 arcsecond could be achieved using the ST-4 CCD camera, and this target could also set the absolute performance limitation for this camera.

7.2   Further Work

The first step in applying the results of this research is the experimental testing of the theoretical findings. The system, consisting of the ST-4 CCD camera, Meade-10 telescope and a computer for processing the images, is to be set up at USQ's Mount Kent Observatory. Simultaneous readings are to be taken using both the low cost system and the newly installed

Celestron-20 0.5 metre , f/6.8 corrected Dall-Kirkham telescope. The C-20 telescope, in combination with its high resolution CCD cameras, allows immediately for the measurement of sub-arcsecond seeing, so that the accuracy of the measurements made using the low cost system can be evaluated. Depending on the outcome of the experiment, further testing can be performed in Western Queensland.

This project identified a major problem with fitting, in that for certain combinations of fitting parameters the non-linear least squares fitting resulted in singular Hessian matrices. This singularity issue may be bypassed by a technique called forward modelling. This technique makes use of the available high processing power of today's desktop computers. With forward modelling stellar profiles are continuously generated over the solution space. χ^2 is generated for each profile and the minimum χ^2 is found over the solution space. Hence problems with inverting the Hessian matrix are avoided. The implementation of this technique as part of the optimisation process may prove beneficial.

Assuming the experimental results confirm the theoretical findings, the long term goal would be the implementation of a remotely operated, partially autonomous low cost system. Techniques for the identification of stellar centroid position and trail location, both of which are readily available, need to be incorporated into a routine software package. The remotely operating system would consist of a data acquisition system, automated analysis package, CCD camera and an appropriate optical system, all within an environmental enclosure.

References

Allen, C. (1973), *Astrophysical Quantities*, third edn, The Altone Press, University of London at 4 Gower Street London.

Ashley, M., Burton, M., Lawrence, J. & Storey, J. (2004), 'Robotic telescopes on the antarctic plateau'.
http://www.phys.unsw.edu.au/~mcba/potsdam04.pdf.

Bennion, R. (2006), *The Stellar Profile*, Ewell Observatory.
http://www.ewellobservatory.com/bestpractices/player.html
current April 2006.

Borse, G. J. (1997), *Numerical Methods with MATLAB*, first edn, PWS Publishing Company, 102 Dodds Street, South Melbourne, 3205, Victoria, Australia.

Buil, C. (2006), *IRIS Version 5.31 Astronomical Imaging Software*, Christian Buil Homepage.
http://www.astrosurf.com/buil/us/iris/iris.htm
current May 2006.

Christensen, M. (2003), 'The importance of (not) being seen', *The Fox Valley Observer* pp. 4–6.

Coulman, C. (1986), 'The physics of seeing', *Identification, optimization and protection of optical telescope sites* pp. 2–12.

Dopita, M., Wood, P. & Hovey, G. (1996), 'An automated dimm telescope for antarctica', *Astronomical Society of Australia* pp. 39–43.

Hainaut, O. (1996), *Basic Image Processing*, European Southern Observatory.

`http://www.sc.eso.org/~ohainaut/ccd`
current April 2006.

Harlan, E. & Walker, M. (1965), 'A star-trail telescope for astronomical site-testing', *Astronomical Society of the Pacific* pp. 246–252.

Hecht, E. (2002), *Optics*, fourth edn, Addison-Wesley, 1301 Sansome St. San Francisco, CA 94111.

Hinds, D. (2004), *Schmidt-Cassegrain Telescope*, David Hinds Ltd Astronomy Supplies. `http://www.dhinds.co.uk/pages/catadioptric-telescopes.php` current March 2006.

Howell, S. (2000), *Handbook of CCD Astronomy*, first edn, Cambridge Univeristy Press, 10 Stamford Road, Oakleigh, Melbourne 3166, Australia.

Jenkins, J. W. C. (2003), *Practical Statistics for Astronomers*, first edn, Cambridge Univeristy Press, 10 Stamford Road, Oakleigh, Melbourne 3166, Australia.

Kea, M. (2006), *Why Mauna Kea is a Unique Site for Astronomy*, Mauna Kea Observatories. `http://www.ifa.hawaii.edu/mko/about_maunakea.htm` current March 2006.

Kutner, M. (2003), *Astronomy, A Physical Perspective*, second edn, Cambridge Universiy Press, 477 Williamstown Road, Port Melbourne, VIC 3207, Australia.

Meade (2006), *8″10″12″Schmidt-Cassegrain Design*, Meade Instruments Corporation. `http://www.meade.com/manuals/lx200/index.html` current April 2006.

Moller, P. (1996), *Astronomical Seeing Measurements Using a Differential Image Motion Monitor*, University of Southern Queensland.

Newsam, A. (2006), *Diffraction Limited Resolution*, Liverpool Johm Moores University. `http://www.astro.livjm.ac.uk/courses/phys134/scopes.html` current March 2006.

Ogata, K. (1995), *Discrete-Time Control Systems*, second edn, Prentice Hall, Upper Saddle River, New Jersy 07458.

OPT (2006), *SBIG - All Weather Seeing Monitor*, Oceanside Photo & Telescope.

http://www.optcorp.com/product.aspx?pid=319-1011-8218

current April 2006.

Peach, D. (2006), *The Pickering Seeing Scale*, Damian Peach.

http://uk.geocities.com/dpeach_78/pickering.htm

current March 2006.

Phtometrics (2006), *Dark Current*, Photometrics.

http://www.photomet.com/library_enc_dark.shtml

current April 2006.

Press, W. & Vetterling, W. (1992), *Numerical recipies in C*, 2nd edn, Cambridge University Press, 10 Stamford Rd, Oakleigh, Vic 3166.

Roussel, P. (1997), *40-inch Refracting Telescope*, Yerkes Observatory, University of Chicago.

http://astro.uchicago.edu/yerkes/virtualmuseum/40inch.html

current March 2006.

Sarazin, M. & Roddier, F. (1990), 'The eso differential image motion monitor', *European Southern Observatory* pp. 294–300.

SBIG (1996), *CCD Camera Operating Manual for the Model ST-4X, ST-5 and ST-6*, Santa Barbara Instrument Group.

http://www.sbig.com/sbwhtmls/softpage.htm

current April 2006.

SBIG (1999), *MODEL ST-4 CCD Star Tracker & Imaging Camera Operating Manual*, Santa Barbara Instrument Group.

http://www.sbig.com/sbwhtmls/softpage.htm

current April 2006.

SBIG (2000), *STV Video Camera and Autoguider Operating Manual*, Santa Barbara Instrument Group.

http://www.sbig.com/sbwhtmls/softpage.htm

current April 2006.

SBIG (2002*a*), *MODEL ST-4 CCD Star Tracker & Imaging Camera*, Santa Barbara Instrument Group.

`http://www.sbig.com/sbwhtmls/st4.htm`

current April 2006.

SBIG (2002*b*), *Model ST-6B CCD Imaging Camera*, Santa Barbara Instrument Group.

`http://www.sbig.com/sbwhtmls/st6b.htm`

current April 2006.

SBIG (2004), *MODEL ST-402ME CCD Imaging Camera*, Santa Barbara Instrument Group.

`http://www.sbig.com/sbwhtmls/online.htm`

current April 2006.

SBIG (2005), *All Weather Seeing Monitor*, Santa Barbara Instrument Group.

`http://www.sbig.com/sbwhtmls/online.htm`

current April 2006.

Wikipedia (2006), *Astronomical Seeing*, Wikipedia.

`http://en.wikipedia.org/wiki/Astronomical_seeing`

current March 2006.

Wood, P., Rodgers, A. & Russell, K. (1995), 'Seeing measurements at freeling heights and siding spring observatory', *Astronomical Society of Australia* pp. 97–105.

Zeilik, P. M. (1981), *Introductory Astronomy and Astrophysics*, second edn, CBS College Publishing, 210 West Washington Square Philadelphia, PA 19105.

Appendix A

Project Specification

University of Southern Queensland

FACULTY OF ENGINEERING AND SURVEYING

<u>ENG 4111/4112 Research Project</u>
PROJECT SPECIFICATION

FOR: **Ramin RAFIEI**

TOPIC: Optimisation of Low-Cost Astronomical Site Testing Techniques

SUPERVISOR: Associate Professor Nigel Hancock

ASSOCIATE SUPERVISORS: Dr Rhodes Hart and Dr Brad Carter

SPONSORSHIP: Faculty of Engineering and Surveying and

Faculty of Sciences

PROJECT AIM: This project aims to evaluate and optimise the low-cost measurement of astronomical seeing within the range of 1-10 arcseconds and to an accuracy of 0.5 arcseconds.

PROGRAMME: <u>**Issue C, 07 August 2006**</u>
(Re-drafted following major expansion of the work on item 4; hence deletion of previous item 6.)

1. Research information on optical astronomy, in particular its limitations. Identify the components of site-evaluation and the characteristics of a 'good astronomical site'.

2. Analyse past and present techniques and technologies used for the measurement of seeing and identify the best method to measure the seeing for a low-cost implementation.

3. Evaluate the suitability of the available equipment for a low-cost seeing measurement system which will measure the seeing within 1-10 arcseconds and to an accuracy of 0.5 arcseconds.

4. Investigate possible data-analysis techniques to overcome conventional limitations of low-cost seeing measurement techniques:

   a. Examine the sources of error in seeing measurement
   b. Find the conditions for optimum seeing determination

As time permits:

5. Explore related techniques (e.g. digitised stellar trails), that may yield further improvement in low cost seeing measurement.

AGREEED: _____ (Student) _____ (Principal Supervisor)

Date: _____

Appendix B

DIMM Wave Theory

B.1   Introduction

The theory of wavefronts and its relation to seeing values in the DIMM system was explained by Sarazin & Roddier (1990). They arrived at an expression which described the variances of the centroid dispersion in both the longitudinal and traverse directions, while taking into account the diameter of the sub-apertures and their separation. This theory has been included to develop an understanding of how the principles of the DIMM system and wave theory interrelate. The complete derivation which follows has been based on the general theory provided by Sarazin & Roddier (1990).

B.2   Derivation

The wavefront corrugation $z(x, y)$ is proportional to the wavefront phase error $\phi(x, y)$:

$$z(x, y) = \frac{\lambda}{2\pi} \phi(x, y) \tag{B.1}$$

Since light rays are normal to the wavefront surface, the component α of the angle-of-arrival fluctuation in the x direction is given by:

$$\alpha(x, y) = -\frac{\partial}{\partial x} z(x, y) = -\frac{\lambda}{2\pi} \frac{\partial}{\partial x} \phi(x, y) \tag{B.2}$$

The covariance of the angle-of-arrival fluctuation $B_\alpha(\xi, \eta)$, is given by:

$$B_\alpha(\xi, \eta) = < \alpha(x, y), \alpha(x + \xi, y + \eta) > \tag{B.3}$$

which is related to the covariance of the phase fluctuation, $B_\phi(\xi, \eta)$, by:

$$B_\alpha(\xi, \eta) = -\frac{\lambda^2}{4\pi^2} \frac{\partial^2}{\partial \xi^2} B_\phi(\xi, \eta). \tag{B.4}$$

From the phase structure function $D_\phi(\xi, \eta)$ which is defined as:

$$D_\phi(\xi, \eta) = 2[B_\phi(0,0) - B_\phi(\xi, \eta)] \tag{B.5}$$

by taking the following steps:

$$D_\phi(\xi, \eta) = 2B_\phi(0,0) - 2B_\phi(\xi, \eta)$$

$$B_\phi(\xi, \eta) = -\frac{1}{2}D_\phi(\xi, \eta) + B_\phi(0,0)$$

$$B_\alpha(\xi, \eta) = -\frac{\lambda^2}{4\pi^2}\frac{\partial^2}{\partial \xi^2}[-\frac{1}{2}D_\phi(\xi, \eta) + B_\phi(0,0)]$$

$$= \frac{\lambda^2}{8\pi^2}\frac{\partial^2}{\partial \xi^2}D_\phi(\xi, \eta)$$

we can arrive at:

$$B_\alpha(\xi, \eta) = \frac{\lambda^2}{8\pi^2}\frac{\partial^2}{\partial \xi^2}D_\phi(\xi, \eta). \tag{B.6}$$

For Kolmogorov turbulence at the near-field approximation, the phase structure function is given by (refer to Coulman (1986) for a more detailed explanation):

$$D_\phi(\xi, \eta) = 6.88(\frac{r}{r_0})^{5/3} \tag{B.7}$$

where $r = \sqrt{\xi^2 + \eta^2}$ and r_0 is Fried's seeing parameter. Substituting Equation B.7 into B.6:

$$B_\alpha(\xi, \eta) = \frac{\lambda^2}{8\pi^2} \frac{\partial^2}{\partial \xi^2} [6.88(\frac{r}{r_0})^{5/3}]$$

$$= 6.88 \frac{\lambda^2}{8\pi^2} r_0^{-5/3} \frac{\partial^2}{\partial \xi^2} [\sqrt{\xi^2 + \eta^2}]^{5/3}$$

$$= 0.087\lambda^2 r_0^{-5/3} \frac{\partial^2}{\partial \xi^2} [\xi^2 + \eta^2]^{5/6}$$

$$= 0.087\lambda^2 r_0^{-5/3} \frac{\partial}{\partial \xi} [2\xi \frac{5}{6} (\xi^2 + \eta^2)^{-1/6}]$$

$$= 0.145\lambda^2 r_0^{-5/3} [\frac{\partial}{\partial \xi} \xi \times (\xi^2 + \eta^2)^{-1/6} + \xi \times \frac{\partial}{\partial \xi} (\xi^2 + \eta^2)^{-1/6}]$$

$$= 0.145\lambda^2 r_0^{-5/3} [(\xi^2 + \eta^2)^{-1/6} + \xi \times 2\xi \times -\frac{1}{6} (\xi^2 + \eta^2)^{-7/6}]$$

$$= 0.145\lambda^2 r_0^{-5/3} [(\xi^2 + \eta^2)^{-1/6} - \frac{1}{3}\xi^2 (\xi^2 + \eta^2)^{-7/6}]$$

hence arriving at the following equation:

$$B_\alpha(\xi, \eta) = 0.145\lambda^2 r_0^{-5/3} [(\xi^2 + \eta^2)^{-1/6} - \frac{1}{3}\xi^2 (\xi^2 + \eta^2)^{-7/6}]. \tag{B.8}$$

Substituting for $\eta = 0$ into Equation B.8, we arrive at the longitudinal covariance $B_l(d)$ as a function of the separation $\xi = d$:

$$B_\alpha(\xi, \eta) = 0.145\lambda^2 r_0^{-5/3} [(\xi^2 + \eta^2)^{-1/6} - \frac{1}{3}\xi^2 (\xi^2 + \eta^2)^{-7/6}]$$

$$B_\alpha(d, 0) = 0.145\lambda^2 r_0^{-5/3} [(d^2)^{-1/6} - \frac{1}{3}d^2 (d^2)^{-7/6}]$$

$$= 0.145\lambda^2 r_0^{-5/3} [d^{-1/3} - \frac{1}{3}d^2 d^{-14/6}]$$

$$= 0.145\lambda^2 r_0^{-5/3} d^{-1/3} - \frac{0.145}{3}\lambda^2 r_0^{-5/3} d^{-1/3}$$

$$= 0.097\lambda^2 r_0^{-5/3} d^{-1/3}$$

$$= 0.097(\frac{\lambda}{r_0})^{5/3} (\frac{\lambda}{d})^{1/3}.$$

$$B_l(d) = B_\alpha(d, 0) = 0.097(\frac{\lambda}{r_0})^{5/3} (\frac{\lambda}{d})^{1/3} \tag{B.9}$$

Substituting for $\xi = 0$ into Equation B.8 , we arrive at the transverse covariance $B_t(d)$ as a function of the separation $\eta = d$:

$$B_\alpha(\xi, \eta) = 0.145\lambda^2 r_0^{-5/3}[(\xi^2 + \eta^2)^{-1/6} - \frac{1}{3}\xi^2(\xi^2 + \eta^2)^{-7/6}]$$

$$B_\alpha(0, d) = 0.145\lambda^2 r_0^{-5/3} d^{-1/3}$$

$$= 0.145(\frac{\lambda}{r_0})^{5/3}(\frac{\lambda}{d})^{1/3}$$

$$B_t(d) = B_\alpha(0, d) = 0.145(\frac{\lambda}{r_0})^{5/3}(\frac{\lambda}{d})^{1/3} \tag{B.10}$$

It can be seen that the transverse covariance is 1.5 times larger than the longitudinal covariance and both decrease as the -1/3 power of the separation. The value at the origin $B_\alpha(0, 0)$ which is limited by aperture averaging was given by the expression for the variance of image motion derived by Fried (Coulman 1986) as:

$$B_\alpha(0, 0) = 0.179(\frac{\lambda}{r_0})^{5/3}(\frac{\lambda}{D})^{1/3} \tag{B.11}$$

where D is the diameter of the sub-apertures through which the tilts are measured. The variance of the differential image motion, $\sigma^2(d)$, observed over a distance d is given by:

$$\sigma^2(d) = 2[B(0) - B(d)]. \tag{B.12}$$

For $d \geq 2D$ and substituting Equations B.9 and B.11 into B.12 we arrive at an approximate expression for the variance of the differential longitudinal motion (σ_l^2):

$$\sigma_l^2 = 2[0.179(\frac{\lambda}{r_0})^{5/3}(\frac{\lambda}{D})^{1/3} - 0.097(\frac{\lambda}{r_0})^{5/3}(\frac{\lambda}{d})^{1/3}]$$

$$= 2\lambda^2 r_0^{-5/3}[0.179D^{-1/3} - 0.0968d^{-1/3}].$$

$$\sigma_l^2 = 2\lambda^2 r_0^{-5/3}[0.179D^{-1/3} - 0.0968d^{-1/3}] \tag{B.13}$$

For $d \geq 2D$ and substituting Equations B.10 and B.11 into B.12 we arrive at an approximate expression for the variance of the differential transverse motion (σ_t^2):

$$\sigma_t^2 = 2[0.179(\frac{\lambda}{r_0})^{5/3}(\frac{\lambda}{D})^{1/3} - 0.145(\frac{\lambda}{r_0})^{5/3}(\frac{\lambda}{d})^{1/3}]$$
$$= 2\lambda^2 r_0^{-5/3}[0.179D^{-1/3} - 0.145d^{-1/3}].$$

$$\sigma_t^2 = 2\lambda^2 r_0^{-5/3}[0.179D^{-1/3} - 0.145d^{-1/3}] \tag{B.14}$$

We have therefore arrived at expressions which describe the variances of the centroid dispersion in both the longitudinal and traverse directions.

Appendix C

Sample Calculations using the ST-4 and 10″ Meade LX200 f/10

C.1   Introduction

The following calculations have been made in order to investigate the suitability of the ST-4, 10″ Meade f/10 camera-telescope combination for the measurement of astronomical seeing. These calculations assume a worst case design. The ST-6 and 10″ Meade calculations follow a similar procedure, and as a result the working has not been included. A summary of the results has been included in Table 4.3.

C.2   Calculations

Table 4.1 provides a summary of the ST-4 specifications which have been used to perform the following calculations. These calculations have been placed in the same order as which they are referred to in Chapter 4.

C.2.1   Field of View and Stellar Density Function

The following calculations correspond to section 4.3.1.

Plate Scale

The plate scale of the telescope has been calculated using Equation 2.4.

$$
\begin{aligned}
f &= 2500\text{mm} \\
s &= \frac{\pi}{180} \times 2500 \\
&= 43.63 \text{ mm.degree}^{-1} \\
&= \frac{43.63 \times 10^3}{3600} \\
&= 12.12 \ \mu\text{m.arcsecond}^{-1}
\end{aligned}
$$

Field of View

The calculation for field of view required the calculation of the pixel resolution.

$$\text{pixel size} = 13.75 \times 16\mu\text{m}$$
$$\text{resolution} = \frac{16}{12.12}$$
$$= 1.32 \text{ arcseconds.pixel}^{-1}$$

The Field of View (FoV) could hence be determined with knowledge of the size of the ST-4 pixel array.

$$\text{pixel array} = 192 \times 164\text{pixels}$$
$$\text{FoV} = 164 \times 1.32$$
$$= 216.5 \text{ arcseconds}$$

12 and 14 Magnitude Star Count per FoV

The calculation for the number of stars brighter than magnitude 12 (N_{12}) and 14 (N_{14}), in the ST-4 FoV required knowledge of the star count, obtained from Figure 4.6. The star counts were taken at 90 degrees to the galactic plane. This calculation required knowledge of the FoV in both X and Y directions.

$$\text{FoV}_Y = 216.5 \text{ arcseconds}$$
$$\text{FoV}_X = 192 \times \frac{13.75}{12.12}$$
$$= 217.8 \text{ arcseconds}$$

$$N_{12} = 21.4 \text{ stars.degree}^{-2}$$

$$N = 21.4 \times \frac{216.5}{3600} \times \frac{217.8}{3600}$$

$$= 0.078 \text{ stars.FoV}^{-1}$$

$$N_{14} = 102.3 \text{ stars.degree}^{-2}$$

$$N = 102.3 \times \frac{216.5}{3600} \times \frac{217.8}{3600}$$

$$= 0.372 \text{ stars.FoV}^{-1}$$

C.2.2 Signal to Noise Ratio

The following calculations correspond to section 4.3.2.

Length of Time Star remains in CCD FoV

In calculating the length of time (t) a star remains in the FoV, a sidereal day was assumed to equal a solar day.

$$\text{rate of travel} = \frac{360}{24}$$

$$= 15 \text{ degrees.hr}^{-1}$$

$$= \frac{15 \times 3600}{3600}$$

$$= 15 \text{ arcseconds.s}^{-1}$$

$$t = \frac{216.5}{15}$$

$$= 14.5 \text{ s}$$

Residency Time

The residency time per pixel was obtained using the length of time a star remained in the ST-4 FoV and its array size.

$$\text{residency time} = \frac{14.5}{192}$$

$$= 75.6 \text{ ms}$$

Saturation Time

The calculation for saturation time required knowledge of the Full Well Capacity of an ST-4 pixel. A residency time larger than the saturation time will cause pixels to saturate. A saturated pixel does not contain its true value.

$$\text{Full Well Capacity} = 80000\text{e}^-$$

$$\text{saturation time} = \frac{80000}{16762}$$

$$= 4.8 \text{ s}$$

Star Flux

The flux from a target star of visual magnitude 12 has been calculated using Equation 4.7.

$$\log F = (-0.4 \times 12) - 8.43$$

$$= -13.23$$

$$\therefore F = 10^{-13.23}$$

$$= 5.888 \times 10^{-14} \text{ erg.cm}^{-2}.\text{Å}^{-1}.\text{s}^{-1}$$

$$= 5.888 \times 10^{-21} \text{ J.cm}^{-2}.\text{Å}^{-1}.\text{s}^{-1}$$

$$= 5.888 \times 10^{-17} \text{ W.m}^{-2}.\text{Å}^{-1}$$

$$= 5.888 \times 10^{-17} \times 3000$$

$$= 1.766 \times 10^{-13} \text{ W.m}^{-2}$$

Electrons per Pixel

The calculation for the number of electrons per pixel assumes perfect seeing such that the light from a star falls on one pixel only. The average Quantum Efficiency (QE), over the 300nm window, has been extracted from the CCD data sheet and the area of the telescope (A) refers to the area of the primary mirror. The definition for current (I) has been used to obtain the electron counts.

$$\text{A} = \frac{\pi}{4} \times 0.254^2$$

$$= 0.051 \text{m}^2$$

$$\text{F} = 0.051 \times 1.766 \times 10^{-13}$$

$$= 9.01 \times 10^{-15} \text{ W.pixel}^{-1}$$

$$\text{QE} = 0.3 \text{ A.W}^{-1}$$

$$\text{I} = 9.01 \times 10^{-15} \times 0.3$$

$$= 2.702 \times 10^{-15} \text{ A.pixel}^{-1}$$

$$= 2.702 \times 10^{-15} \text{ C.s}^{-1}.\text{pixel}^{-1}$$

$$\text{electrons per pixel} = \frac{2.70 \times 10^{-15}}{1.6 \times 10^{-19}}$$

$$= 16762 \text{ e}^{-}\text{s}^{-1}$$

Signal Count

To calculate the signal count initially the electron count over the residence time had to be calculated.

$$\text{electron count} = 75.6 \times 10^{-3} \times 16762$$

$$= 1267 \text{ e}^-.\text{pixel}^{-1}$$

$$\text{Gain} = 150 \text{ e}^-.\text{ADU}^{-1}$$

$$\text{signal count} = \frac{1267}{150}$$

$$= 8.45 \text{ ADU}$$

Noise Count

The calculation of noise count required knowledge of the read noise and dark current. Equation 4.1 has been used to calculate the rms dark current noise and Equation 4.2 has been used to arrive at the total noise in electrons. The A/D gain has been used to obtain the noise count.

$$\text{Read Noise}_{rms} = 150 \text{ e}^-.\text{pixel}^{-1}$$

$$\text{Dark Current} = 250 \text{ e}^-.\text{pixel}^{-1}.\text{s}^{-1}$$

$$= 250 \times 75.6 \times 10^{-3}$$

$$= 18.9 \text{e}^-.\text{pixel}^{-1}$$

$$\text{Dark Current Noise}_{rms} = \sqrt{18.9}$$

$$= 4.35 \text{ e}^-.\text{pixel}^{-1}$$

$$\text{Total Noise} = \sqrt{150^2 + 4.35^2}$$

$$= 150 \text{ e}^-.\text{pixel}^{-1}$$

$$\text{noise count} = \frac{150}{150}$$

$$= 1.00 \text{ ADU}$$

Ratio of Signal to Noise

The signal to noise ratio can be obtained using Equation 4.4, which calls on Equations 4.5 and 4.6. The resolution of the ST-4 is 1.32 arcseconds per pixel which corresponds to a FWHM (measured in pixels) of:

$$\text{FWHM} = \frac{1}{1.32}$$
$$= 0.75 \text{ pixels}$$

Hence the S/N obtained on the ST-4 from a magnitude 12 target star is calculated as follows:

$$\sigma = \frac{\text{FWHM}}{2.355}$$
$$\sigma = \frac{0.75}{2.355}$$
$$= 0.32 \text{ pixels}$$
$$a_0 = \frac{a}{2\pi\sigma^2}$$
$$a_0 = \frac{8.45}{2\pi \times 0.32^2}$$
$$= 12.9$$
$$\text{S/N} = \frac{a0}{\sigma_{noise}}$$
$$\text{S/N} = \frac{12.9}{1}$$
$$= 12.9$$

Signal Count for a Magnitude 14 Star

The signal count for a 14 magnitude target star could simply be obtained by calculating the flux ratio between the 12 and 14 magnitude stars and hence dividing the signal count for the 12 magnitude star by the flux ratio.

$$\log F = -0.4m_v - 8.43$$

$$\log F_{12} = (-0.4 \times 12) - 8.43$$

$$\log F_{14} = (-0.4 \times 14) - 8.43$$

$$\log F_{12} - \log F_{14} = 0.8$$

$$\frac{F_{12}}{F_{14}} = 6.3$$

$$\text{signal count} = \frac{8.45}{6.3}$$

$$= 1.3$$

C.2.3 Resolution

The following calculation corresponds to section 4.3.3.

Detector Resolution

The calculation for the CCD resolution required knowledge of the size of a ST-4 pixel and the plate scale of the telescope.

$$\text{pixel size} = 13.75 \times 16\mu\text{m}$$

$$\text{resolution} = \frac{16}{12.12}$$

$$= 1.32 \text{ arcseconds.pixel}^{-1}$$

Appendix D

MATLAB Source Code

D.1   Introduction

This Appendix contains the complete MATLAB source code used for the implementation of this project. The raw code was provided as a package for the completion of this project by project co-supervisor Dr. Rhodes Hart. Debugging, application and documentation was performed by the candidate as part of the project.

D.2   The `circgauss` MATLAB Function

The MATLAB function `circgauss` generates a stellar profile based on a Gaussian distribution, given by Equation 5.3. The function also returns the peak amplitude of the stellar profile given by Equation 5.4.

```
% Function:     circgauss
% Purpose       To generate a stellar profile based in the
%               Gaussian distribution
% Syntax:       [n,a0] = circgauss(x,y,a,b,amp,sigma,noise)
% Input:        x and y = equal length vectors of
%               pixel positions
%               a and b = define the stellar centroid on the
%               CCD plane for x and y respectively
%               amp = total signal count [ADU]
%               sigma = standard deviation of the stellar
%               profile
%               noise = noise count [ADU]
% Output:       n = matrix containing the stellar profile
%               a0 = peak amplitude of the stellar profile


function [n,a0] = circgauss(x,y,a,b,amp,sigma,noise)



% Transform the domain specified by vectors x and y into
```

```
% arrays xx and yy

[xx,yy] = meshgrid(x,y);


% Generate the stellar profile based on a Gaussian distribution

n = amp*exp(-((xx-a).^2 +(yy-b).^2)/(2*sigma^2))/(2*pi*sigma^2);


% Include the effect of random normal noise

n = n + noise*randn(size(xx));


% Calculate the peak amplitude of the stellar profile

a0 = amp/(2*pi*sigma^2);


% Plot the stellar profile

surf(n)


title('A Stellar Profile based on the Gaussian Distribution of the
PSF')


xlabel('xx (pixels)')


ylabel('yy (pixels)')


zlabel('f(xx,yy)(signal count per pixel)')
```

D.3   The `cgfiterr` MATLAB Function

The MATLAB function `cgfiterr` calculates the standard error of the five fitting parameters based on the LM theory of error estimation. The `cgfiterr` function calculates the Hessian Matrix as given by Equation 5.10 using the partial derivatives defined by Equations 5.17 through to 5.21. The Hessian Matrix is then used to calculate the covariance matrix which was defined as its inverse (see Equation 5.9). The standard errors in the measurement of the fitting parameters are the square-root of the diagonal terms of the covariance matrix, given by

Equation 5.12. The `cgfiterr` function also returns the maximum correlation between the fitted parameters as the above interpretation of the covariance matrix holds only if the fitted parameters are uncorrelated (see Equation 5.14). The `cgfiterr` function also calculates the 'condition number' of the Hessian Matrix using Singular Value Decomposition (SVD) in order to indicate the trustworthiness of the results.

```
% Function:      cgfiterr.m
% Purpose:       To calculate the standard error of the
%                five fitting parameters based on the
%                LM theory of error estimation.
% Syntax:        [sde,cor,cov] = cgfiterr(amp,sig,const,pixfact)
% Input:         amp = signal count
%                sig = standard deviation of the Gaussian profile
%                const = pedestal voltage
%                pixfact = number of standard deviations arcoss the
%                fitting window
% Output:        sde = standard error of fitting parameters
%                cor = correlation between fitted parameters
%                cov = covariance matrix


function  [sde,cor,cov] = cgfiterr(amp,sig,const,pixfact)



% Assign the inputs to the parameters
a1 = amp;


a2 = sig;


a5 = const;


% Calculate number of pixels across
npix = round(pixfact*a2) + 1;
```

```
% Ensure fitting area covers odd number of pixels so that
% the distibution is at the centre of a pixel

if (rem(npix,2)==0) npix = npix + 1; end

% Place centre of distibution slightly off-centre
% (needed for stability of inverse)

ctr = round(mean([1 npix]));

a3 = ctr+ .00001;

a4 = ctr+ .00001;

% Generate mesh and turn into columns
vec = 1:npix;

[x1array,x2array] = meshgrid(vec,vec);

x1 = x1array(:);

x2 = x2array(:);

% Calculate the partial derivatives
delx1 = (x1-a3);

delx12 = delx1.^2;

delx2 = (x2-a4);

delx22 = delx2.^2;

sqs = delx12 + delx22;
```

```
e = exp( -sqs/(2*a2^2));


t1 = 1/(2*pi*a2^2);


t2 = a1*t1; t3 = t2*e;


% Define the partial derivatives


da1 = t1*e;


da2 = t3.*(-2/a2 +sqs/a2^3);


da3 = t3.*delx1/a2^2;


da4 = t3.*delx2/a2^2;


da5 = ones(size(x1));


% Calculate the entries to the Hessian Matrix
a11 = sum(da1)^2;


a12 = sum(da1.*da2);


a13 = sum(da1.*da3);


a14 = sum(da1.*da4);


a15 = sum(da1.*da5);


a21 = a12;


a22 = sum(da2)^2;
```

```
a23 = sum(da2.*da3);


a24 = sum(da2.*da4);


a25 = sum(da2.*da5);


a31 = a13;


a32 = a23;


a33 = sum(da3)^2;


a34 = sum(da3.*da4);


a35 = sum(da3.*da5);


a41 = a14;


a42 = a24;


a43 = a34;


a44 = sum(da4)^2;


a45 = sum(da4.*da5);


a51 = a15;


a52 = a25;


a53 = a35;
```

```
a54 = a45;


a55 = sum(da5)^2;


% Define the Hessian Matrix
alpha = [a11 a12 a13 a14 a15; ...
         a21 a22 a23 a24 a25; ...
         a31 a32 a33 a34 a35; ...
         a41 a42 a43 a44 a45; ...
         a51 a52 a53 a54 a55];


% Calcualte the covariance matrix
cm = inv(alpha);


% Calcualte the standard errors in the fitted parameters
sde = sqrt(diag(cm));


% Calculate the correlation
cor = cm;


for i = 1:5
  for j = 1:5
     cor(i,j) = cor(i,j)/(sde(i)*sde(j));
  end
end


% Display the number of pixels used for the fitting
% and the height of the stellar profile (i.e. signal
% to noise ratio for noise=1)
fprintf('NPix = %d  Height = %10.3f\n',npix, t2);


% Display the standard errors of the fitted parameters
fprintf('SE in fitted parameters a1,a2,a3,a4,a5 = ');
```

```
fprintf('%10.3e   ',sde); fprintf('\n');


% Calculate and display the maximum correlation between

% the fitted parameters

fprintf('Max correlation = %5.2f percent\n',

max(max(abs(cor-eye(5))))*100);


% Return the vector s containing the singular values

[u,s,v] = svd(alpha);


% Calcualte the condition number

d = diag(s)'; cond = max(d)/min(d);


% Exceeding condition > 10^16 will produce a singular

% matrix (IEEE 64-bit floating point format)

fprintf('Condition = %10.3e\n',cond);
```

D.4   The `cgfiterrfixedcentre` MATLAB Function

The MATLAB function `cgfiterrfixedcentre` calculates the standard error of the three fitting parameters based on the LM theory of error estimation. The `cgfiterrfixedcentre` function follows a similar algorithm to that of `cgfiterr` but for a fixed stellar centroid.

```
% Function:     cgfiterr.m

% Purpose:      To calculate the standard error of the

%               three fitting parameters based on the

%               LM theory of error estimation.

% Syntax:       [sde,cor,cov] = cgfiterr(amp,sig,const,pixfact)

% Input:        amp = signal count

%               sig = standard deviation of the Gaussian profile

%               const = pedestal voltage
```

```
%              pixfact = number of standard deviations arcoss the
%              fitting window
% Output:      sde = standard error of fitting parameters
%              cor = correlation between fitted parameters
%              cov = covariance matrix


function  [sde,cor,cov] =
cgfiterrfixedcentre(amp,sig,const,pixfact)



% Assign the inputs to the parameters
a1 = amp;


a2 = sig;


a5 = const;


% Calculate number of pixels across
npix = round(pixfact*a2) + 1;


% Ensure fitting area covers odd number of pixels so that
% the distibution is at the centre of a pixel
if (rem(npix,2)==0) npix = npix + 1; end


% Place centre of distibution slightly off-centre
% (needed for stability of inverse)
ctr = round(mean([1 npix]));


a3 = ctr+ .00001;


a4 = ctr+ .00001;


% Generate mesh and turn into columns
```

```matlab
vec = 1:npix;


[x1array,x2array] = meshgrid(vec,vec);


x1 = x1array(:);


x2 = x2array(:);


% Calculate the partial derivatives
delx1 = (x1-a3);


delx12 = delx1.^2;


delx2 = (x2-a4);


delx22 = delx2.^2;


sqs = delx12 + delx22;


e = exp( -sqs/(2*a2^2));


t1 = 1/(2*pi*a2^2);


t2 = a1*t1;


t3 = t2*e;


% Define the partial derivatives
da1 = t1*e;


da2 = t3.*(-2/a2 +sqs/a2^3);


da3 = t3.*delx1/a2^2;
```

```
da4 = t3.*delx2/a2^2;


da5 = ones(size(x1));


% Calculate the entries to the Hessian Matrix
a11 = sum(da1)^2;


a12 = sum(da1.*da2);


a13 = sum(da1.*da3);


a14 = sum(da1.*da4);


a15 = sum(da1.*da5);


a21 = a12;


a22 = sum(da2)^2;


a23 = sum(da2.*da3);


a24 = sum(da2.*da4);


a25 = sum(da2.*da5);


a31 = a13;


a32 = a23;


a33 = sum(da3)^2;


a34 = sum(da3.*da4);
```

```matlab
a35 = sum(da3.*da5);

a41 = a14;

a42 = a24;

a43 = a34;

a44 = sum(da4)^2;

a45 = sum(da4.*da5);

a51 = a15;

a52 = a25;

a53 = a35;

a54 = a45;

a55 = sum(da5)^2;

% Define the Hessian Matrix
alpha = [a11 a12 a15; ...
         a21 a22 a25; ...
         a51 a52 a55];

% Calcualte the covariance matrix
cm = inv(alpha);

% Calcualte the standard errors in the fitted parameters
sde = sqrt(diag(cm));
```

```matlab
% Calculate the correlation
cor = cm;

for i = 1:3
   for j = 1:3
      cor(i,j) = cor(i,j)/(sde(i)*sde(j));
   end
end

% Display the number of pixels used for the fitting
% and the height of the stellar profile
% (i.e. signal to noise ratio for noise=1)
fprintf('NPix = %d  Height = %10.3f\n',npix, t2);

% Display the standard errors of the fitted parameters
fprintf('SE in fitted parameters a1,a2,a5 = ');
fprintf('%10.3e   ',sde); fprintf('\n');

% Calculate and display the maximum correlation
% between the fitted parameters
fprintf('Max correlation = %5.2f percent\n',
max(max(abs(cor-eye(3))))*100);

% Return the vector s containing the singular values
[u,s,v]= svd(alpha);

% Calcualte the condition number
d = diag(s)'; cond = max(d)/min(d);

% Exceeding condition > 10^16 will produce a
% singular matrix (IEEE 64-bit% floating point format)
fprintf('Condition = %10.3e\n',cond)
```

D.5   The `cgaussianmodelfit` MATLAB Function

The MATLAB function `cgaussianmodelfit` performs the simulation. In doing so it calls

on the function `lmnlsqfit` (see section D.6) which performs a fitting to a non-linear

function using the Levenberg-Maquardt non-linear least squares technique.


```
% Function:      cgaussianmodelfit.m
% Purpose:       To simulate a circular Gaussian and fit using
%                the LM technique.
% Syntax:
% cgaussianmodelfit(npix, a, aguess, ause, noisesd, endcond,pstep)
% Input:         npix = size of the fitting window (both x and y)
%                a = [amp sd x10 x20 const] is the parameter vector:
%                   amp = signal count
%                   (i.e. area under the Gaussian distribution)
%                   sd = standard deviation of the Gaussian profile
%                   x10 and x20 = stellar centroid on the CCD plane
%                   const = pedestal voltage
%                aguess = vector of initially guessed parameters
%                ause = vector defining the number of parameters
%                to fit for (e.g. for a 3 parameter fitting
%                ause=[1 1 0 0 1])
%                noisesd = standard deviation of the noise
%                endcond = condition at which to stop the
%                iterations (i.e. when the fractional change
%                in chi-squared is less than the end condition
%                value set, Press (1992) recommends endcond=0.001)
%                pstep = if set to 1 program will step
%                through each iteration.
% Output:        a2 = the modelled standard deviation of the
%                Gaussian Profile


function a2 = cgaussianmodelfit(npix, a, aguess, ause, noisesd,
```

```
endcond,pstep)



% If pstep has not been set as an input, assume 0
if (nargin<7)
   pstep = 0;
end


% Generate a mesh
vec = 1:npix; [x1array,x2array] = meshgrid(vec,vec);


% Turn into columns
x = [x1array(:) x2array(:)];


% Assign number of data points
[ndata,t] = size(x);


% Get parameters in our standard form
a1 = a(1); a2 = a(2); a3 = a(3); a4 = a(4); a5 = a(5);


% Simulate the Gaussian profile
y = (a1/(2*pi*a2^2))*exp( -( (x(:,1) - a3).^2  + (x(:,2) -
a4).^2)/(2*a2^2)) + a5 + noisesd*randn(ndata,1);


% Use the same noise standard deviation for all points
sig = noisesd*ones(ndata,1);


% Fit to the simulated stellar profile by calling on
% the lmnlsqfit.m function
[a,covmtx,minchisq] = lmnlsqfit(x, y, sig, aguess, ause,
endcond,pstep);


% Assign the a2 value
```

```
a2 = a(2);
```

D.6   The `lmnlsqfit` MATLAB Function

The MATLAB function `lmnlsqfit` fits to a non-linear function using the LM method. In doing so it calls on the mrqmin function (see section D.7) which performs a single iteration. `lmnlsqfit` repeats each iteration while the fractional change in χ^2 is positive OR the fractional change in χ^2 is negative AND its absolute change is larger than the final resolution required.

```
% Function:     lmnlsqfit.m
% Purpose:      To fit to a non-linear function using the
%               LM technique.
% Syntax:
% [a,covmtx,minchisq] = lmnlsqfit(x,y,sig,aguess,ause,endcond,pstep)
% Input:        x = matrix of independent variables
%               (column per variable)
%               y = values of function corresponding to x
%               sig = Standard deviation of noise
%               at each point x
%               aguess = vector of initially guessed parameters
%               ause = vector defining the number of parameters
%               to fit for (e.g. for a 3 parameter
%               fitting ause=[1 1 0 0 1])
%               endcond = condition at which to stop the iterations
%               (i.e. when the fractional change in chi-squared
%               is less than the end condition value set,
%               Press(1992) recommends endcond=0.001)
%               pstep = if set to 1 program will step through
%               each iteration.
% Output:       a = vector of fitted parameters
%               covmtx = covariance matrix
```

```
%                minchisq = minimum chi-squared value


function [a,covmtx,minchisq] =
lmnlsqfit(x,y,sig,aguess,ause,endcond,pstep)



% define global variables. Also used in mrqmin.m and mrqcof.m


% Current Hessian martix
global alpha;


% Current values of -.5 del(chisq)/del(a(k)).
% (See Press(1992) p682)
global betaa;


% Current covariance matrix (inverse of hessian matrix)
global covm;


% Current factor to scale next step in parameters
% (See Press(1992) p683-4)
global alambda;



% Call mrqmin with alambda < 0 to initialize
alambda = -1; [newa,chisq] = mrqmin(x,y,sig,aguess,ause);


if (pstep==1)
   fprintf('ChiSq %10.4f  Lambda %10.4f  Parms ',chisq,alambda);
   fprintf('%10.4f  ',newa); fprintf('\n');
end


oldchisq = chisq; fractdcs = 0;
```

```matlab
% Repeat each iteration while the fractional change in
% chi-squared is positive OR the fractional change in
% chi-squared is negative AND its absolute change is
% larger that the final resolution required
while((fractdcs>=0)|((fractdcs<0)&(fractdcs<(-endcond))))
   [newa,chisq] = mrqmin(x,y,sig,newa,ause);
   if (pstep==1)
     fprintf('ChiSq %10.4f  Lambda %10.4f  Parms ',chisq,alambda);
     fprintf('%10.4f  ',newa); fprintf('\n');
   end
   fractdcs = (chisq-oldchisq)/oldchisq;
   oldchisq = chisq;
end


% Call on the mrqmin function for one last time to calculate
% the covariance matrix
alambda = 0; mrqmin(x,y,sig,newa,ause);
fprintf('Parms '); fprintf('%10.4f  ',newa); fprintf('\n');


% Calculate the correlation matrix
sde = sqrt(diag(covm)); mfit = length(find(ause==1)); cor =
zeros(mfit,mfit); for i = 1:mfit
  for j = 1:mfit
     cor(i,j) = covm(i,j)/(sde(i)*sde(j));
  end
end


fprintf('StdErrors  ');
fprintf('%10.3f   ',sde); fprintf('\n');
fprintf('Max corr = %5.2f percent. ChiSq = %10.2f\n',
max(max(abs(cor-eye(mfit))))*100, chisq);


% Return results
```

```
a = newa; covmtx = covm; minchisq = chisq; cor;
```

D.7   The `mrqmin` MATLAB Function

The MATLAB function `mrqmin` performs the local linearisation. `mrqmin` is a MATLAB
implementation of the C code provided by Press & Vetterling (1992) for a single iteration.

```
% Function:     mrqmin.m

% Purpose:      To perform local linearisation.

%               A Matlab implementation of the

%               mrqmin function (Press(1992) p685)

% Syntax:       [newa,newchisq] = mrqmin(x,y,sig,a,ia)

% Input:        x = Columns of independent variables

%               (i.e. a row represents a point)

%               y   = Column of data at the above points

%               sig = Column of noise standard deviations

%               at each point

%               a   = starting parameters for an iteration

%               ia  = to select which parameters to fit

%               (e.g. [1 1 0 0 1] fits for 1st,

%               2nd and 5th parameters)

% Output:       newa = matrix of calculated a parameters

%               newchisq = calculated chi-squared value


function [newa,newchisq] = mrqmin(x,y,sig,a,ia)



Step = sqrt(100);


% Following are equivalent to static through the iterations

global alpha;

global betaa;
```

```
global covm;

global alambda;

persistent chisq;

persistent mfit;

persistent ma;

persistent sel;


% Only completed first time it is called with alambda set to <0

if (alambda<0)

   % Supplied as a parameter in C version

   ma       = length(a);

   betaa    = zeros(1,ma);

   da       = zeros(1,ma);

   % Find how many parameters to fit for

   mfit     = length(find(ia==1));

   % Indices of fitted parameters in vector a

   sel      = find(ia==1);

   alambda  = .001;

   [alpha,betaa,chisq] = mrqcof(x,y,sig,a,ia);

end




% Alter linearized fitting matrix, by augmenting diagonal elements

augalpha = alpha + alambda*diag(diag(alpha));


% Solve for da in augalpha*da=betaa

% (see Press & Vetterling (1992) P682 Equation 15.5.9)

da = augalpha\betaa;


% Generate covariance matrix

covm  = inv(augalpha);


% Indicates all operations have been finished
```

```
if (alambda==0)
    return;
end


% Generate new vector of a parameters
atry  = a; atry(sel) = atry(sel)' + da;


% Call on mrqcof to calculate the Hessian Matrix(alpha) and
% Beta vector (see Press(1992) P682 Equation 15.5.8)
[newalpha,newbetaa,newchisq] = mrqcof(x,y,sig,atry,ia);


% If solution has improved accept the solution
if (newchisq<chisq)
    % Reduce alambda so as to take larger steps
    % (see Press(1992) P682 Equation 15.5.12)
    alambda = alambda/Step;
    % Save new alpha a;
    alpha = newalph
    % Save new beta
    betaa = newbetaa;
    % Save new a
    newa  = atry;
    % Save new chisq
    chisq = newchisq;
% Else if solution has not improved...
else
    % Increase alambda so as to take smaller steps
    alambda    = Step * alambda;
    % Return old chi-squared
    newchisq   = chisq;
    % Return old  vector a
    newa       = a;
end
```

D.8   The **mrqcof** MATLAB Function

The MATLAB function mrqcof is called by mrqmin for the calculation of the Hessian Matrix. mrqcof is also a MATLAB implementation of the C code provided by Press & Vetterling (1992).

```
% Function:     mrqcof.m
% Purpose:      To calculate the Hessian Matrix and Beta vector.
%               A Matlab implementation of the mrqcof function
%               (Press & Vetterling (1992) p687)
% Syntax:       [malpha, mbeta, mchisq] = mrqcof(x,y,sig,a,ia)
% Input:        x = Columns of independent variables
%               (i.e. a row represents a point)
%               y  = Column of data at the above points
%               sig = Column of noise standard deviations
%               at each point
%               a  = starting parameters for an iteration
%               ia  = to select which parameters to fit
%               (e.g. [1 1 0 0 1] fits for 1st, 2nd and
%               5th parameters)
% Output:       malpha = vector of calculated alpha values
%               mbeta = vector of calculated beta values
%               mchisq = claculated chi-squared value


function [malpha, mbeta, mchisq] = mrqcof(x,y,sig,a,ia)



ma      = length(a); dyda    = zeros(1,ma);
% Find how many parameters to fit for
mfit    = length(find(ia==1)); malpha  = zeros(mfit,mfit); mbeta
= zeros(mfit,1);
% Number of data points
[ndata,nx] = size(x); mchisq = 0;
```

```
for i=1:ndata
   % Calculate the Gaussian function and its
   % derivatives with respect to
   % the parameters
   [ymod,dyda] = afitfunc(x(i,:),a);
   sig2i       = sig(i)^(-2);
   dy          = y(i) - ymod;
   j = 0;
   for l=1:ma
      if (ia(l)==1)
         wt = dyda(l)*sig2i;
         j = j + 1; k = 0;
         for m = 1:l
            if (ia(m)==1)
               k = k + 1;
               % Calculate the Hessian Matrix
               % (see Press(1992) P682 Equation 15.5.8)
               malpha(j,k) = malpha(j,k) + wt*dyda(m);
            end
         end
         % Calculate the beta vector
         % (see Press(1992) P682 Equation 15.5.8)
         mbeta(j) = mbeta(j) + dy*wt;
      end
   end
   % Calculate chi-squared values
   mchisq = mchisq + dy*dy*sig2i;
end
% Fill in symmetric side of alpha
for j=2:mfit
   for k=1:(j-1)
      malpha(k,j) = malpha (j,k);
```

```
    end

end
```

D.9   The `afitfunc` MATLAB Function

The MATLAB function `afitfunc` is called by `mrqcof` which for input values of $\vec{x}$ and $\vec{a}$ calculates the vector of derivatives, $dydx$, (given by Equations 5.17 through to 5.21) and the model Gaussian function, `ymod`=$y(x_i; \vec{a})$ (given by Equation 5.15).

```
% Function:      afitfunc.m

% Purpose:       To generate the model Gaussian function

%                and the vector of derivatives

% Syntax:        [ymod,dyda] = afitfunc(x,a)

% Input:         a = vector of starting parameters

%                x = a single data point

% Output:        ymod = model Gaussian function

%                dyda = vector of derivatives


function    [ymod,dyda] = afitfunc(x,a)



x1  = x(1); x2 = x(2); a1  = a(1); a2 = a(2); a3 = a(3); a4 =
a(4); a5 = a(5);


% Calculate the model Gaussian function
t1  = 1/(2*pi*a2^2);


t2  = a1*t1;


dx1 = x1-a3;


dx12 = dx1^2;
```

```
dx2=x2-a4;


dx22 = dx2^2;


xs2 = dx12 + dx22;


e = exp(-xs2/(2*a2^2));


ymod = t2*e;


%Calculate the vector of derivatives
dyda = 0*a;


dyda(1) = ymod/a1;


dyda(2) = ymod*( -2/a2 + xs2/a2^3);


dyda(3) = ymod*dx1/a2^2;


dyda(4) = ymod*dx2/a2^2;


dyda(5) = 1;


ymod = ymod + a5;
```

Appendix E

Tables of Error Estimations

E.1   Introduction

The following tables contain error estimation results for fitting with both five parameters and three parameters (see Chapter 5). These results are part of a much larger study which have successfully identified how the SE of the seeing depends on the signal to noise ratio, size of the fitting window and resolution. In order, the column headings for these tables are as follows:

- a_1 is the signal count - total counts if all light from a star was collected by one pixel (i.e. area under the Gaussian curve);

- a_2 is the standard deviation of the gaussian profile;

- a_5 is the CCD pedestal voltage;

- `pixfact` is the number of standard deviations across the fitting window;

- `npix` is the size of the fitting window in pixels;

- SE(a_1) is the standard error in parameter a_1;

- SE(a_2) is the standard error in parameter a_2;

- SE(a_3) is the standard error in parameter a_3;

- SE(a_4) is the standard error in parameter a_4;

- SE(a_5) is the standard error in parameter a_5;

- Max Corr is the maximum correlation between the fitted parameters (Equation 5.13);

- S/N is the signal to noise ratio (equal to $\frac{a_1}{2\pi a_2^2}$ for $\sigma_{noise} = 1$);

- Cond is the condition number (see 5.4.1).

E.2   Results

a_1	a_2	a_5	pixfact	npix	SE(a_1)	SE(a_2)	SE(a_3)	SE(a_4)	SE(a_5)	Max Corr(%)	S/N	Cond
10	5	10	0.2	3	18.3	4.7	4.7×10^6	4.7×10^6	0.11	8.48	0.064	1.92×10^{15}
10^2	5	10	0.2	3	18.3	4.7×10^{-1}	4.7×10^5	4.7×10^5	0.11	8.48	0.64	1.92×10^{13}
10^3	5	10	0.2	3	18.3	$\mathbf{4.7 \times 10^{-2}}$	4.7×10^4	4.7×10^4	0.11	8.48	**6.4**	1.12×10^{12}
10^4	5	10	0.2	3	18.3	4.7×10^{-3}	4.7×10^3	4.7×10^3	0.11	8.48	64	1.12×10^{12}
10^5	5	10	0.2	3	18.3	4.7×10^{-4}	4.7×10^2	4.7×10^2	0.11	8.48	640	1.12×10^{12}
10	5	10	0.5	5	6.8	2	1.85×10^6	1.85×10^6	0.04	3.65	0.064	2.2×10^{15}
10^2	5	10	0.5	5	6.8	2×10^{-1}	1.85×10^5	1.85×10^5	0.04	3.65	0.64	2.2×10^{13}
10^3	5	10	0.5	5	6.8	$\mathbf{2 \times 10^{-2}}$	1.85×10^4	1.85×10^4	0.04	3.65	**6.4**	1.0×10^{12}
10^5	5	10	0.5	5	6.8	2×10^{-4}	1.85×10^2	1.85×10^2	0.04	3.65	640	1.0×10^{12}
10	5	10	1.0	7	3.8	1.1	1.1×10^6	1.1×10^6	0.02	2.00	0.064	3.0×10^{15}
10^2	5	10	1.0	7	3.8	1.1×10^{-1}	1.1×10^5	1.1×10^5	0.02	2.00	0.64	3.0×10^{13}
10^3	5	10	1.0	7	3.8	$\mathbf{1.1 \times 10^{-2}}$	1.1×10^4	1.1×10^4	0.02	2.00	**6.4**	1.0×10^{12}
10^5	5	10	1.0	7	3.8	1.1×10^{-4}	1.1×10^2	1.1×10^2	0.02	2.00	640	1.0×10^{12}
10	5	10	1.5	9	2.5	8.2×10^{-1}	8.2×10^5	8.2×10^5	0.01	1.3	0.064	4.5×10^{15}
10^2	5	10	1.5	9	2.5	8.2×10^{-2}	8.2×10^4	8.2×10^4	0.01	1.3	0.64	4.5×10^{13}
10^3	5	10	1.5	9	2.5	$\mathbf{8.2 \times 10^{-3}}$	8.2×10^3	8.2×10^3	0.01	1.3	**6.4**	1.0×10^{12}
10^5	5	10	1.5	9	2.5	8.2×10^{-5}	8.2×10^1	8.2×10^1	0.01	1.3	640	1.0×10^{12}

Table E.1: Error Estimation Using 5 Parameters. For each window size (npix) in the set 3, 5, 7 and 9 pixels wide, the amplitude (a_1) is increased in multiples of 10 within the range of 10 to 10^5, and the standard error of a_2 (SE(a_2)) is displayed. The process is then repeated for Gaussian profiles with standard deviations decrementing from 5 pixels to 1 pixel.

a_1	a_2	a_5	pixfact	npix	SE(a_1)	SE(a_2)	SE(a_3)	SE(a_4)	SE(a_5)	Max Corr(%)	S/N	Cond
10	3	10	0.5	3	6.9	1.1	6.7×10^5	6.7×10^5	0.11	8.75	0.18	3.9×10^{13}
10^2	3	10	0.5	3	6.9	1.1×10^{-1}	6.7×10^4	6.7×10^4	0.11	8.75	1.8	4.4×10^{11}
10^3	3	10	0.5	3	6.9	1.1×10^{-2}	6.7×10^3	6.7×10^3	0.11	8.75	18	4.0×10^{11}
10^5	3	10	0.5	3	6.9	1.1×10^{-4}	6.7×10^1	6.7×10^1	0.11	8.75	1800	4.0×10^{11}
10	3	10	1.0	5	2.8	5.3×10^{-1}	3.2×10^5	3.2×10^5	0.04	3.88	0.18	6.5×10^{13}
10^2	3	10	1.0	5	2.8	5.3×10^{-2}	3.2×10^4	3.2×10^4	0.04	3.88	1.8	6.5×10^{11}
10^3	3	10	1.0	5	2.8	5.3×10^{-3}	3.2×10^3	3.2×10^3	0.04	3.88	18	3.7×10^{11}
10^5	3	10	1.0	5	2.8	5.3×10^{-5}	3.2×10^1	3.2×10^1	0.04	3.88	1800	3.7×10^{11}
10	3	10	1.5	7	1.74	4×10^{-1}	2.5×10^5	2.5×10^5	0.02	2.35	0.18	1.5×10^{14}
10^2	3	10	1.5	7	1.74	4×10^{-2}	2.5×10^4	2.5×10^4	0.02	2.35	1.8	1.5×10^{12}
10^3	3	10	1.5	7	1.74	4×10^{-3}	2.5×10^3	2.5×10^3	0.02	2.35	18	3.6×10^{11}
10^5	3	10	1.5	7	1.74	4×10^{-5}	2.5×10^1	2.5×10^1	0.02	2.35	1800	3.6×10^{11}
10	3	10	2.5	9	1.33	4.4×10^{-1}	2.7×10^5	2.7×10^5	0.012	1.91	0.18	4.6×10^{14}
10^2	3	10	2.5	9	1.33	4.4×10^{-2}	2.7×10^4	2.7×10^4	0.012	1.91	1.8	4.6×10^{12}
10^3	3	10	2.5	9	1.33	4.4×10^{-3}	2.7×10^3	2.7×10^3	0.012	1.91	18	3.6×10^{11}
10^5	3	10	2.5	9	1.33	4.4×10^{-5}	2.7×10^1	2.7×10^1	0.012	1.91	1800	3.6×10^{11}
10	1.6	10	1.0	3	2.34	2.5×10^{-1}	7.85×10^4	7.85×10^4	0.11	10	0.62	5.22×10^{11}

Table E.2: Error Estimation Using 5 Parameters Continued.

a_1	a_2	a_5	pixfact	npix	SE(a_1)	SE(a_2)	SE(a_3)	SE(a_4)	SE(a_5)	Max Corr(%)	S/N	Cond
10^3	1.6	10	1.0	3	2.34	2.5×10^{-3}	7.85×10^2	7.85×10^2	0.11	10	62	1.09×10^{11}
10^5	1.6	10	1.0	3	2.34	2.5×10^{-5}	7.85	7.85	0.11	10	6200	1.09×10^{11}
10	1.6	10	2.0	5	1.27	2.4×10^{-1}	7.78×10^4	7.78×10^4	0.04	6.5	0.62	3.80×10^{12}
10^3	1.6	10	2.0	5	1.27	2.4×10^{-3}	7.78×10^2	7.78×10^2	0.04	6.5	62	1.03×10^{11}
10^5	1.6	10	2.0	5	1.27	2.4×10^{-5}	7.78	7.78	0.04	6.5	6200	1.03×10^{11}
10	1.6	10	3.0	7	1.06	5.4×10^{-1}	1.7×10^5	1.7×10^5	0.02	11	0.62	7×10^{13}
10^3	1.6	10	3.0	7	1.06	5.4×10^{-3}	1.7×10^3	1.7×10^3	0.02	11	62	1.0×10^{11}
10^5	1.6	10	3.0	7	1.06	5.4×10^{-5}	1.7×10^1	1.7×10^1	0.02	11	6200	1.0×10^{11}
10	1.6	10	5.0	9	1.1	2.22	6.5×10^5	6.5×10^5	0.01	40	0.62	2.8×10^{15}
10^3	1.6	10	5.0	9	1.1	2.22×10^{-2}	6.5×10^3	6.5×10^3	0.01	40	62	2.8×10^{15}
10^5	1.6	10	5.0	9	1.1	2.22×10^{-4}	6.5×10^1	6.5×10^1	0.01	40	6200	1.0×10^{11}
10	**1.0**	**10**	**2.0**	**3**	**1.3**	$\mathbf{1.5 \times 10^{-1}}$	$\mathbf{2.9 \times 10^4}$	$\mathbf{2.9 \times 10^4}$	**0.11**	**16**	**1.6**	$\mathbf{6.8 \times 10^{10}}$
10^3	1.0	10	2.0	3	1.3	1.5×10^{-3}	2.9×10^2	2.9×10^2	0.11	16	160	4.1×10^{10}
10^5	1.0	10	2.0	3	1.3	1.5×10^{-5}	2.9	2.9	0.11	16	1600	4.1×10^{10}
10	1.0	10	4.0	5	1.2	8.1×10^{-1}	1.3×10^5	1.3×10^5	0.04	55	1.6	1.1×10^{13}
10^3	1.0	10	4.0	5	1.2	8.1×10^{-3}	1.3×10^3	1.3×10^3	0.04	55	160	4×10^{10}
10	1.0	10	5.0	7	1.0	0	1.7×10^6	1.7×10^6	0.02	96	1.6	1.5×10^{16}

Table E.3: Error Estimation Using 5 Parameters Continued.

a_1	a_2	a_5	pixfact	npix	SE(a_1)	SE(a_2)	SE(a_5)	Max Corr(%)	S/N	Cond
5	0.8	10	3.0	3	1.16	3.7×10^{-1}	0.11	31	**1.25**	1.1×10^2
10	0.8	10	3.0	3	1.16	1.8×10^{-1}	0.11	31	**2.50**	1.1×10^2
50	0.8	10	3.0	3	1.16	3.7×10^{-2}	0.11	31	**12.5**	1.1×10^3
10^2	0.8	10	3.0	3	1.16	1.8×10^{-2}	0.11	31	**25.0**	4.5×10^3
500	0.8	10	3.0	3	1.16	3.7×10^{-3}	0.11	31	**125**	1.1×10^5
10^3	0.8	10	3.0	3	1.16	1.8×10^{-3}	0.11	31	**250**	4.5×10^5
5	5	10	2.0	11	1.88	**1.43**	8.3×10^{-3}	0.93	**0.032**	5.2×10^4
10	5	10	2.0	11	1.88	$\mathbf{7.13 \times 10^{-1}}$	8.3×10^{-3}	0.93	**0.064**	5.2×10^4
50	5	10	2.0	11	1.88	$\mathbf{1.43 \times 10^{-1}}$	8.3×10^{-3}	0.93	**0.32**	5.2×10^4
10^2	5	10	2.0	11	1.88	$\mathbf{7.13 \times 10^{-2}}$	8.3×10^{-3}	0.93	**0.64**	5.2×10^4
500	5	10	2.0	11	1.88	$\mathbf{1.43 \times 10^{-2}}$	8.3×10^{-3}	0.93	**3.2**	5.2×10^4
10^3	5	10	2.0	11	1.88	$\mathbf{7.13 \times 10^{-3}}$	8.3×10^{-3}	0.93	**6.4**	7.0×10^4

Table E.4: Demonstrating the dependence of SE of fitting parameters on S/N. For a fixed window size (npix) , the amplitude (a_1) is increased in multiples of 2 and 5 consecutively within the range of 5 to 10^3, and the standard error of a_2 (SE(a_2)) is displayed.

a_1	a_2	a_5	pixfact	npix	SE(a_1)	SE(a_2)	SE(a_5)	Max Corr(%)	S/N	Cond
10^2	2	10	1.0	**3**	3.33	$\mathbf{3.96 \times 10^{-2}}$	1.12×10^{-1}	10.2	4	7.24×10^3
10^2	2	10	2.0	**5**	1.59	$\mathbf{2.72 \times 10^{-2}}$	4.00×10^{-2}	4.73	4	3.43×10^3
10^2	2	10	3.0	**7**	1.18	$\mathbf{3.60 \times 10^{-2}}$	2.04×10^{-2}	4.41	4	3.32×10^3
10^2	2	10	4.0	**9**	1.05	$\mathbf{7.35 \times 10^{-2}}$	1.24×10^{-2}	7.71	4	7.25×10^3
10^2	2	10	5.0	**11**	1.04	$\mathbf{2.16 \times 10^{-1}}$	8.27×10^{-3}	21.3	4	1.57×10^4
500	4	10	0.5	**3**	1.18	$\mathbf{4.91 \times 10^{-2}}$	1.12×10^{-1}	10.0	5	5.9×10^4
500	4	10	1	**5**	4.55	$\mathbf{2.07 \times 10^{-2}}$	4.01×10^{-2}	3.90	5	4.9×10^4
500	4	10	1.5	**7**	2.61	$\mathbf{1.35 \times 10^{-2}}$	2.04×10^{-2}	2.10	5	3.74×10^4
500	4	10	2.0	**9**	1.82	$\mathbf{1.128 \times 10^{-2}}$	1.24×10^{-2}	1.41	5	2.62×10^4
500	4	10	2.5	**11**	1.45	$\mathbf{1.125 \times 10^{-2}}$	8.27×10^{-3}	1.13	5	3.06×10^4
500	4	10	3.0	**13**	1.24	$\mathbf{1.29 \times 10^{-2}}$	5.92×10^{-3}	1.08	5	4.42×10^4
500	4	10	3.5	**15**	1.13	$\mathbf{1.65 \times 10^{-2}}$	4.45×10^{-3}	1.21	5	6.49×10^4
500	4	10	4.0	**17**	1.07	$\mathbf{2.34 \times 10^{-2}}$	3.46×10^{-3}	1.59	5	9.56×10^4

Table E.5: Demonstrating the dependence of SE of fitting parameters on fitting window. For a fixed S/N, the window size (npix) is increased between 3 and 11 pixels wide and the standard error of a_2 (SE(a_2)) is displayed.

a_1	a_2	a_5	pixfact	npix	SE(a_1)	SE(a_2)	SE(a_5)	Max Corr(%)	S/N	Cond
1570	**5**	10	0.3	**3**	18.1	$\mathbf{2.97 \times 10^{-2}}$	1.12×10^{-1}	10	10	3.83×10^5
1570	**5**	10	0.5	**5**	6.81	$\mathbf{1.18 \times 10^{-2}}$	4.01×10^{-2}	3.86	10	3.37×10^5
1570	**5**	10	1.0	**7**	3.75	$\mathbf{7.02 \times 10^{-3}}$	2.04×10^{-2}	2.04	10	2.85×10^5
1570	**5**	10	1.5	**9**	2.5	$\mathbf{5.24 \times 10^{-3}}$	1.24×10^{-2}	1.29	10	2.28×10^5
1570	**5**	10	2.0	**11**	1.88	$\mathbf{4.54 \times 10^{-3}}$	8.27×10^{-3}	0.93	10	1.71×10^5
1005	**4**	10	0.5	**3**	11.8	$\mathbf{2.44 \times 10^{-2}}$	1.12×10^{-1}	10.0	10	2.38×10^5
1005	**4**	10	1.0	**5**	4.55	$\mathbf{1.03 \times 10^{-2}}$	4.01×10^{-2}	3.89	10	1.96×10^5
1005	**4**	10	1.5	**7**	2.61	$\mathbf{6.71 \times 10^{-3}}$	2.04×10^{-2}	2.10	10	1.51×10^5
1005	**4**	10	2.0	**9**	1.82	$\mathbf{5.61 \times 10^{-3}}$	1.24×10^{-2}	1.41	10	1.06×10^5
1005	**4**	10	2.5	**11**	1.45	$\mathbf{5.59 \times 10^{-3}}$	8.27×10^{-3}	1.13	10	6.67×10^4

Table E.6: Demonstrating the dependence of SE of fitting parameters on resolution. A family of curves have been generated where the S/N has been held fixed at 10 for all curves. For each curve a_2 has been held fixed, while the window size (npix) is incremented between 3 and 11 pixels wide. The standard error of a_2 (SE(a_2)) is then displayed.

a_1	a_2	a_5	pixfact	npix	SE(a_1)	SE(a_2)	SE(a_5)	Max Corr(%)	S/N	Cond
565	**3**	10	0.5	**3**	6.84	1.96×10^{-2}	1.12×10^{-1}	10.0	10	1.25×10^5
565	**3**	10	1.0	**5**	2.81	9.37×10^{-3}	4.01×10^{-2}	4.00	10	8.99×10^4
565	**3**	10	1.5	**7**	1.74	7.37×10^{-3}	2.04×10^{-2}	2.35	10	5.56×10^4
565	**3**	10	2.5	**9**	1.33	7.85×10^{-3}	1.24×10^{-2}	1.90	10	2.86×10^4
565	**3**	10	3.0	**11**	1.15	1.05×10^{-2}	8.27×10^{-3}	2.09	10	1.92×10^4
252	**2**	10	1.0	**3**	3.33	1.57×10^{-2}	1.12×10^{-1}	10.2	10	4.59×10^4
252	**2**	10	2.0	**5**	1.59	1.08×10^{-2}	4.01×10^{-2}	4.73	10	2.18×10^4
252	**2**	10	3.0	**7**	1.18	1.43×10^{-2}	2.04×10^{-2}	4.41	10	6.80×10^3
252	**2**	10	4.0	**9**	1.05	2.92×10^{-2}	1.24×10^{-2}	7.71	10	7.25×10^3
252	**2**	10	5.0	**11**	1.04	8.57×10^{-2}	8.27×10^{-3}	21.3	10	1.57×10^4
40	**0.8**	**10**	**3.0**	**3**	**1.16**	$\mathbf{4.58 \times 10^{-2}}$	$\mathbf{1.12 \times 10^{-1}}$	**31.0**	**10**	$\mathbf{7.20 \times 10^2}$

Table E.7: Demonstrating the dependence of SE of fitting parameters on resolution Continued.